Conformational Spread in the Bacterial Flagellar Switch

Richard William Branch

A thesis submitted in partial fulfillment of
the requirements for the degree of
Doctor of Philosophy at the University of Oxford

St. Cross College
University of Oxford
Trinity Term 2010

Conformational Spread in the Bacterial Flagellar Switch

Richard William Branch

St. Cross College

Thesis submitted for the degree of Doctor of Philosophy,
University of Oxford, Trinity Term 2010.

Abstract

The bacterial flagellar switch is responsible for controlling the direction of rotation of the bacterial flagellar motor during chemotaxis. The flagellar switch has a highly cooperative response, contributing to the remarkable signal amplification observed in the *Escherichia coli* chemotactic signal transduction pathway. A central goal in the study of the pathway has been to understand such sources of amplification.

Flagellar switching has classically been understood in terms of the two-state concerted model of allosteric cooperativity. In this study, switching of single motors was observed with high resolution back-focal-plane interferometry, uncovering the stochastic multi-state nature of the switch. The observations are in detailed quantitative agreement with simulations of a recent general model of allosteric cooperativity, exhibiting the novel phenomenon of conformational spread.

Publications

T. Pilizota*, M. T. Brown*, M. C. Leake, **R. W. Branch**, R. M. Berry, and J. P. Armitage. A molecular brake, not a clutch, stops the *Rhodobacter sphaeroides* flagellar motor. *Proc. Natl. Acad. Sci. U.S.A.* **106**, 11590 (2009)

Author contributions: T.P., M.T.B., R.M.B., and J.P.A. designed research; T.P. and M.T.B. performed research; M.C.L. contributed new reagents/analytic tools; T.P., M.T.B., and R.W.B. analyzed data; and T.P. and M.T.B. wrote the paper.

F. Bai*, **R. W. Branch***, D. V. Nicolau, Jr.*, T. Pilizota, B. C. Steel, P. K. Maini, R. M. Berry. Conformational Spread as a mechanism for cooperativity in the bacterial flagellar switch. *Science* **327**, 685 (2010)

Author contributions: hypothesis developed by R.W.B., F. B., R.M.B.; experiments designed by F.B., T.P., R.W.B and R.M.B.; experiments were carried out by F.B., R.W.B and T. P. in the laboratory of R.M.B.; the experimental system was designed by T.P. and R.M.B.; data analysis was done by R.W.B., F.B. and R.M.B.; preliminary simulations were carried out by D.V.N. under the instructions of P.K.M.; final simulations were carried out by B.C.S. and R.W.B.; the paper was written by R.W.B., F.B., B.C.S. and R.M.B..

* these authors contributed equally

Acknowledgements

Contents

Chapter 4   Observations

Chapter 5   Model agreement

Chapter 6   Further Work

Chapter 1

Introduction

1.1 Preamble

Reductionism is a necessary component for successful scientific enquiry, but alone is insufficient to understand the emergent properties of biological complexity. A systems approach to the subject is required, in which the multi-variate datasets of experimental investigation are integrated by sweeping quantitative models, through numerous rounds of the Scientific Method. In this way, it is hoped that insightful in silico reproductions of the system can be achieved, and possibly even that biological laws are established.

The bacterial chemotaxis network is among the most well characterised signal transduction pathways in biology. The core of the network is conserved throughout the bacterial kingdom, with the simplest and paradigmatic form found in *Escherichia coli* (*E. coli*). In this species, the structure, copy number, localisation and kinetics of almost all known participating proteins have been elucidated. Together with the superior experimental accessibility of signal output, namely flagellar rotation, the pathway has provided an ideal candidate for systems biology study. The lessons learned are expected to be of broad relevance to other biological systems.

1.2 The motility of *E. coli*

Of the various forms of locomotion observed in the bacterial kingdom, *E. coli*, the protagonist of this study, swims in fluid by rotating long helical flagellar filaments that are attached to rotary molecular motors embedded in the cell envelope (Berg and Anderson, 1973, Silversmith and Simon, 1974). The bacterium operates in an environment with a low Reynolds number ($\sim 10^{-4}$), such that viscous drag dominates inertia. Propulsion arises due to the reaction force against viscous drag over non-reciprocal cycles of rotating helical flagella, rather than the displacement of fluid as in a macroscopic propeller, resulting in cell translation (and roll) (Purcell, 1997).

There are typically half a dozen independently functioning motors distributed over the cell surface, each able to rotate clockwise (CW) and counter-clockwise (CCW). During CCW rotation (looking down the filament towards the cell body), the stable left-handed flagella form a bundle due to hydrodynamic interactions, allowing the cell to 'run' smoothly in one direction at speeds of 20-30 μm s^{-1}. During CW rotation of one or more motors, the associated flagella undergo a torsionally induced polymorphic transformation to an unstable right-handed state and leave the bundle, causing erratic 'tumbling' of the cell, and random reorientation for the subsequent run (Berg and Brown, 1972, Turner *et al.* 2000, Darnton *et al.* 2007, Kim *et al.*, 2003) (Figure 1.1). The ability of motors to switch direction of rotation is pivotal to the process of chemotaxis, the biased random walk towards high concentrations of attractant molecules and away from high concentrations of repellent molecules in the extra-cellular environment (Brown and Berg, 1974, Berg and Tedesco, 1975).
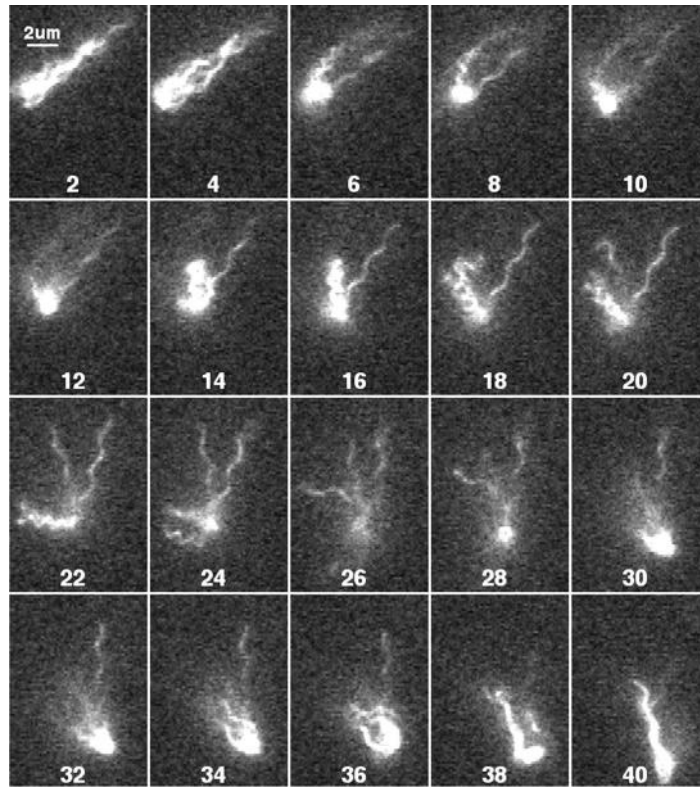
Figure 1.1. A swimming *E. coli* bacterial cell, where the body and filaments have been labelled with Alexa Fluor 532 and illuminated by a strobed argon-ion laser (image from Turner *et al.*, 2000). Frame rate is 60 Hz and every other frame is shown. All but one of the filaments undergo a polymorphic transformation, disrupting the bundle and redirecting the cell.

Being too small in size to sense gradients directly, the cell measures spatial gradients by temporal sampling as it swims. In baseline swimming behaviour, cells run for ~ 1 s and tumble for ~ 1/10 s. By modulating the frequency of switching between CW and CCW rotation, the cell can perform a biased random walk to preferable areas. When the cell moves up a spatial gradient of attractant or down a spatial gradient of repellent, runs are extended, up to ~ 10 s. Runs do not exceed the 1-10 s range due to physical considerations (Berg and Purcell, 1977). Below 1 s, the cell does not travel far enough to outrun diffusion and make a fresh estimate of stimuli concentration. Meanwhile, running for longer than 10 s is futile since the cell drifts off course by more than 90° due to Brownian motion. The motors receive instructions to modulate the frequency of switching via an intracellular signal transduction pathway, which is reviewed in the next section.

1.3 The chemosensory pathway of *E. coli*

1.3.1 Molecular details

Many signal transduction pathways in prokaryotes utilise two-component histidine-aspartate phosphorelay (HAP) systems, in which a histidine protein kinase with a fused sensory domain catalyses the transfer of phosphoryl groups from adenosine-tri-phosphate (ATP) to one of its own histidine residues. The group is then transferred to an aspartate residue on a response regulator that proceeds to regulate the pathway output. The chemosensory pathway of *E. coli* represents a variation on this theme and has been thoroughly characterised. For reviews see Bren and Eisenbach, 2000, Bourret and Stock,

2002, Wadhams and Armitage, 2004, Sourjik, 2004, Parkinson *et al.*, 2005, Baker *et al.*, 2006ab.

The system is depicted in Figure 1.2. Dedicated transmembrane receptor proteins are responsible for detecting attractant and repellent stimuli. Different receptor species are capable of binding aspartate and maltose (Tar receptor), serine (Tsr receptor), dipeptides (Tap receptor), or ribose and galactose (Trg). A fifth type of receptor (Aer) detects redox potential for mediating aerotaxis responses. Tar and Tsr are the major receptors, comprising ~7500 molecules per cell, while the minor receptors number a few hundred copies. The histidine protein kinase CheA associates with receptors via the coupling protein CheW to form sensory complexes. Signalling proceeds through conformational changes induced in receptors as a result of changes in occupancy, which are propagated to CheA. Sensory complex response occurs over the timescale of milliseconds.

Autophosphorylation activity of CheA is enhanced by increases in repellents or decreases in attractants. The phosphoryl group is transferred to the response regulator CheY protein on the timescale of tenths of seconds. CheY-P is released and diffuses to motors on the timescale of microseconds, where binding to the motor increases the probability of CW rotation. CheA autophosphorylation is inhibited by increases in attractants or decreases in repellents, leading to a decrease in CheY-P concentration and increased probability of CCW rotation.

Three other proteins complete the pathway. The phosphatase CheZ, localised to the sensory complex, provides signal termination and a steady-state level of CheY-P during adapted conditions by decreasing CheY-P half life from ~ 20s to ~ 200ms. Adaptation to
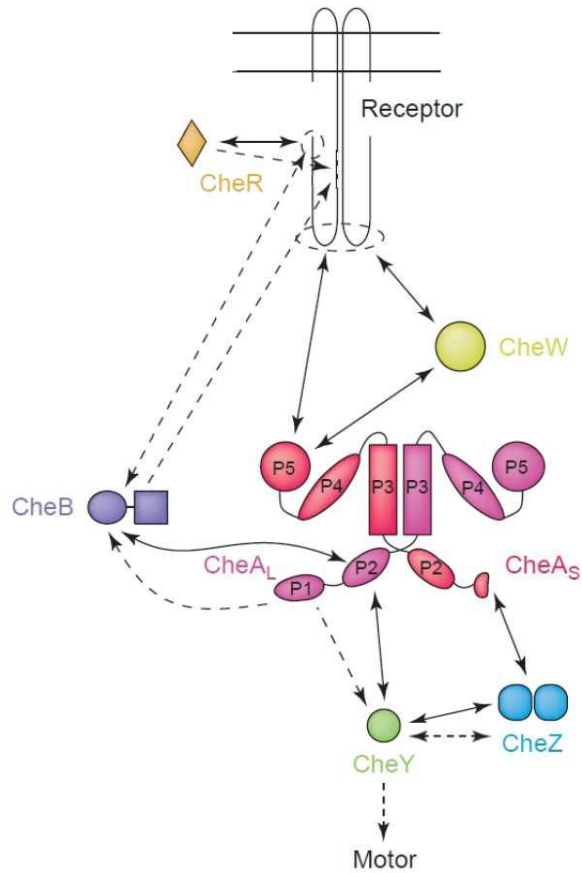
Figure 1.2. The *E. coli* chemosensory pathway. Diagram modified from Sourjik, 2004. Solid arrows identify localisation, dashed arrows identify interactions. Receptors form homodimers. The periplasmic sensory domain of receptor monomers consist of an up-down-up-down four helix bundle, connected via a hydrophobic membrane spanning helix to a long hairpin-like anti-parallel coiled coil extending into the cytoplasm. A highly conserved signalling domain at the cytoplasmic tip binds CheW and CheA. CheA has five domains: a phosphorylation domain (P1); a binding domain (P2); a dimerisation domain (P3); a catalytic domain (P4) and a regulatory domain for coupling CheA to CheW (P5). CheA is expressed in two forms: full-length CheA$_L$ and short-length CheA$_S$, which lacks a phosphorylation site and binds CheZ. CheY and CheB bind competitively to P2 and are phosphorylated by the P1 domain of CheA$_L$. CheR and CheB bind in competition to an NWETF pentapeptide sequence at the C-terminus of the major receptors (Tar and Tsr) for receptor modification (this sequence is absent in minor receptors, which are modified by CheR/CheB docked to nearby major receptors).

attractant stimuli is mediated by the constitutively active methyltransferase CheR, which adds methyl groups to receptors from a cytoplasmic pool of S-adenosyl methionine, to increase CheA activity. Adaptation to repellent stimuli is mediated by the methylesterase CheB, a second response regulator that is phosphorylated by CheA, before proceeding to demethylate or deamidate receptors. Phosphotransfer to CheY is faster than to CheB, ensuring a response is generated before adaptation occurs. Negative feedback in both adaptation scenarios is provided by CheB. Adaptation occurs on the timescale of seconds under physiological conditions and resets signalling to the baseline level.

1.3.2 Amplification

The remarkable signal processing abilities of the *E. coli* chemosensory pathway have been the subject of interest for several decades. Early investigation explored the rotational response of a tethered cell (attached by a single antibody-treated filament to a microscope coverslip) following exposure to small steps in aspartate concentration delivered iontophoretically (Segall *et al.*, 1986). According to estimates of receptor number and aspartate dissociation constant, steps leading to a change in the aspartate receptor occupancy of just 0.2 % (~ 20 out of the ~ 10000 receptors) resulted in a 23 % change in CW bias (the probability of CW rotation). The amplification of the pathway, defined as the fractional change in CW bias divided by the fractional change in receptor occupancy, therefore stands at a factor of ~ 100. Coupling to the adaptation system allows widely variable sensitivity (defined as the inverse of the concentration resulting in a half maximal response) and prevents signal saturation at higher stimuli concentrations (Koshland *et al.*, 1982). The cell has the resulting ability to maintain the amplification

response over ambient concentrations spanning five orders of magnitude from 10 nM aspartate (Bray, 2002).

The higher order organisation of the receptors is critical for this response. The revelation that sensory complexes assemble into tight clusters (Maddock and Shapiro, 1993, Sourjik and Berg, 2000) rather than being scattered independently around the cell surface indicated a possible source of interaction responsible for amplification (Bray *et al.*, 1998). Indeed, clustering has since been observed in all other examined bacteria and archea (Gestwicki *et al.*, 2000) suggesting a universal mechanism for signal processing. The basic receptor units of the cluster in *E. coli* are thought to be homo- and hetero-trimers of homo-dimers (Kim *et al.*, 1999, Ames *et al.*, 2002, Studdert and Parkinson, 2004). Various stochiometries for CheW and CheA relative to the trimers have been proposed (Li and Hazelbauer, 2004, Ames and Parkinson, 1994, Ames *et al.*, 2002), but all arrangements suggest that several receptors have collaborative control over only a few CheA dimers. This also provides a means of signal integration and an explanation for how the minor receptors are able to generate a response equal to the major receptors (Sourjik and Berg, 2004).

Confirmation of the contribution of clusters to pathway amplification was provided by an in vivo fluorescence study, where CheA activity was inferred from the steady-state concentration of the CheZ-CheY-P complex, measured using Forster-resonance-energy-transfer (FRET) between the fluorescently labelled CheZ and CheY proteins (Sourjik and Berg, 2002a). A 1 % change in receptor occupancy resulted in a 35 % inhibition of CheA activity. Interactions between receptors have since been elucidated (Li and Weis, 2000, Bornhorst and Falke, 2000, Gestwicki and Kiessling, 2002); a notable study using the

above approach demonstrated that heterogeneous receptor populations operate with reduced amplification relative to homogenous populations, indicating functional interactions between receptors (Sourjik and Berg, 2004). Modelling of the response as a function of receptor species homogeneity (Sourjik and Berg, 2004, Endres *et al.*, 2008) suggests that receptor trimers form teams of ~ 10 units. Domain swapping has been proposed as a mechanism of interaction, in which the second coiled coil after the hairpin in one receptor partners with the first coiled coil in a neighbouring receptor (Wolanin and Stock, 2004). Receptor interaction mediated via the CheA-CheW complex has also been considered (Shimizu *et al.*, 2000).

Beyond the clusters, there does not appear to be any amplification in the cytoplasm; a linear relationship exists between CheA activity and CheY-P concentration, and CheZ deletion mutants retain amplification ability (Kim *et al.*, 2001, Sourjik and Berg, 2002ab). The second and final amplification step occurs at the motor. Early tethered cell studies relying on population averaging revealed a weak sigmoidal dependence of CW bias on expressed CheY-P concentration (Scharf *et al.*, 1998a, Alon *et al.*, 1998). A later study demonstrating the importance of single cell measurements corrected this finding. The concentration of fluorescently labelled CheY-P was variably expressed and monitored in a single immobilised cell, while motor rotational bias was assessed by video darkfield microscopy of a latex bead attached to a rotating flagellum (Cluzel *et al.*, 2000). A steep sigmoidal relationship was observed between CheY-P concentration and motor bias: for very small changes in CheY-P concentration about the operational value (~ 3 μM), very large changes in motor bias are observed, leading to a maximum of 4-fold

amplification in the signal. When combined with the receptor amplification, this motor response explains the overall ~ 100 fold amplification in the pathway.

In terms of understanding the cell's signal processing abilities, attention has focused mainly on the receptor-end of the pathway, the chief source of amplification, and adaptation, in chemotactic response. This study concerns the end-point amplification mechanism. In the following sections, we review our experimental subject, the bacterial flagellar motor and flagellar switch.

1.4 The bacterial flagellar motor of *E. coli*

1.4.1 Structure and function

Flagellar rotation is due to the bacterial flagellar motor, which is capable of driving filaments at rotation rates, or 'speeds', of order 100 Hz in *E. coli* (the record is held by the *Vibrio* species, clocked at 1700 Hz). At 11 MDa, comprising ~ 13 different protein components and a further ~ 25 for expression and assembly, the motor is one of the largest and most complicated assemblies in the bacterial cell (Berg, 2002). As with the chemosensory pathway, *E. coli* provides the most well studied example, along with *Salmonella enterica* Sv *typhimurium* (*S. typhimurium*) and *Thermotoga maritima* (*T. maritima*).

Electron microscopy reconstructions have provided a general picture of the flagellar motor (Figure 1.3). Like macroscopic rotary motors, the motor consists of a rotor and stator. The rotor comprises four rings and a rod (DePamphilis and Adler, 1971). The MS (Membrane, Supermembranous) ring is constructed first, of ~ 26 FliF protein subunits
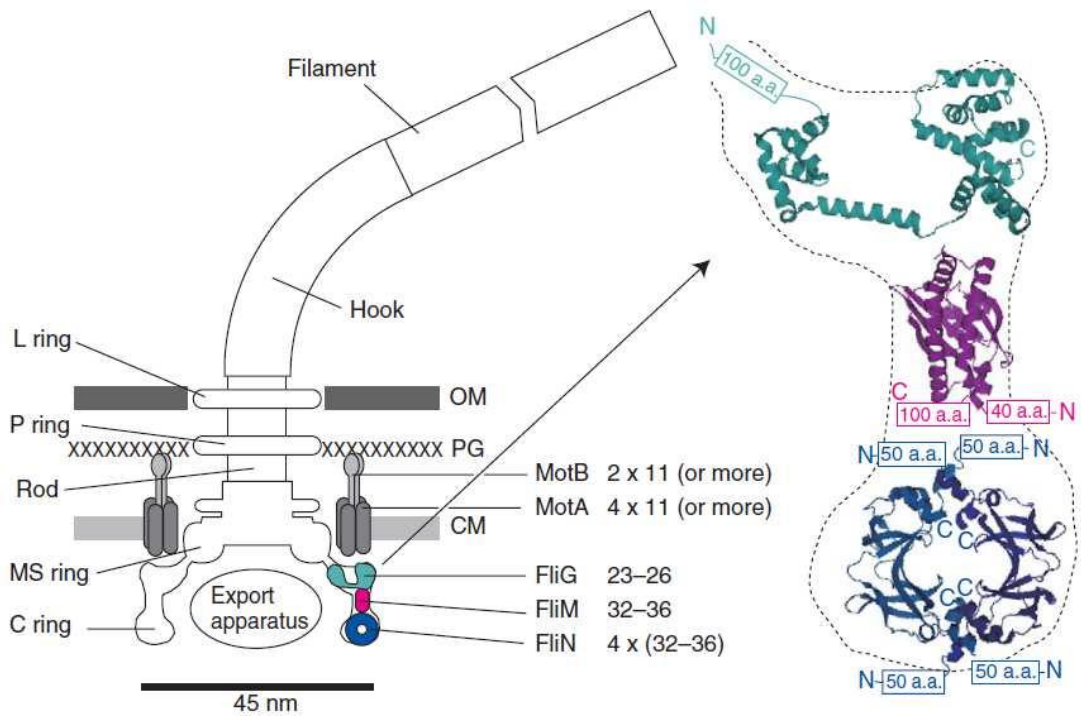
Figure 1.3. Schematic of the bacterial flagellar motor (from Sowa and Berry, 2008). The motor consists of a rotor comprising a rod and four rings, and a stator comprising $MotA_2MotB_4$ units. The assembly spans the outer membrane (OM), peptidoglycan wall (PG) and cytoplasmic membrane (CM). Rotation is coupled to the flagellar filament via the hook, a universal joint. Right: detail of the proposed location and orientation of C-ring proteins consistent with the model of Brown *et al.*, 2007. X-ray crystal structures of the truncated proteins are shown docked into rotor structure. N- and C- termini and missing amino acids are indicated.

(Suzuki *et al.* 2004), and serves as a platform for the remaining self-assembly. The L (Lipopolysaccharide) and P (Peptidoglycan) rings are believed to serve as bushing between the motor and outer envelope. The rod connects the MS ring to the hook, which serves as a universal joint for the rigid filament, allowing filaments from different motors to bundle and rotate (Samatey *et al.*, 2004). Both hook and filament are tubular polymers of a single protein, FlgE and FliC respectively. Apparatus within the C (Cytoplasmic) ring allow these proteins to be exported by diffusion through the hollow rotor, hook and filament for incorporation at the distal end (Minamino and Namba, 2004).

The C-ring constitutes the proteins FliG, FliM and FliN, and is believed to be the site for torque generation (Katamaya *et al.*, 1996). The assembly is also known as the switch complex, since mutations here lead to defective switching phenotypes (Yamaguchi *et al.* 1986ab). FliN is important in assembly and is thought to provide a scaffold for the switch (Dyer *et al.*, 2009). Atomic structures of the *T. maritima* middle and C-terminal domains of FliG, middle domain of FliM and C-terminal domain of FliN have been resolved by X-ray crystallography (Lloyd *et al.* 1999, Brown *et al.* 2002, 2005; Park *et al.* 2006), as well as a peptide version of the *E. coli* N-terminal domain of FliM (Lee *et al.*, 2001, Dyer *et al.*, 2004, Dyer and Dahlquist, 2006). Biochemical studies have provided a model for the locations of these proteins within the C-ring (Lowder *et al.* 2005, Paul and Blair 2006, Paul *et al.* 2006, Brown *et al.* 2007, Park *et al.*, 2006). A partly functional fusion between FliF and FliG indicate that the MS and C-rings are connected and that there are ~ 26 copies of FliG present (Francis *et al.* 1992). Meanwhile there are ~ 34 FliM and ~ 34 tetramers of FliN protein subunits (Thomas et 1999). Various configurations have been proposed to reconcile the mismatch between the FliG and FliM ring symmetries: in one

reconstruction, the C-ring inner lobe shares the MS-ring symmetry, while the outer lobe independently maintains 34-fold symmetry (Thomas *et al.* 2006); another model (Brown *et al.* 2007) suggests that FliG spans both lobes, and that there are ~ (34-26) defects in the outer lobe missing FliG.

In a technique known as 'resurrection', the incorporation of successive stator units into the motor by controlled expression of stator protein leads to step-wise increases in speed, demonstrating that there are ~ 10 torque generating units surrounding the rotor, and that the units function independently and contribute equally to output (Reid *et al.*, 2006). The units continuously turnover during rotation, as observed in a study using labelled units with Total Internal Reflection Fluorescence (TIRF) microscopy (Leake at al., 2006). The average lifetime of a unit is < 1 minute; the reason for turnover is unclear, but exchange might serve the replacement of damaged units. The stator units are unusual among motor proteins for their free energy source: in cells lacking the ability to generate ATP (the common energy currency of the cell, as produced by ATP-synthase, the only other molecular motor known to utilise rotary rather than linear motion) flagellar rotation was restored by the application of an artificial membrane voltage or pH gradient, demonstrating that the motor is ion driven (Manson *et al.*, 1977, Matsuura *et al.*, 1977).

These ion translocating membrane complexes comprise four MotA and two MotB proteins subunits in proton-driven motors such as *E. coli* (Blair and Berg, 1990, de Mot and Vanderlayden 1994, Braun *et al.* 2004, Kojima and Blair 2004), and four PomA and two PomB protein subunits in sodium-driven motors such as *Vibrio alginolyticus* (Sato and Homma 2000). No atomic structures exist for any part of the stator, but cross-linking and site-directed mutagenesis studies have revealed their general topology and function

(Dean *et al.* 1984, Chun and Parkinson 1988, de Mot and Vanderlayden 1994). MotA has four membrane spanning alpha-helices with a large cytoplasmic domain; MotB has one membrane spanning alpha-helix and a large periplasmic domain. The C-terminal periplasmic domain of MotB has a peptidoglycan binding motif, allowing the unit to be anchored to the cell wall. The four alpha-helices of one MotA unit surround a suspected protein binding site at residue Asp32 on MotB (Sharp *et al.* 1995ab); this configuration is expected to form one of two ion channels per $MotA_4MotB_2$ unit (Braun and Blair 2001).

The electrochemical gradient of protons maintained across the inner membrane by respiration provides the free energy source for work. The free energy gain per unit charge crossing the membrane is given by the Ion Motive Force (IMF), which consists of an enthalpic term (due to the electrical potential difference across the membrane) and an entropic term (due to the chemical potential difference across the membrane). Stator unit assembly into the motor is dependent on the existence of an IMF (Fukuoka *et al.*, 2009). Under typical biological conditions, a single ion transit provides ~ 6 k_BT_0, where k_B is Boltzmann's constant and T_0 is standard temperature (compare this to ~ 20 k_BT_0 for the hydrolysis of an ATP molecule) (Sowa and Berry, 2002). Ion transit is expected to coordinate conformational changes in MotA via MotB-Asp32. The cytoplasmic domain of MotA contains two charged residues that interact electrostatically with five charged residues on $FliG_c$, the suspected site for torque generation (Lloyd and Blair 1997, Zhou and Blair 1997, Zhou *et al.* 1998).

1.4.2 Rotation studies

Molecular motors follow mechano-chemical cycles wherein discrete units of fuel are consumed in order to take steps along a discrete track. The cycles of a number of motor proteins have been elucidated, most notably the ATP-dependent procession of Myosin V and Kinesin along actin and microtubules respectively (Yildiz *et al.*, 2003, Yildiz *et al.*, 2004). The evolution of experimental techniques for studying and controlling the rotation of the bacterial flagellar motor has allowed the observation of discretised rotation, providing the first step towards understanding the mechano-chemical cycle between ion flux and the torque-generating conformational changes of a stator unit.

Early studies constructed motor torque versus speed relationships to characterise motor output. The viscous load on the motor, equal to motor torque in steady state rotation, can be controlled by varying the size of a plastic bead (of order 1 μm diameter) attached to the truncated filament of an immobilised cell, and also varying the viscosity of the environment. At the same time, the bead can be used as a marker. Superior position detection to standard video imaging can be achieved with back-focal plane interferometry (Ryu *et al.*, 2000). Here, a weak laser is focused on the dielectric bead, and small changes in bead position are accompanied by shifts in refracted laser light, as measured by a quadrant photodiode in a plane conjugate to the back-focal plane (BFP) of the microscope's condenser.

The zero-load regime was probed only recently (Yuan and Berg, 2008), following the development of an assay in which gold nanoparticles of diameter 60 nm were attached directly to hooks by antibody, in cells lacking flagella. While brightfield imaging collects

15

incident and sample-scattered light, laser darkfield microscopy collects only the scattered light, allowing direct imaging of the readily scattering gold nanoparticles with high contrast to background scattering. A darkfield image of a nanoparticle wobbles, allowing motor speed to be measured by spectral analysis.

The torque versus speed curve is a piecewise continuous function: in the first regime (high motor torque and low speed), the torque is maximum at stall and falls linearly by 10% between 0 Hz and ~160 Hz; in the second regime (low motor torque and high speed) the torque falls linearly and more rapidly, reaching zero motor torque at ~ 330 Hz (Chen and Berg, 2000a; Berg and Turner, 1993; Yuan and Berg, 2008). In the first regime, torque is independent of temperature and solvent isotope effects, while in the second regime, torque is influenced by both factors (Chen and Berg, 2000b). This indicates that chemical transitions are not rate limited at low speeds but that mechanical and chemical transitions are rate-limited at high speeds.

A key development for going beyond the torque versus speed curve came from the genetics front, where the structural similarity between MotA/MotB and PomA/PomB inspired the creation of a hybrid motor (Asai *et al.*, 2003). A fusion protein was made between the periplasmic C-terminal domain of *E. coli* MotB and the membrane spanning N-terminal domain of PomB from *V. alginolyticus*. This chimera PotB was expressed with PomA to form a sodium-driven motor in *E. coli*. The chimeric motor allows for investigation of motor energetics and control of motor rotation: while the electrical potential difference across the membrane depends on pH and must be kept constant to maintain healthy metabolism, the chemical potential difference for the chimeric motor is

dependent on sodium concentration. Motor speed can thus be controlled by varying this concentration (Lo *et al.*, 2006, Lo *et al.*, 2007).

A combination of the above techniques allowed for observation of bacterial flagellar motor stepping (Sowa *et al.*, 2005). Observation of motor steps in BFP interferometry is ordinarily limited by the timescale separation between motor position and bead position due to the filtering activity of the elastic hook. The displacement of a bead upon an instantaneous step in motor position follows an exponential response with a decay constant (the 'relaxation time') given by the viscous drag coefficient of the bead divided by the spring constant of the hook. To observe steps in motor rotation, the step dwell time must be greater than the relaxation time of the marker. Reduction of bead size results in a reduction in relaxation time, but also a decrease in step dwell time as the motor speed is increased. A compromise of using beads of diameter 0.5 μm (with a relaxation time of ~ 1 ms) was selected. Meanwhile, use of the chimeric motor allowed speed reduction to <10 Hz. 26 steps per revolution were observed, in agreement with the periodicity of the FliG track.

1.5 The bacterial flagellar switch of *E. coli*

1.5.1 Molecular details

CheY is a small (14KDa) protein with the typical five-alpha-helix-five-stranded-beta-sheet structure of a response regulator (Volz *et al.*, 1991). The crystal structure of CheY bound to a fragment containing the CheY-binding domain of CheA indicates that binding triggers conformational changes in CheY, presumably necessary for phosphorylation

(Welch *et al.*, 1998, McEvoy *et al.*, 1998). Autodephosphorylation activity, resulting in a CheY-P half life of ~20 s, precludes X-ray crystallography of the phosphorylated state. The C-terminus of CheY is involved in binding CheA, FliM and CheZ and presumably changes conformation upon phosphorylation to recognize FliM and CheZ, and upon dephosphyorylation to recognize CheA (McEvoy *et al.*, 1998, McEvoy *et al.*, 1999, Welch *et al.*, 1998, Zhu *et al.*, 1997). NMR studies (that probe the amino acid electronic environment) indicate that phosphorylation induces conformational changes along most of the protein (Drake *et al.*, 1993, Lowry *et al.*, 1994), although crystal structures of various mutants and analogues of CheY-P implicate only the rotameric state of residue Tyr106 as being critical (Bren and Eisenbach, 2002). These various forms of CheY-P in themselves provide further insight into the protein's function. The mutant CheY13DK binds FliM in vitro and stabilises CW rotation in vivo without phosphorylation (Scharf *et al.*, 1998b), while CheY87TI and CheY109KR remain inactive despite phosphorylation (Appleby and Bourret, 1998, Lukat *et al.*, 1991). This demonstrates that it is conformational change of CheY rather than the presence of a phosphate group that is important for switching.

CheY-P has a reduced affinity for CheA and is released (Schuster *et al.*, 1993), with an increased affinity for FliM (Welch *et al.*, 1994). CheY-P bound to FliM is protected from CheZ-mediated dephosphorylation (Bren *et al.*, 1996), presumably through steric hindrance, given that the CheY binding surface on FliM and CheZ are similar (McEvoy *et al.*, 1999). Biochemical study reveals that CheY-P binds to the 16 N-terminal residues of FliM (Bren and Eisenbach, 1998), although these may not account for the entire binding site (Matthews *et al.*, 1998). Binding of FliM peptides to CheY appears to change

CheY structure, as determined from changes in CheY autophosphorylation rate. Following binding, it is believed that FliM and FliG interact, with FliG communicating FliM state to the motor (Togashi *et al.*, 1997, Matthews *et al.*, 1998, Brown *et al.*, 2002).

A recent study characterised the interaction between soluble fragments of FliM and BeF3-CheY (a stable analogue of CheY-P) and several soluble fragments of FliG, from *T. maritima*, using NMR. The N-terminal domain of FliM (FliM$_N$) was shown to be attached to the middle domain of FliM (FliM$_M$) by a flexible linker and that following binding to FliM$_N$, BeF3-CheY can simultaneously bind to FliM$_M$ by virtue of this linker. BeF3-CheY had only a slightly higher affinity for FliM$_{NM}$ than for FliM$_N$, indicating a low affinity for FliM$_M$. This setup suggests a 'tethered bait' strategy for CheY-P binding, a common mechanism that allows for substrate binding to a secondary site via a high affinity recognition element. Interestingly, BeF3-CheY was found to bind a surface on FliM$_M$ adjacent to the surface used in FliM$_M$ self-association. In the context of an earlier 34-FliM ring model (Park *et al.*, 2006), this occurs on the inside of the C-ring barrel. In that model, switching was proposed to proceed via relative reorientation of the FliM subunits in the ring via re-modelling of the FliM-FliM interfaces. The incursion by the FliM$_N$-BeF3-CheY complex in the NMR study suggests a mechanism for this re-modelling.

The NMR study also revealed that FliM$_M$ binds the C-terminal domain of FliG (FliG$_C$) in close proximity to the surface that interacts with MotA, and at a surface that overlaps the BeF3-CheY binding site. Consequently, it appeared that FliG$_C$ was displaced upon BeF3-CheY binding. It was proposed that this displacement could affect the torque-generating interface between FliG$_C$ and MotA, permissible through a rod-like helix resembling a

hinge connecting $FliG_C$ and the middle domain of FliG ($FliG_M$) (Brown *et al.*, 2002). This molecular model is depicted in Figure 1.4. Indeed, the hinge region is implicated in switching. A mutational study replacing hinge residues generated a group of mutants that were exclusively CCW or CW rotating, lesser or more frequently switching, transiently paused and permanently paused (Van Way, 2004).

In the context of structural models for stator-unit torque generation, two movements of $FliG_C$ relative to the $FliG_M$ rotor perimeter would appear to allow switching. In the crossbridge-type stepping mechanism (Kojima and Blair, 2001), the pair of MotA units closest to the rotor perform power strokes tangential to the rotor perimeter to drive rotation, alternately to ensure a high duty cycle (Ryu *et al.*, 2000). Due to the symmetry of the $MotA_4MotB_2$ complex, the farther pair of MotA units will undergo power strokes in the opposite direction. Thus, a radial movement of $FliG_C$ relative to the rotor perimeter will allow switching between CCW and CW rotation (Figure 1.5, left). Meanwhile, in the piston-type stepping mechanism (Xing *et al.*, 2006) the MotA units perform power strokes parallel to the axis of the rotor. Here, the $FliG_C$ ring presents an inclined saw-tooth surface to serve as a track, with the direction of rotation determined by the direction of inclination. Thus, tangential movement of $FliG_C$ relative to the rotor perimeter will allow switching (Figure 1.5, right).

It is possible to reverse the direction of rotation in non-switching mutants by reversing the ion flux. This was performed with *Streptococcus* using a K^+ diffusion potential (Berg *et al.*, 1982), and with *E. coli* using a voltage clamp (Fung and Berg 1995), indicating that the mechano-chemical cycle of the motor is reversible. However, it is generally agreed
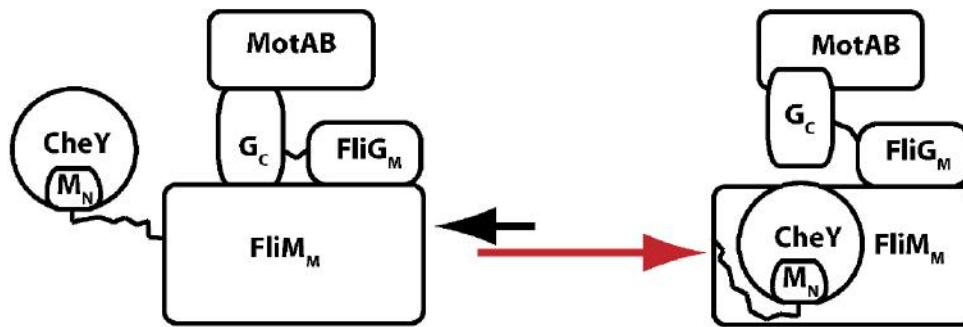
Figure 1.4. Proposed molecular mechanism for switching (figure modified from Dyer *et al.*, 2009). At high CheY-P concentration, CheY-P associates with the high affinity N-terminal domain of FliM (M_N), driving interaction with the low affinity middle domain of FliM ($FliM_M$). The binding of CheY-P at the $FliM_M$ interface results in a displacement of the C-terminal of FliG (G_C) from its $FliM_M$ binding site, resulting in reorientation of G_C relative to the torque generating stator units (MotAB) and a change in the direction of torque.
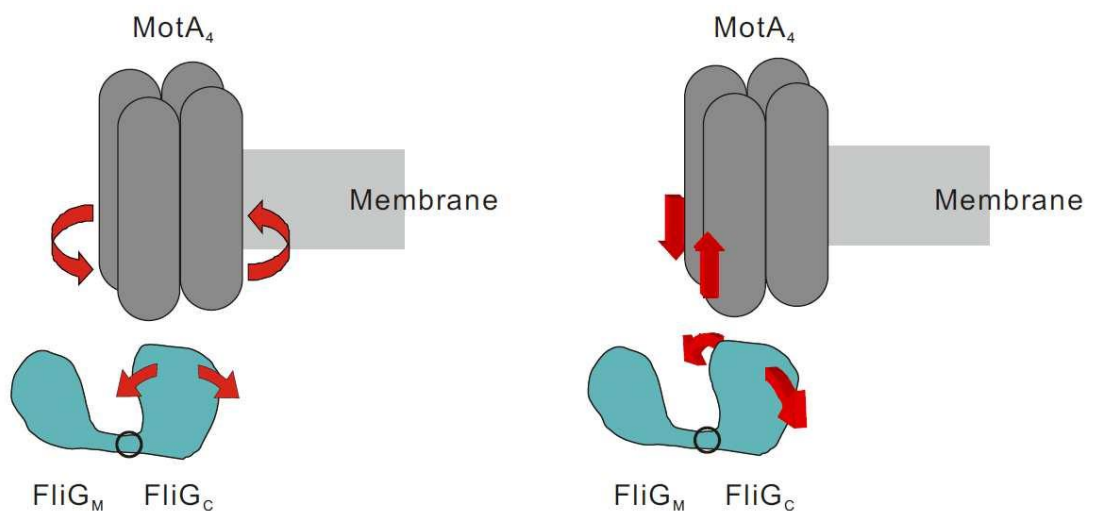
Figure 1.5. Possible conformational changes in FliG resulting in reversal of rotation direction. For clarity, the interaction between just one FliG protein (with the hinge region circled) and one $MotA_4$ complex is depicted. Left: radial movement of $FliG_C$ relative to the rotor results in switching under the crossbridge-type stepping mechanism. Right: tangential movement of $FliG_C$ relative to the rotor results in switching under the piston-type stepping mechanism.

that switching is mediated via conformational changes that affect the direction of torque generation following the binding of CheY-P to FliM, at a constant IMF of ~ -150 mV.

1.5.2 Kinetics

Early models for flagellar motor switching considered deterministic mechanisms in which the direction of rotation depended on the amount of CheY-P bound (Bray *et al.*, 1993, Kuo and Koshland Jr., 1989). Switching was later understood to be a stochastic process. In a tethered cell assay of *E. coli*, CCW and CW intervals were observed to follow exponential distributions down to intervals of length 400 ms (the experimental resolution) (Block *et al.* 1983). The distributions prevailed across exposure to different levels of attractant concentration and even during periods where cells were subjected to continuous chemotactic stimulation. To explain this apparent Markov process, a two-state thermal isomerisation model was proposed in which the CW and CCW states sit in potential wells with free energies G_{CW} and G_{CCW} respectively. Transitions between the wells are governed by thermal fluctuations over an energy barrier of free energy G_T (Scharf *et al.*, 1998a), with rate constants $k_{CW-CCW}=\omega exp[(G_T-G_{CW})/kT]$ and $k_{CCW-CW} = \omega exp[-(G_T-G_{CCW})/kT]$, where ω is the fundamental switching frequency. The ratio of CW state to CCW state probabilities is then $k_{CW-CCW} / k_{CCW-CW} = exp(-\Delta G/k_BT)$, where $\Delta G = G_{CW} - G_{CCW}$.

ΔG in this phenomenological model is a function of both temperature and CheY-P binding. Tethered cells lacking CheY and CheA rotate exclusively CCW, but begin switching if the temperature is reduced to about 10 ºC, with neutral bias achieved at -1 ºC (Turner *et al.*, 1996). ΔG was shown to vary linearly with temperature. An extrapolation

up to 23 ℃ gives ΔG=14.4 k_BT, the energy difference between CW and CCW states in the absence of CheY-P. At constant temperature, and with variable expression of the double mutant CheY(D13K Y106W) (known as CheY**), which is active without phosphorylation, it was found that ΔG decreases by about 0.8 k_BT for each molecule of CheY** bound, with the CCW state rising and CW state falling by about 0.4 k_BT (Scharf *et al.*, 1998a). This was determined assuming Michaelis-Menten binding to 26 FliM sites. A study combining the two variables of CheY** concentration and temperature found that Δ(ΔG) for each molecule of CheY** bound varies linearly from 0.3 k_BT at 5 ℃ to 0.9 k_BT at 25 ℃ (Turner *et al.*, 1999). Curiously, at high temperature the study revealed the inability of CheY** to achieve high CW bias over the standard concentration range.

BFP interferometry of beads attached to unsheared filaments demonstrates long term variation in bias on the timescale of minutes to hours (Korobkova *et al.*, 2004). The variation in bias was confirmed by calculating the 'instantaneous' bias of a record over time, using a 30 second running window. The associated motor interval distributions follow a power law, with an excess of longer intervals compared to an exponential distribution. This behaviour was attributed to the slow fluctuations in the methylation system: expression of saturating CheR or use of mutants with fixed receptor activity restored constant bias and the traditional exponentially distributed intervals. It has been suggested that power-law switching may lead to a more efficient exploration of the bacterial environment compared to Markov-switching (Emonet and Cluzel, 2008). The thermal isomerisation model is able to reproduce power law switching if the CheY-P concentration fluctuates over time (Tu and Grinstein, 2005).

Consistent with the thermal isomerisation view, the transitions between CW and CCW states appear to be near-instantaneous, implying that the switch complex undergoes a concerted quaternary conformational change. This was established in an early experiment using laser darkfield microscopy (Kudo *et al.*, 1990). While standard darkfield microscopy images the entire flagellum, laser darkfield images only components of the filament helix normal to the incident laser, so that the flagellum appears as a series of bright spots, one for each turn of the helix. The oscillating light intensity passing through a slit perpendicular to the filament image provides motor speed. The study revealed that switches in *S. typhimurium* from ~ 100Hz in one direction to ~ 100 Hz in the other direction were completed in less than 1 ms.

A number of studies have challenged elements of the established switching kinetics described above. An improved experimental resolution allowed tethered cell intervals to be measured down to 35 ms (Kuo and Koshland Jr., 1989). Consequently, a double exponential was revealed, with the knee occurring at ~ 200 ms. Another intervals study was motivated by the concern that the previous distributions may have been constructed from cells of very different biases, masking the true interval distribution (Korobkova *et al.*, 2006). The authors used BFP interferometry of beads attached to unsheared filaments of motors where the level of CheY-P was carefully expressed to obtain intervals at a certain bias. Gamma distributions resulted, highlighting a lack of short intervals compared to an exponential distribution. The gamma distribution *G(n, v)* was interpreted as arising due to a hidden *n*-step Poisson process preceding the switch events, with steps occurring at an average rate *v*.

The two-state nature of switching has been challenged by studies suggesting that pausing represents a third state of switching motors (Lapidus *et al.*, 1988, Eisenbach *et al.*, 1990). To avoid concerns about the possibility of mechanical interactions between cells and coverslip in tethered assays, latex beads were attached to cells with straight filaments, which were consequently immotile and recordable in solution away from interacting surfaces. Pausing was observed, at a frequency correlated with CW bias. None of the chemotactic mutants investigated could uncouple pausing from switching, suggesting that no unique pausing signal exists and that the phenomenon may instead represent failed or incomplete switches. In contrast, other studies maintain the absence of pausing, or question the resolution of the above experiments (Korobkova *et al.*, 2006, Berg, 2002).

1.6 Aim

E. coli has the ability to detect small changes in stimuli concentration over a wide dynamic range, providing the basis for successful chemotaxis. The bacterial flagellar switch is an important component of the network, responsible for controlling the direction of rotation of the bacterial flagellar motor during chemotaxis and partly responsible for the observed amplification.

Despite this, the mechanism behind the switch remains poorly understood, with the early phenomenological models lacking explanatory power in light of increasing experimental detail. Amplification in biology is a hallmark of allosteric cooperativity. We proceed in the next chapter to consider existing models for this widespread protein regulation mechanism, with a view to improving our understanding of the bacterial flagellar switch.

Chapter 2

Hypothesis

2.1 Allosteric cooperativity theory

2.1.1 Background

For most proteins there exists a hyperbolic relationship between the fractional occupancy of substrate-binding sites, *Y*, and substrate concentration, [*S*], as described by the Michaelis-Menten model of 1913. However, the dissociation curve for cooperative proteins is sigmoidal, conferring amplification beyond that possible in a Michaelis-Menten system. This is critical to a wide range of cellular processes.

The relationship was first observed between Haemoglobin and O_2 by Bohr in 1904. A 3-fold increase in [O_2] changed the binding capacity of Haemoglobin 9-fold, from 10% to 90%, allowing the protein to bind the maximum amount of O_2 in the lungs and unbind the maximum amount of O_2 in the tissues. In a Michaelis-Menten system, an 81-fold change in [O_2] would be required for the same effect.

Bohr explained the sigmoidal relationship found for Haemoglobin by postulating that the binding of one O_2 molecule made it easier for the successive molecule to bind: the binding events were judged to be cooperative. The concept of binding cooperativity was developed by Hill in 1913. Rather than considering the standard equilibrium equation

$Hb + O_2 \rightleftharpoons HbO_2$, which leads to Michaelis-Menten kinetics, Hill proposed a hypothetical equilibrium displaying infinite binding cooperativity, where Haemoglobin binds four O_2 molecules at once: $Hb + 4O_2 \rightleftharpoons Hb(O_2)_4$. This provided the sigmoidal dissociation curve $Y = [O_2]^4 / (K + [O_2]^4)$, with the dissociation constant $K = [Hb][O_2] / Hb(O_2)_4$. (In actuality, Hill's sigmoid curve did not agree with experiments. The data were described instead by the dissociation curve $Y = [O_2]^{2.8} / (K + [O_2]^{2.8})$, with $K = [Hb][O_2] / Hb(O_2)_{2.8}$). This general form of the dissociation curve has since been used for curve fitting purposes. The Hill equation, $Y = [S]^h / (K + [S]^h)$, with $K = [P][S]^h / [PS_h]$, can be applied to a cooperative protein, P, to describe the degree of either binding or subunit cooperativity in the system with the Hill coefficient h. For $h < 1$, the system is negatively cooperative, for $h = 1$ the system is non-cooperative (reproducing Michaelis-Menten kinetics) and for $h > 1$ the system is positively cooperative.

The discovery that Haemoglobin could be partially oxygenated ruled out Hill's all-or-none binding mechanism, leading Gilbert Adair to develop the Adair equation in 1924. Adair assumed sequential binding, and explained binding cooperativity by assigning a different dissociation constant to each O_2-bound state. This formulation could successfully reproduce the Haemoglobin dissociation curve. However, the model gave no physical insight into why the microscopic dissociation constants should differ from each other.

2.1.2 Classical models

Physical models for cooperativity were developed in the 1960s following the advent of allosteric regulation theory to explain the mystery of feedback-inhibited enzyme kinetics. Classical mechanisms had simply considered that regulatory ligand shared a common binding site with the enzyme's substrate, causing suppression through steric hindrance at the active site. However, the elucidation that the regulatory ligand was sometimes structurally different from the active site substrate precluded such mechanisms. The problem was resolved by considering a so called 'allosteric' interaction (from the Greek *allos*, "other," and *stereos*, "solid (object)"). Regulatory ligand would bind to a site that is stereospecifically distinct from the protein's active site, and the consequent coupling of conformational changes between the sites would suppress active site substrate binding.

In 1965, Monod, Wyman and Changeux considered allosteric interactions within a multi-subunit protein to explain the cooperative binding observed in Haemoglobin. The assumptions of the MWC model, depicted in Figure 2.1 for Haemoglobin, are:

1) The protein interconverts between two conformations, R and T. Symmetry is conserved during transitions: all the subunits must be in the T form, or all must be in R form (the model is also referred to as the 'concerted model' and the 'symmetry model').

2) Ligand binds with a low affinity to the T form and with a high affinity to the R form.

3) The binding of each ligand increases the probability that the protein is in the R conformation through an allosteric strain on all subunits.
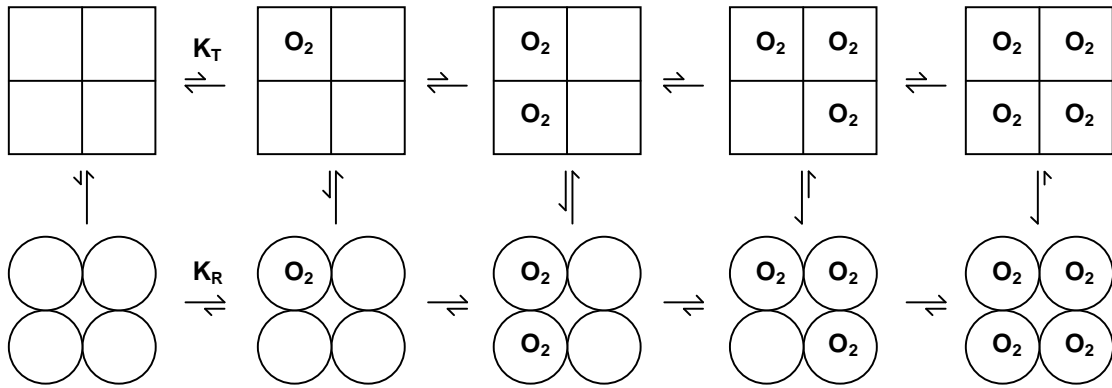
Figure 2.1. Schematic depicting the allowed states of the MWC model as applied to Haemoglobin and binding of O_2. Subunits are either in the T state (square) or R state (circle). The protein undergoes concerted quaternary conformational changes. The dissociation constants (K_T and K_R) differ between T and R states but are independent of O_2 occupancy.
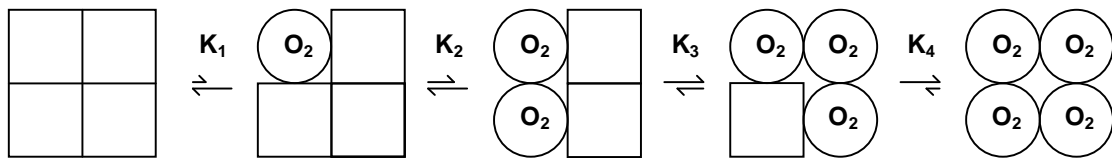

Figure 2.2. Schematic depicting the allowed states of the KNF model as applied to Haemoglobin and binding of O_2. Subunits are either in the T state (square) or R state (circle). The protein undergoes sequential tertiary conformational changes led by changes in occupancy. The dissociation constant varies with bound state.

In 1966, Koshland, Nemethy and Filmer proposed an alternative allosteric interaction. The assumptions of the KNF model, depicted in Figure 2.2 for Haemoglobin, are:

1) Each subunit can exist in a T or R state.

2) The binding of ligand to a subunit induces a change in the conformation of that subunit from a T to an R state.

3) The conformational change of the subunit induces a slight conformational change in neighbouring subunits, affecting their binding affinity (the model is also referred to as the sequential model).

These concerted and sequential mechanisms of allosteric regulation have been of great use in understanding cooperative protein kinetics over the past fifty years (Changeux and Edelstein, 2005, Koshland and Hamadani, 2002). Beyond the details of quaternary transition, the models are distinguished primarily by their differences in the coupling of subunit and binding cooperativity. The fraction of protein molecules in the R form, f_R, as a function of $[S]$ is compared to Y. For the KNF model, where there is a one-to-one correspondence between binding and subunit activity, f_R is equivalent to Y. This is not the case for the MWC model. For a protein molecule with $\alpha = [S] / K_R$, an equilibrium constant $L = [T] / [R]$ (evaluated in the absence of substrate), and a ratio of R state to T state dissociation constants $C = K_R / K_T$, we have:

$$Y = \frac{\alpha(1+\alpha)^{h-1} + LC\alpha(1+C\alpha)^{h-1}}{(1+\alpha)^h + L(1+C\alpha)^h},$$

$$f_R = \frac{(1+\alpha)^h}{(1+\alpha)^h + L(1+C\alpha)^h}.$$

For the MWC model, f_R clearly varies differently to Y as *[S]* increases; that is, the subunit cooperativity (denoted by Hill coefficient h_R) differs from the binding cooperativity (denoted by the Hill coefficient h_Y) (Stryer, 2002).

In those cases where the experimental data do not constrain these differences, and where the protein exhibits positive cooperativity (only the KNF model is capable of explaining negative cooperativity), the MWC model is typically applied for simplicity, being defined by just three variables: the number of subunits, *N,* the equilibrium constant *L*, and *C*. The former two parameters influence sensitivity (the inverse of the substrate concentration resulting in a half maximal response) and amplification (the fractional change in response divided by the fractional change in ligand concentration). If the difference in energy between T and R states is small, then the binding of only a few substrate molecules will induce a transition. The sensitivity therefore grows with *N* and decreases with *L*. In contrast, if there is a large energy difference between the states, the transition does not occur until most subunits are bound. Therefore the amplification, or cooperativity, grows with both *N* and *L* (Sourjik and Berg, 2004).

2.1.3 General model

In 1967, Eigen recognized that the MWC and KNF models were extreme cases in a general scheme of allosteric interactions within multi-subunit proteins. Figure 2.3 represents the scheme for Haemoglobin. Only recently was a mathematical model formulated to describe the full parameter space, leading on from work on receptor amplification in *E. coli*.
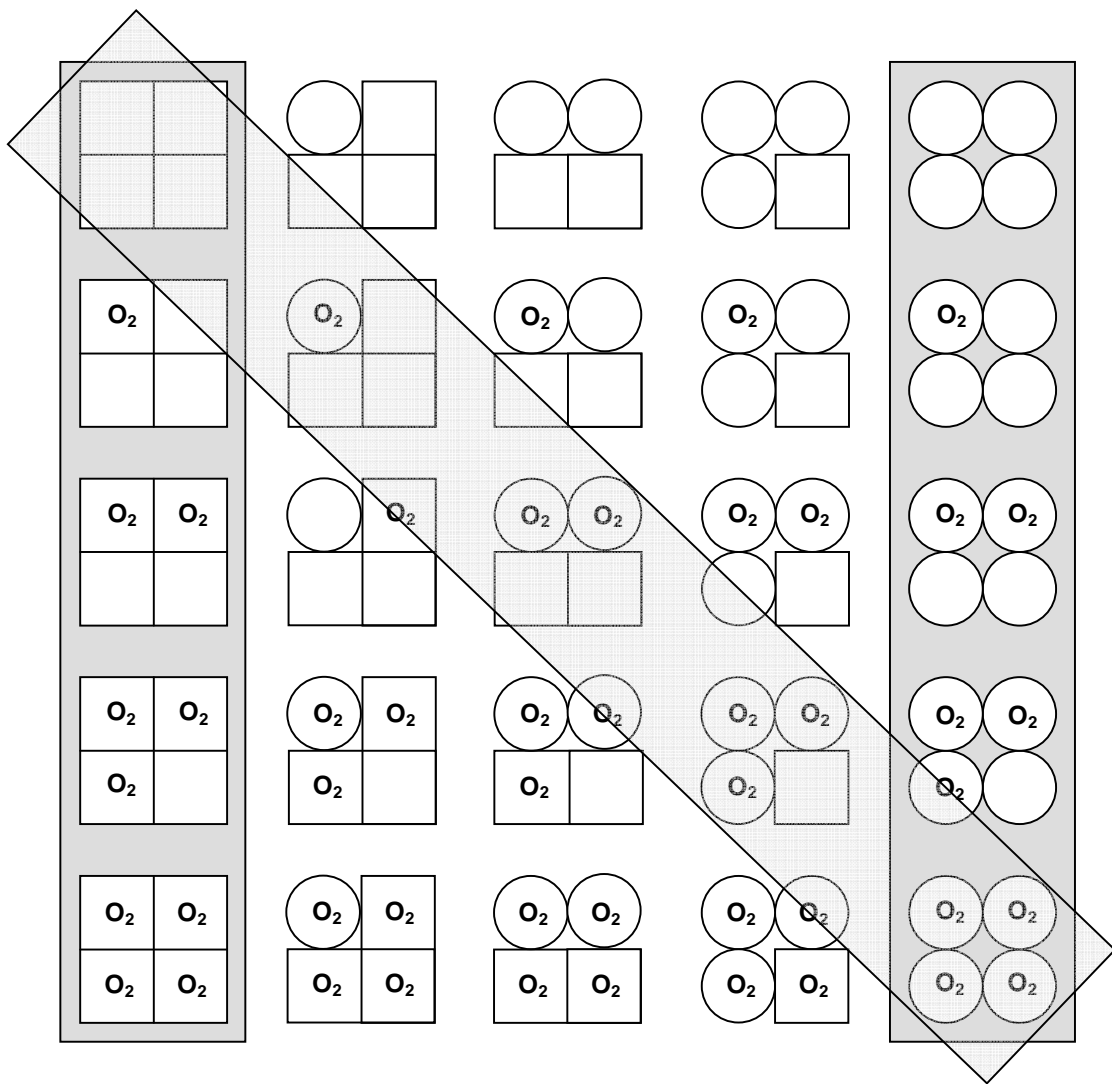
Figure 2.3 The general allosteric scheme depicting the 25 possible states of the Haemoglobin tetramer (N=4), although there are in fact 4^N permutations available, since each subunit may be in a T state (square) or R state (circle) with O_2 bound or not. The states described by the MWC model (dark grey) and KNF model (light grey diagonal) are highlighted.

Following the elucidation of receptor clustering, it was found that the performance of theoretical clusters could be enhanced by considering stochastic conformational coupling between receptors (Bray *et al.* 1998). The idea was later mapped to the two-dimensional Ising model, a classic formulation from statistical mechanics originally developed to explain the resultant ferromagnetic properties of a system by considering magnetic spin coupling. In this framework, receptors underwent probabilistic nearest neighbour interactions on a two-dimensional extended lattice, and analytical mean field solutions (Shi and Duke, 1998) or Monte Carlo based numerical solutions could be obtained (Duke and Bray, 1999). Application of these concepts to a ring of interacting protomers (Duke *et al.*, 2001) provided the grounds for investigating the general model for allosteric cooperativity. The classical models define schemes for coupling between ligand binding and subunit conformation, and coupling of conformations between different subunits. Both models adopt deterministic elements. In the concerted model, coupling between subunits is absolute: all subunits switch conformation simultaneously. In the sequential model, coupling between ligand binding and conformation is absolute: when a ligand binds a subunit, that subunit switches. To access the general parameter space between the classical models both types of coupling must be treated as probabilistic, described as follows.

A 1-D ring of *N* interacting protomers is considered. Each protomer can be in either an *active* (**A**) or *inactive* (**a**) conformation, and it may be bound (**B**) or not bound (**b**) to a single molecule of substrate. This allows each protomer to undergo transitions between four possible states, **AB↔Ab↔ab↔aB↔AB**. The model assumes that the rate constants for a single protomer undergoing a change in activity (**AB↔aB** or **Ab↔ab**) are affected by the conformation of the two adjacent protomers. Since each neighboring protomer

may be either active or inactive, this leads to four pairs of rate constants for each of these changes in activity. The model assumes that the rate constants for CheY-P binding to a protomer, (**AB↔Ab** or **aB↔ab**) are affected only by the conformation of the protomer itself, and that substrate binds the active state more strongly. This general model thus consists of 10 possible reversible transitions for each protomer, as indicated in the free energy diagram shown in Figure 2.4.

A reduced version of the model is obtained by assuming symmetry in the ring. Firstly, the energy difference between active and inactive states is considered independent of ligand occupancy and equal, so that in terms of the energy values specified in Figure 2.4, $(G_2 - G_1) = (G_3 - G_4) = E_A$. Secondly, it is considered that there is no preferred direction in the ring, so the free energy of interaction is independent of activity and equal in either direction. In terms of the energy values specified in figure 2.4, $E_{J1} = E_{J2} = E_{J3} = E_{J4} = E_J$. A free energy diagram for this reduced model is shown in Figure 2.5.

The values of E_A and E_J govern the mechanisms by which conformational change can spread around the ring. As E_A becomes large, binding of CheY-P correlates precisely with activity state – that is, states **aB** and **Ab** are rarely occupied. The limit of very large E_A gives behaviour equivalent to the sequential model of allosteric regulation, where coupling between ligand binding and conformation is absolute. In the limit of very large E_J values, adjacent protomers are energetically forbidden from holding different conformations, leading to behaviour equivalent to the concerted model of allosteric regulation where there is absolute coupling between subunit conformations and all subunits switch simultaneously.
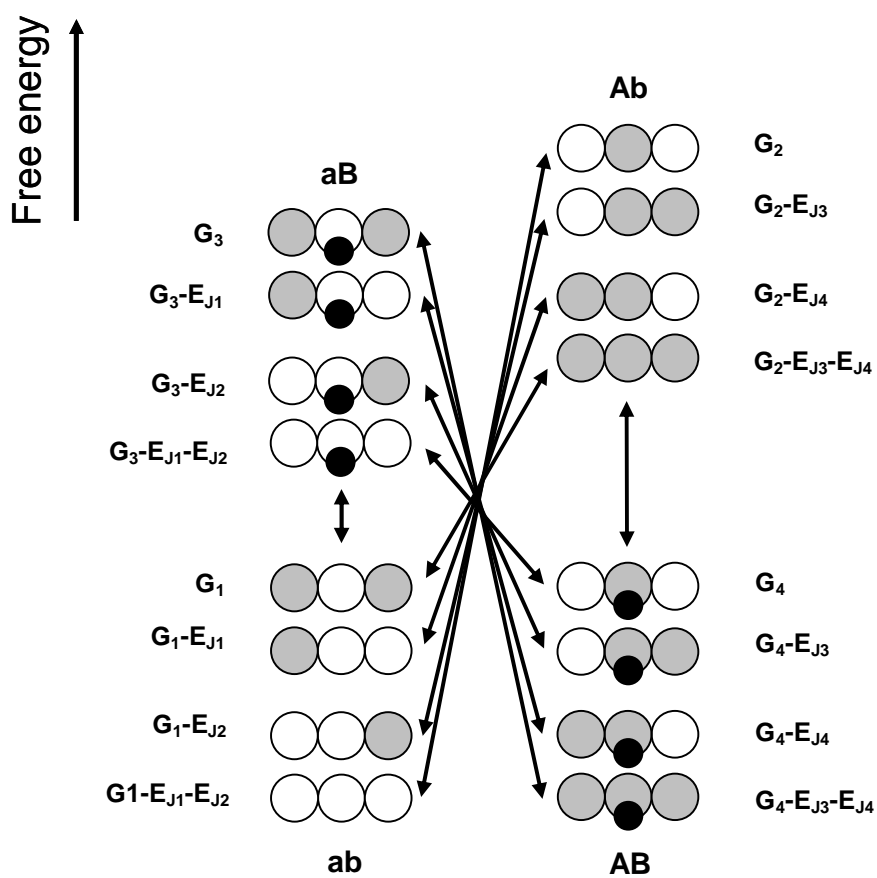
Figure 2.4. Free energy diagram for a protomer (centre of each trio) in the general model for allosteric cooperativity, with energies G_1 (**ab**), G_2 (**Ab**), G_3 (**aB**) and G_4 (**AB**), where $G_1 < G_2$ and $G_4 < G_3$. The diagram is drawn for the concentration of ligand at which the probability of active and inactive states is equal. The free energy of interaction is lower by E_{J1} for a like-inactive protomer to the right, E_{J2} for a like-inactive protomer to the left, E_{J3} for a like-active protomer to the right and E_{J4} for a like-active protomer to the left. Indicated are the four sets of transitions associated with each type of change in activity, and the two sets of transitions associated with change in occupancy.
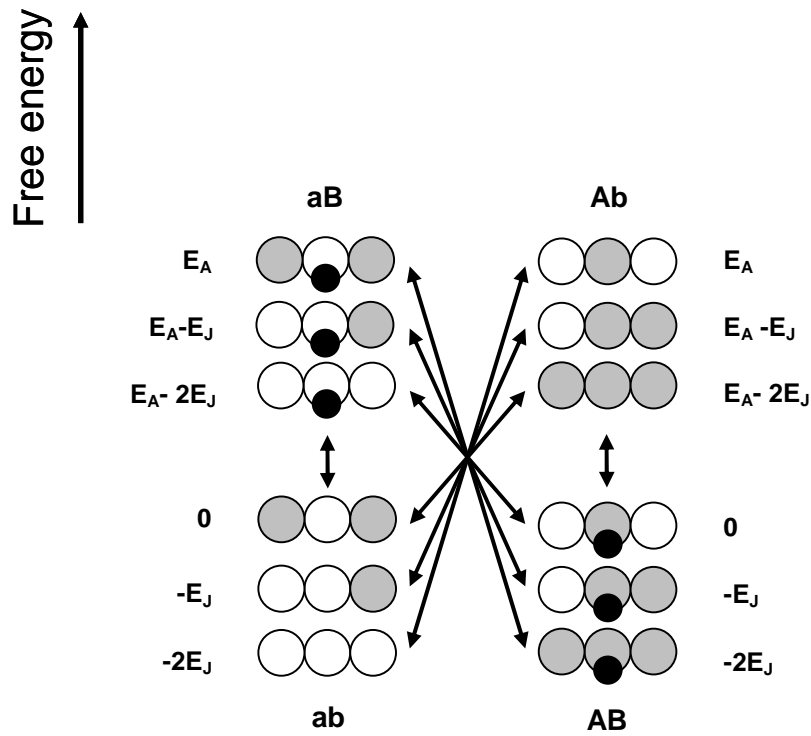
Figure 2.5. Free energy diagram for a protomer (centre of each trio) in the reduced model of allosteric cooperativity, where symmetry has been assumed such that $(G_2 - G_1) = (G_3 - G_4) = E_A$, and $E_{J1} = E_{J2} = E_{J3} = E_{J4} = E_J$. The diagram is drawn for the concentration of ligand at which the probability of active and inactive states is equal.

At other values of E_A and E_J, the model introduces the novel mechanism of conformational spread. At low values of E_J, the ring exhibits a random pattern of states as the protomers flip independently of each other. As the interaction between adjacent protomers is strengthened, domains of like conformational state dominate, until past a critical value, $E_J^* = k_B T \ln N$ (for $N \gg 1$), the behaviour becomes switch-like: the ring spends the majority of time in a coherent state, stochastically switching between fully active and fully inactive configurations. Switches typically occur via a single nucleation of a new domain, followed by conformational spread of the domain, which follows a biased random walk until it either encompasses the entire ring, or collapses back to the previous coherent state (Figure 2.6).

2.2 Application to *E. coli*

2.2.1 Receptors

The early application of two-dimensional conformational spread to receptor clusters was extended in a number of studies to incorporate the effects of receptor modification in adaptation and the presence of heterogeneous receptor populations (Mello and Tu, 2003, Mello *et al.*, 2004, Shimizu *et al.*, 2003). Later studies adopted the MWC model as a convenient approximation (Mello and Tu, 2005): the coupling strength between lattice receptors requires tuning (below the critical coupling strength) in order for the correlation length of interactions to resemble receptor teams; in the MWC model, the team size is simply set as N, and the model is algebraically tractable.
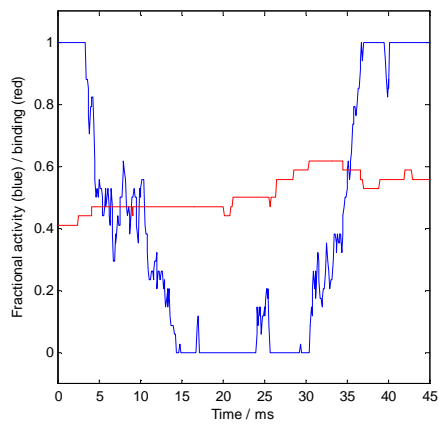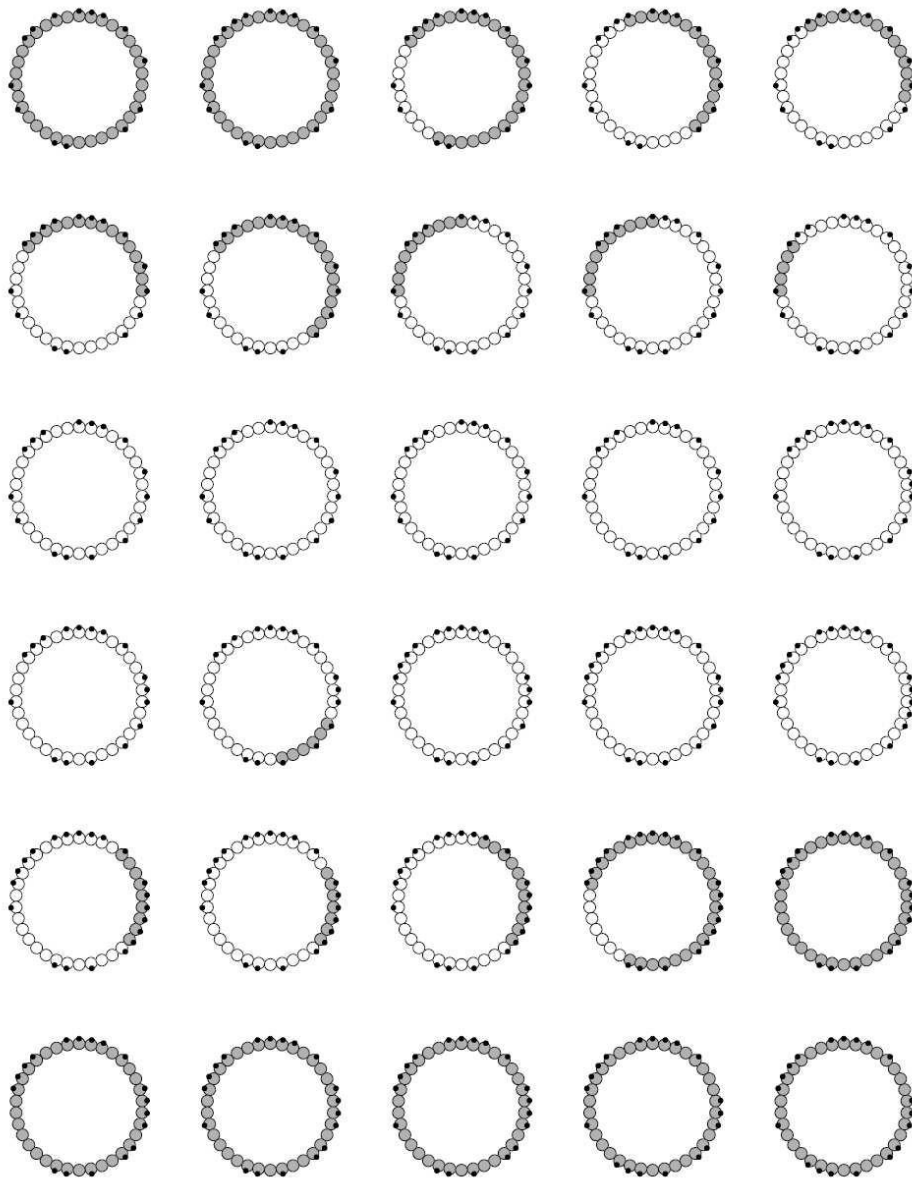
Figure 2.6. Above: Representation of a 45ms conformational spread simulation (see Chapter 5) for a ring with N=34. Increasing time is from left to right, top to bottom. Each image is separated by 1.5 ms. Left: Activity and occupancy over the course of the simulation.

In particular, the functional interactions identified between receptors (Sourjik and Berg, 2004) could be readily explained in MWC terms: increased homogeneity by deletion of other receptor types increases N and therefore sensitivity and cooperativity; meanwhile, increased expression of one receptor type increases *L* and therefore increases cooperativity but decreases sensitivity. The resetting of sensitivity during adaptation was also attributed to a decrease in *L*, achieved by modification of receptors to balance active and inactive states (Sourjik and Berg, 2004, Keymer *et al.*, 2006). A recent study took advantage of the relationship between *N*, *L* and sensitivity to extract the fact that receptor teams are made up of approximately ten trimer units (Endres *et al.*, 2009). The study also found that the team size is dynamic, increasing with receptor modification and ambient concentration, presumably to ensure adequate signal to noise ratios. The MWC approximation appears to be fair in light of evidence pointing to receptors being tightly coupled within teams; for most intents and purposes these teams are two-state systems (Skoge *et al.*, 2006).

2.2.2 Flagellar switch

The elucidation of the high subunit cooperativity ($h_R = 10$) of the bacterial flagellar switch (Cluzel *et al.*, 2000) motivated investigation into binding cooperativity between CheY-P and FliM. An *in vitro* study purified intact complexes comprising FliN, FliM, FliG and FliF, and used double-labelling centrifugation assays to assess binding (Sagi *et al.*, 2003). A lack of binding cooperativity ($h_Y = 1$) was determined. Meanwhile, an *in vivo* study investigated binding using FRET between labelled CheY under variable expression and labelled FliM in single cells (Sourjik and Berg, 2002b). A weak binding

cooperativity was determined (h_Y = 1-2), although it was noted that this may represent an underestimate considering the cytoplasmic pool of FliM unincorporated into motors.

In terms of classical allosteric regulation theory, these results preclude the KNF model and favour the MWC model, as described in section 2.1.2. Further evidence against the KNF model is the ability of motors to switch at low temperature in the absence of CheY (Turner *et al.*, 1999). Indeed, the traditionally observed, binary-like kinetics of bacterial flagellar switching are consistent with the two-state MWC model, which was previously applied to the flagellar switch (Alon *et al.*, 1998) even before the full extent of its cooperativity was made clear (Cluzel *et al.*, 2000).

The conformational spread model has since been applied to the switch (Duke *et al.*, 2001, Bray and Duke, 2006). With estimates for E_A and E_J, the model was able to reproduce the characteristic timescales of switching, and an accurate value for h_R (greater than h_Y). For a complex as large as the flagellar switch, the authors argue that conformational spread would appear to be a necessary extension to the classical models. Here, the instantaneous quaternary transitions of the MWC model seem unrealistic, and indeed, for larger and larger complexes must ultimately breakdown.

Indirect support for conformational spread in the switch over a two-state system has been provided by considering load-dependent switching. Switching as a function of load has been investigated with BFP interferometry of beads with varying size and environment viscosity (Fahrner *et al.*, 2003). At high loads, the CW-CCW switching rate decreased with load, while the CCW-CW rate remained constant, leading to an increase in CW bias with load. Low load switching was investigated by darkfield gold nanoparticle imaging as described in Chapter 1 except that scattered light was split and focused on two

orthogonal slits in front of photomultipliers, providing x and y signals that were converted to motor speed (Yuan *et al.*, 2009). In contrast to the results at high load, both switching rates increased linearly and equally with load, keeping the CW bias constant. Thus switching appears to be sensitive to the two regimes of motor function outlined by investigation of the torque versus speed curve.

In the context of the thermal isomerisation model, to maintain a steady bias while increasing both switching rates, the CW and CCW activation energies must be reduced. A model for switching under load (Van Albada *et al.*, 2008) considered reductions of order $\tau\theta$ where τ is the motor torque and θ is the angular change in orientation of FliG upon switching, leading to switching rates that increase exponentially with torque, in disagreement with experiment. Instead, the linear increase in switching rates was reproduced by scaling the fundamental flipping frequency of flagellar switch protomers in conformational spread simulations by a factor of $exp(\tau\theta/k_BT)$. (An explanation remains to be given for the high load regime).

A more direct route to discriminating between the MWC and conformational spread models concerns the kinetic states of the switch. In contrast to the MWC model, the observable consequence of conformational spread is that switch events should be non-instantaneous with broadly distributed durations due to the biased random walk of conformational spread. Additionally, incomplete switches due to rapid incomplete growth and shrinkage of nucleated domains should be observable as transient speed fluctuations in otherwise stable rotation. At lower time resolution, both models predict exponentially distributed intervals between switch events.

Though classically viewed in binary terms, the kinetic states of the switch, discussed in Chapter 1, are currently unclear: the distribution of motor intervals is disputed, intermediary states in the form of pausing are controversial, and little is known about the mysterious near-instantaneous switch event itself. Consequently, current understanding is insufficient to discriminate between the models. The next chapter describes the steps taken to resolve these issues, allowing an assessment of the underlying mechanism of the bacterial flagellar switch.

Chapter 3

Materials and Methods

3.1 Experimental Procedure and Data Acquisition

3.1.1 Back focal plane interferometry

The time resolution available in flagellar motor experiments is limited by the relaxation time of the hook-marker system following motor displacements. The relaxation time is equal to the viscous drag coefficient of the marker divided by the spring constant of the hook. The viscous drag coefficient for a bead of radius a is equal to $8\pi\eta a^3 + 6\pi\eta a l^2$, where η is the viscosity of the environmental medium, and l is the distance between the rotational axis and the center of the bead. In the tethered cell assay, the cell body itself serves as the marker. Due to its large size and radius of orbit, the associated relaxation time of the system is very large (tens of milliseconds). The relaxation time of a 0.5 μm diameter polystyrene bead attached to a sheared filament rotating about an axis 150 nm from its diameter is about 1.1 ms (Block *et al.*, 1989), the lower limit of time resolution assuming no contribution from the flagellar stub (Ryu *et al.*, 2000). BFP interferometry was the chosen experimental technique for this study.

BFP interferometry relies on the concepts of optical trapping. With the ability to apply pico-Newton forces to sub-micron sized particles while simultaneously measuring displacements with sub-millisecond and nanometer resolutions, optical trapping has

become a widely used technique in the field of biophysics (Neuman and Block, 2004). The following principles may be understood in terms of geometric ray optics for large particles, or far-field interference for particles smaller than the wavelength of the trapping light.

Light passing through dielectric particles is refracted. This results in a reaction force applied to the bead, equal in magnitude and in the opposite direction to the rate of change of photon momentum. For particles with a higher refractive index than the surroundings, and with a steeply focused beam achieved with a high numerical aperture objective lens, a 3-D harmonic potential arises that confines the particle in space (Figure 3.1). Displacements of the particle result in restoring forces and detectable shifts in the angle of refracted light. For low laser power, the restoring force is negligible and the system provides position detection only.

A quadrant photodiode (QPD) in the back-focal plane of the condensing lens can detect shifts in refraction, producing a signal that is proportional to particle displacement. Photocurrents *a*, *b*, *c* and *d* from the four quadrants (clockwise from top-left) provide *x* and *y* displacement as:

$$x = \alpha \frac{(b+c)-(a+d)}{(a+b+c+d)}, \qquad y = \beta \frac{(a+b)-(c+d)}{(a+b+c+d)},$$

where α and β are calibration constants. For displacements much smaller than the laser focus, the response of the QPD is proportional to $(d/w_0)^3$, where d is bead diameter and w_0 is laser beam waist size, which is a function of laser wavelength and objective lens numerical aperture (Gittes and Schmidt, 1998). For 0.5 μm diameter beads, the use of 632
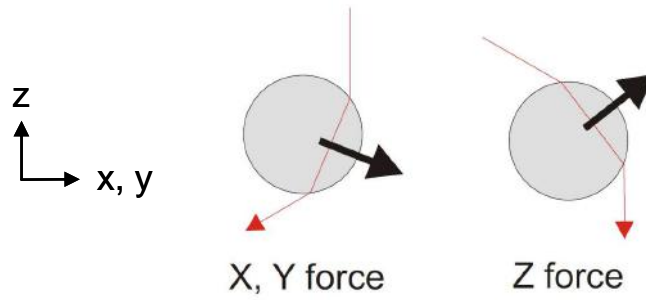
X, Y force   Z force

Figure 3.1 Principle of optical trapping, demonstrated for a dielectric bead with a refractive index larger than the surroundings. Red arrows are light paths, black arrows are the resultant forces. Left: X-Y forces are readily generated by the refraction of light. Right: significant Z forces are generated for incident light with sufficient steepness.
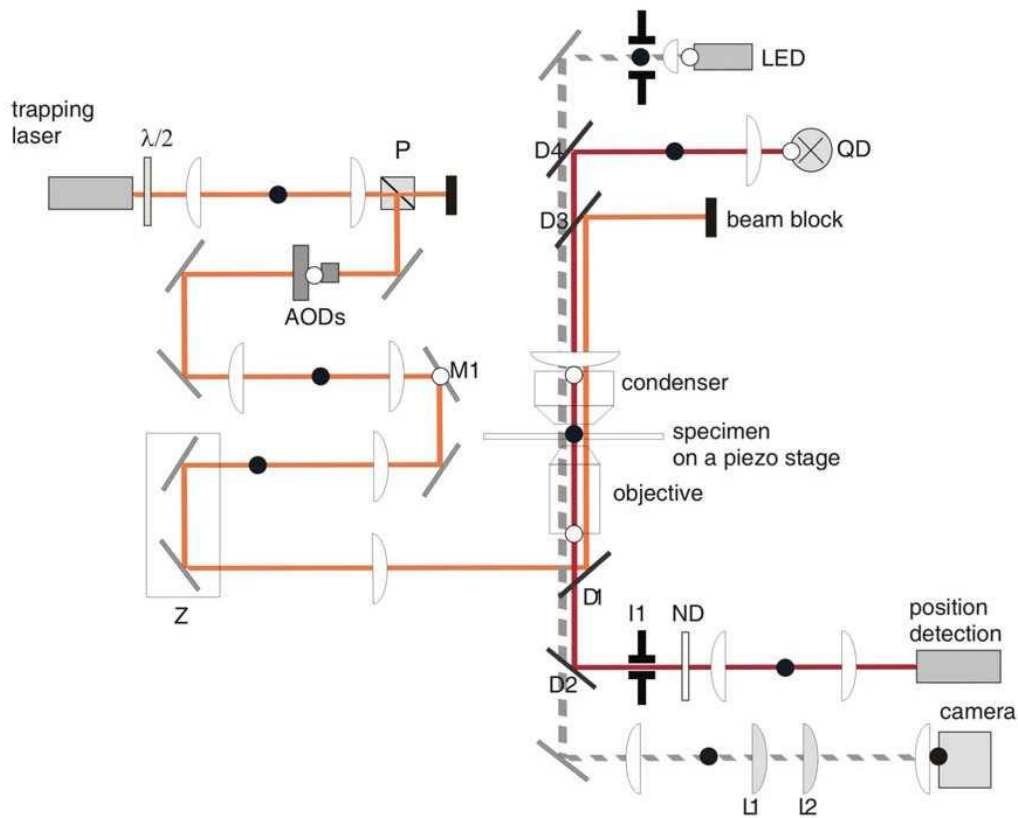

Figure 3.2. Inverted brightfield microscope and dual optical trapping system (figure courtesy of Dr. T. Pilizota). The brightfield light path is indicated by the dashed line. The Helium Neon laser trapping path, used only for position detection at low power, is indicated by the red line. Details of use of these two paths are described in the main text. The Ytterbium laser trapping path is indicated by the orange line. For details of Ytterbium trapping, refer to Pilizota *et al.*, 2007. Planes conjugate to the specimen plane and to the back focal plane of the objective are marked with black and white circles respectively.

nm laser light and a 100x oil-immersion objective with NA 1.3 provides an angular resolution of 1°.

3.1.2 Setup

An existing combined inverted microscope and optical trap system, constructed by Dr. T. Pilizota and Dr. R. M. Berry, was used for all data collection (Figure 3.2). The system has two lasers: a Helium-Neon (632 nm) laser for position detection by BFP interferometry and a near infra-red Ytterbium laser (1064 nm) for optical trapping. The use of the former laser for position detection is described here.

The Helium-Neon laser is first expanded by a telescope system, with the width of the laser into the objective back aperture controlled by an iris. Overfilling the back-aperture provides a diffraction limited spot and maximises the sensitivity of the detector according to the relation of Gittes and Schmidt, 1998, while limiting detector range to bead displacements approximately equal to the laser wavelength. The power level of the laser was attenuated at the back aperture of the objective with two neutral density (ND 1) filters to prevent optical trapping and to minimize photo-damage of the motor. Laser power was approximately 2 mW at focus.

The transmitted beam is collimated by a condenser and expanded to fill the quadrant photodiode to detect bead displacement. The amplified photo-current signals outputted by the quadrants are sampled by a digital signal processing board installed in a host computer. Arbitrary bead time resolution is available depending on sampling rate, but practically, motor time resolution is limited due to the hook-bead system as described above. A sampling rate of 10 KHz was chosen, which required the construction of a

46

4KHz RC filter for anti-aliasing. Illumination for bright-field imaging is provided by a high power red LED. The images were projected onto a CCD camera and displayed on a video monitor.

The sample is mounted on a dovetail stage for coarse 3-axis positioning with a 3-axis piezo-electric stage for fine sample positioning. The entire setup is mounted on an optical air table to damp noise.

3.1.3 Sample preparation

Experiments were conducted with *E. coli* cells wild-type for chemotaxis. Strain KAF84 (*ΔfliC*, *zeb741*::Tn*10*, *pilA*::Tn*5*, pFD313 (*fliCst*, Ap^R)), derived from strain AW405 and plasmid pBR322, was provided as a gift by Prof. H. C. Berg and Dr. K. Fahrner (Department of Molecular and Cellular Biology, Harvard University). The deletion of cell pili (used for twitching motility) avoids interference with bead rotation. The replacement of the filament protein FliC with a mutant allows for the spontaneous attachment of polystyrene beads to the exposed hydrophobic core of the mutant 'sticky' filament.

Cells were grown aerobically from a 100 μL aliquot of frozen stock for 5 h at 30 °C with shaking at 180 rpm, in tryptone broth (1% tryptone; 0.5% sodium chloride) containing ampicillin antibiotic at 100 μM to preserve plasmids. Polystyrene beads of diameter 0.5 μm (Polysciences Inc., Eppelheim, Germany) were attached to truncated flagella of immobilised cells in custom tunnel slides as follows. Flagellar filaments were truncated by viscous shear after passing culture through a narrow gauge needle fifty times. Cells were washed in motility buffer (6.2 mM K_2HPO_4, 3.8 mM KH_2PO_4; 0.1 mM EDTA at

pH 7.0), removing sheared flagella and tryptone broth to prevent filament re-growth. Coverslips were cleaned in a saturated solution of potassium-hydroxide in 95 % ethanol to create a negatively charged surface. Tunnels were constructed by using double-sided tape as spacer between slide and coverslip (Figure 3.3). Poly-L-lysine was wicked through the tunnel with tissue and then flushed out with motility buffer, forming a positively-charged monolayer. The negatively charged bodies of cells results in cell immobilisation. Loose cells were flushed out with motility buffer before adding beads for attachment to flagella. Loose beads were flushed out with motility buffer and the tunnel sealed with grease to prevent evaporation. Full slide protocol details are given in Appendix A.

The same procedure was used to load custom flow slides, which allow for the exchange of cellular environment during experiment. Flow slides were constructed by drilling inlet and outlet holes into a standard slide and attaching polyethylene injection tubes with epoxy-resin. Y-shaped flow slides were constructed in this study to accommodate for two inlets (Figure 3.4). Full slide protocol details are given in Appendix A.

3.1.4 Data collection

Data collection was undertaken in collaboration with Dr. F. Bai (former D. Phil student and postdoctoral researcher in the Berry Group, Department of Physics, University of Oxford). Isolated single cells with wobbling beads were located with brightfield imaging. Groups of cells and beads on visibly large orbits were not considered. Candidate spinners
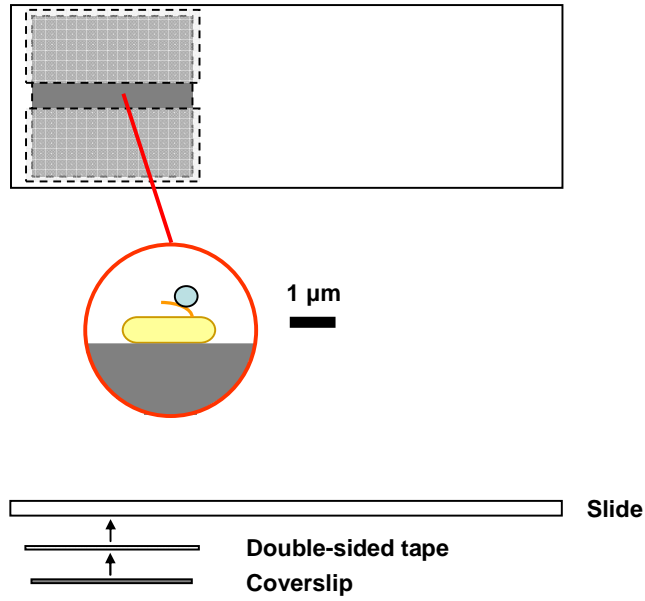
Figure 3.3. Schematic (scale 1:1) showing bottom and side views of a standard tunnel slide. The location of the sample (an immobilized cell with a sheared flagellum and bead attached) on the coverslip surface in the tunnel is shown.
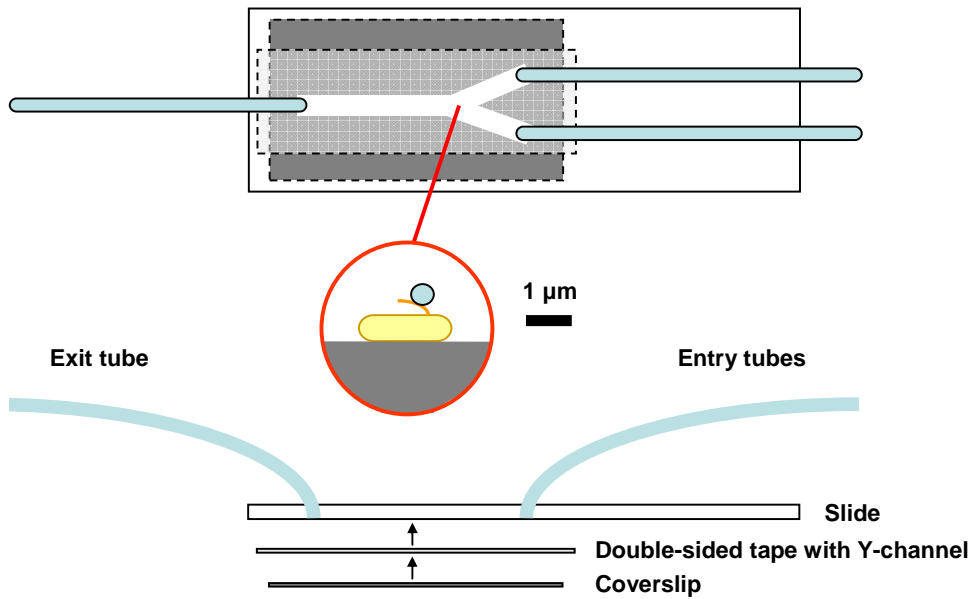

Figure 3.4. Schematic (scale 1:1) showing the top and side views of a flow slide with two inlets and one outlet. The location of the sample (an immobilized cell with a sheared flagellum and bead attached) on the coverslip surface in the Y-shaped tunnel is shown.

were brought into laser focus. Existing QuView software provided a real-time power spectrum giving motor speed and direction of rotation, and a real-time bead spatial trajectory. Beads with steady speed and steady elliptical or circular trajectories were recorded. Each selected cell was recorded for 30 s only, to avoid cumulative laser damage (visible over the timescale of minutes as a steady decline in speed) and slow fluctuations in bias that may confound motor intervals analysis (Korobkova *et al.*, 2006). Measurements were taken from a single slide for no longer than three hours. All experiments were performed at 23 °C.

Cells were categorized by bias. The CW bias was calculated for each 30 s cell record as the fraction of the record spent in the CW state as determined through interval measurement (see section 3.2.4). Bias was observed to vary across the cell population, spanning the entire CW bias range, presumably due to natural variability (Korobkova *et al.*, 2004). To increase the yield of cells with higher CW bias, the technique of attractant removal was applied to a subset of slides to stimulate chemotactic behaviour (Lapidus *et al.*, 1988). Motility buffer (6.2 mM K_2HPO_4, 3.8 mM KH_2PO_4, 0.1 mM EDTA, at pH 7.0) containing an attractant mixture (10μM L-aspartate, 1mM L-serine) was injected into the flow chamber and left for up to 10 minutes. The mixture was then flushed out with plain motility buffer and measurements were taken for up to 10 minutes. Flow chambers allowed a complete exchange of medium in about 5 s. This protocol was repeated for the duration of the experiment. A very marginal increase in the yield of CW bias cells was observed.

3.2 Analyzing Switching

3.2.1 First observations

Using existing LabView software, each sampled bead position, recorded as an (x, y) pair, was converted into an angle and a radius by fitting an ellipse to the bead trajectory (Yasuda *et al.*, 2001), and assuming that trajectories represent the projection of circular orbits onto the focal plane of the microscope (Sowa *et al.*, 2005). Angles were converted to instantaneous motor speed by dividing the difference between successive angles by the sampling time, 0.1 ms. To reduce noise, the record of speed *vs.* time was filtered with a 100 point running median filter, before further analysis. The median filter was chosen over a mean filter, for its edge-preserving ability.

The data show multi-state switching behaviour. Median filtered motor speed records show complete switching between CW and CCW states and incomplete switching to speed levels in between (Figure 3.5). A typical switch event is displayed in detail in Figure 3.6. Filtering, which is required to show the CW and CCW speeds clearly, extends the apparent duration of a switch (left panel), but its finite duration is evident in the unfiltered data (centre and right panel).

In light of the apparent multi-state nature of switching revealed in the data, a framework was developed to quantify the behaviour, with a view to addressing the unresolved kinetic states of the switch, and ultimately to compare experiment with theory.
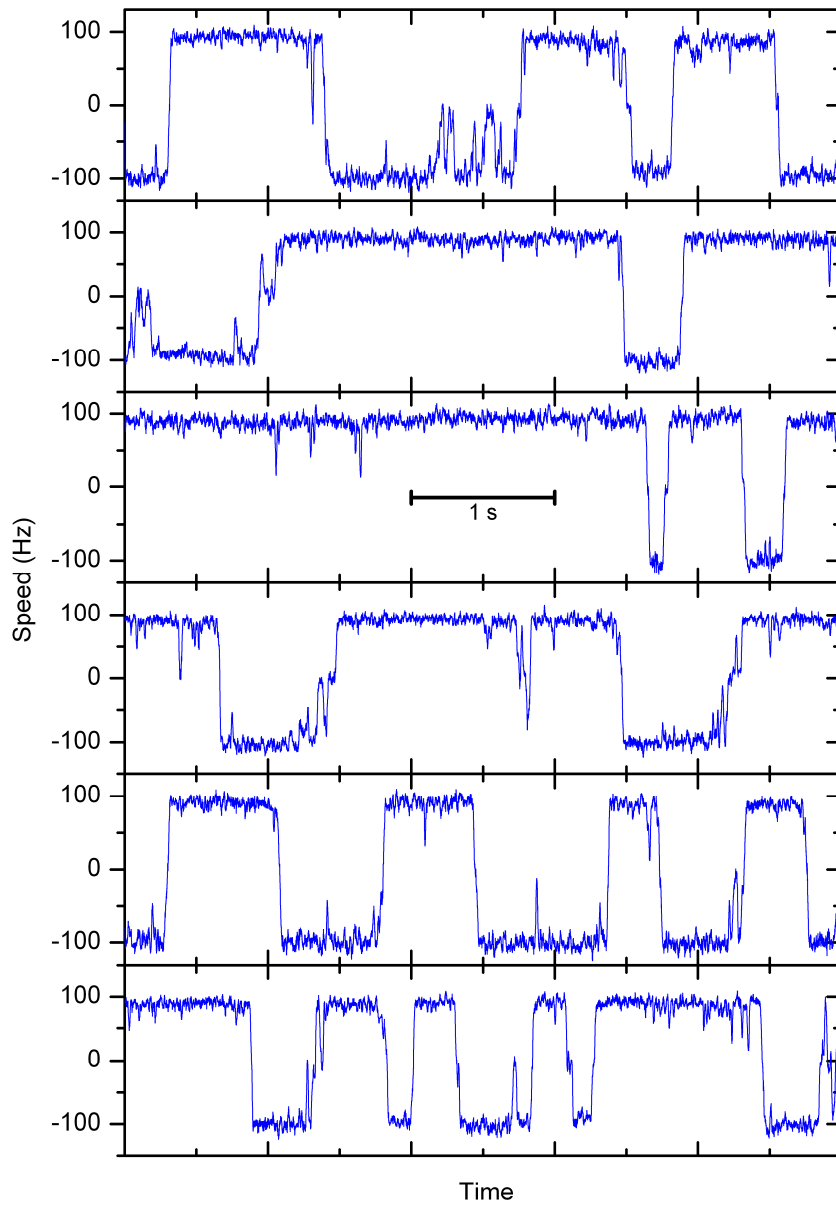
Figure 3.5. A full 30 s motor speed record, median filtered (100 points) to reduce noise. The trace is split into 5 s sections top to bottom. Complete and incomplete switching is evident between CW (negative speeds) and CCW (positive speeds) states.
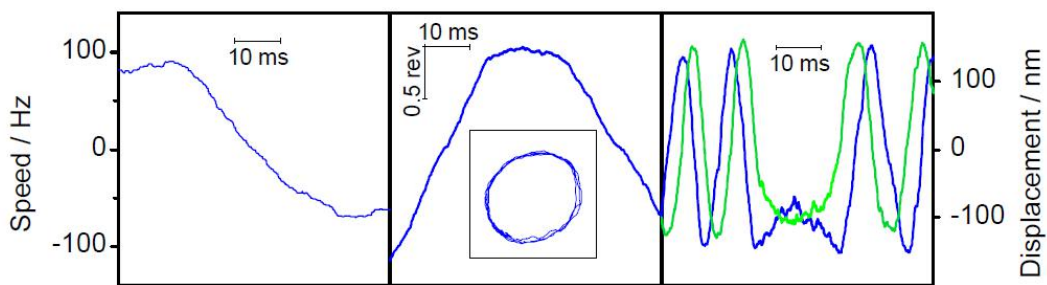
Figure 3.6. Detail of a switch event. Left panel: median filtered speed trace showing a typical complete switch from CCW to CW rotation. Center panel: the same switch shown as unfiltered bead angle versus time. Scale bars show 0.5 revolutions and 10 ms. The switch comprises a linear region corresponding to smooth CCW rotation, followed by a central region corresponding to deceleration, reversal, and acceleration in the opposite direction, and finally another linear region corresponding to smooth CW rotation. The inset shows the unfiltered bead trajectory (x, y) for the same switch, for a range of 400 nm in x and y bead position. Right panel: the same data as the inset in the center panel, shown as unfiltered bead position versus time (x in blue, y in green). Sinusoidal sections of the trace correspond to smooth rotation; the sign of the phase shift between x and y indicates the direction of rotation.

3.2.2 Analysis framework

The problem of analysing multi-state longitudinal time series has been explored in FRET trajectory and ion channel record analysis. A multitude of techniques exist to achieve this goal (Qin and Li, 2004). For a two state series, the most widely used technique is that of zero-crossing thresholding (Reissner *et al.*, 2002, Nekouzadeh and Rudy, 2007), which has been applied in previous studies of motor intervals. Here, positive speeds contributed to CCW intervals and negative speeds to CW intervals. This approach is acceptable for use on binary series, but its application to our multi-state records is inappropriate. Such a scheme cannot deal sensibly with finite switch duration and is problematic when attempting to identify complete and incomplete switching. A zero-speed crossing analysis is also susceptible to high-frequency noise due to multiple crossing of the single threshold during a switch event.

Instead, switching was characterised in terms of a three state model consisting of equilibrium CW and CCW states, and a non-equilibrium intermediary state that is accessed during complete and incomplete switching. This understanding is consistent with the kinetics of conformational spread and provides a natural framework for measuring complete and incomplete switching.

Equilibrium states were defined by the mean speeds of stable CW and CCW rotation. A histogram of filtered speeds in each filtered 30 s speed record was constructed, with bins 0.1 Hz wide. Speed histograms typically showed two peaks, one each for the CW and CCW rotation modes. Because the peak shape is asymmetrically affected by incomplete switching, Gaussian curves were fitted to the outside portion of the histogram peaks to obtain mean CCW and CW speeds, μ_{CCW} and μ_{CW}, and the corresponding standard

54

deviations, σ_{CCW} and σ_{CW}. This fitting was achieved in two steps: for the CCW peak, a preliminary Gaussian fit was made to the data range greater than 20 Hz to provide a mean and standard deviation; a second Gaussian fit was then made to the data range greater than this mean minus a quarter of the standard deviation.

Thresholds for the identification of complete switches were set at $\alpha_{CCW} = \alpha \mu_{CCW}$ and $\alpha_{CW} = \alpha \mu_{CW}$ while thresholds for identification of incomplete switches were set as $\beta_{CCW} = \beta \mu_{CCW}$ and $\beta_{CW} = \beta \mu_{CW}$, with α and β set to arbitrary values (Figure 3.7). Complete and incomplete switching events were then analysed as follows.

3.2.3 Measuring complete switch durations

The procedure for switch duration measurement was developed by F. Bai and is described in this section.

Criteria for selection In order to ensure that data analyzed were attributable to the motor itself rather than extraneous factors, we analyzed only data that satisfied the following criteria. Data from an individual cell were analyzed for switching only if the speed histogram exhibited two modes that could be automatically and accurately fit as described. Then, in order to ensure that each measured switch duration reflects the activity on the ring, a histogram was constructed of the measured radii of all points in the bead trajectory. Only records exhibiting unimodal histograms (judged by visual inspection) were considered, excluding beads that were not stably attached to motors. In addition, after switch duration measurement, the radius of the bead trajectory through the
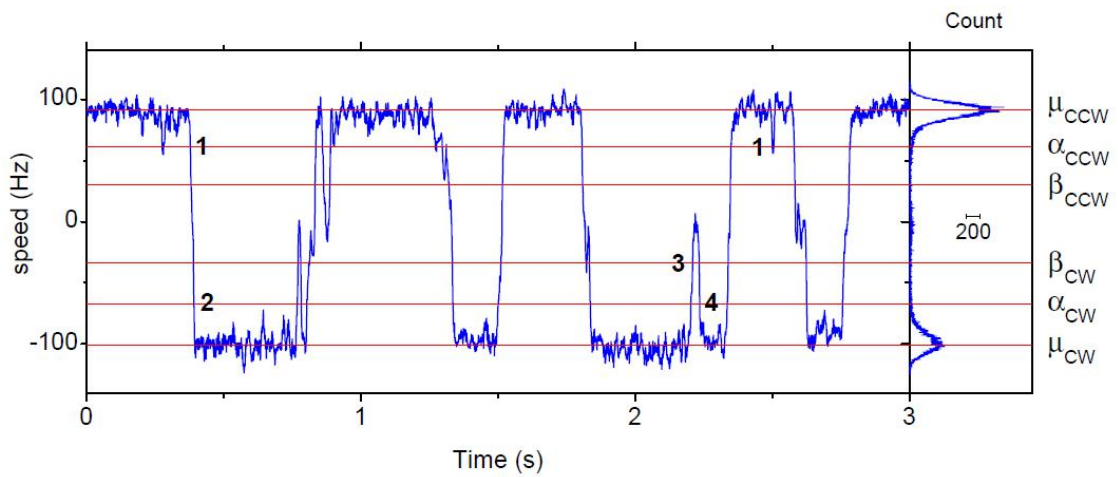
Figure 3.7. Left: three seconds of a typical motor speed record, median filtered (100 points) to reduce noise. Right: the motor speed histogram for the full 30 s record, used to set the α and β thresholds. Indicated are the passages of the thresholds that define switching behaviour. 1 alone: not scored. 1→2: complete switch (CCW→CW). 3→4: incomplete switch from the CW state. Switching from the opposite state is defined similarly.

measured switch was checked to ensure a tight coupling between bead and motor activity. A Gaussian fit was applied to the radius histogram for the entire 30 s record containing the switch. The radius during the switch was monitored from 10 points before the beginning of, to 10 points after the end of, the switch event. The switch was accepted if the radius during the switch was never beyond two standard deviations from the mean of the Gaussian fit to the radius histogram for the entire record.

Duration measurement Complete switches were detected by a custom-written algorithm encoded in MATLAB (The MathWorks, Inc.). CCW and CW thresholds were defined as $\alpha_{CCW} = \alpha \mu_{CCW}$ and $\alpha_{CW} = \alpha \mu_{CW}$ with the parameter α set to 2/3. Complete switch events were located by searching for successive crossings of both thresholds in the same direction in the median-filtered speed record (Figure 3.7). The direction of crossing was used to label the direction of the switch. The midpoint in time of the threshold crossings was saved as the centre point of the complete switch event.

Two 20-point (2 ms) running windows were set to run outwards from the centre point in the bead-angle record. The CCW (CW) window continues until both (a) the slope of a linear fit to the points in the window is above (below) α_{CCW} (α_{CW}), and (b) the root-mean-square error (RMSE) of the linear fit is within the noise profile of the CCW (CW) state.

The noise profile of the CCW (CW) state was defined as follows. A 20-point running window was passed through the entire 30 s bead-angle record (totaling 30 s $\times$ 10 kHz = 300,000 points) and a linear fit obtained for each position of the window. A "noise histogram" was constructed containing the RMSEs of all the linear fits. The shape of the noise histograms deviated slightly from a Gaussian function, with relatively long tails in

the direction of high noise that we attribute to switching and incomplete switching events in the record. We fitted the inner portion of the noise histogram with a Gaussian function and defined this curve as the noise profile of the CCW (CW) state, which is attributed to Brownian motion, the fluctuations produced by the fundamental stepping mechanism, and instrumental noise. If the RMSE of the linear fitting of the window in (b) at a certain position was further than three standard deviations from the mean of the noise profile, we concluded this position was still within a switch event. Since the noise profile varies slightly from cell to cell, noise profile construction was repeated for each record.

Finally, the switch duration was defined as the interval between the inner extremes of the stopped windows. The choice of window size is important: too short and the window lacks statistical accuracy; too long and it is not sensitive to the local change of slope and RMSE. A 20-point (2 ms) window was found to provide an accurate measurement compared to the switch time determined by visual examination of the angular position record and is robust to variations of ±5 points (0.5 ms).

3.2.4 Complete and incomplete switch interval measurement

Criteria for 30 s records used for interval measurement In order to ensure that data analyzed were attributable to the motor itself rather than extraneous factors, we analyzed only data that satisfied the following criteria. Data from an individual cell were analyzed for switching only if the speed histogram exhibited two modes that could be automatically and accurately fit as described. Then, to ensure accurate interval measurement, all records in which beads may have been perturbed by their local environment were excluded as follows. Pauses due to sticking would be expected to

occur at the same angle on successive revolutions, whereas those due to incomplete switching would be randomly distributed. We therefore excluded all records where pauses were found at angles which were inconsistent with a random distribution of pause angle.

The implementation of clustering algorithms to the angle data is inappropriate, since these will always locate an arbitrary number of clusters in a dataset, regardless of whether any clustering exists (Bezdek and Hathaway, 2002). Instead, binomial testing was applied, with the null hypothesis that the angles are uniformly randomly distributed. In each 30 s filtered speed record, pauses were defined as incomplete switches detected using a threshold $\beta = 0.1$ but not detected using a threshold $\beta = -0.1$. The maximum number of pauses, k, detected in a 45° bin swept in 1° increments around the orbit was determined. k was subjected to a binomial test with *p-value= f(k: n, q)*, where *n* is the total number of incomplete switches located and, with the hypothesis of uniformly randomly distributed pausing angles, *q = 45/360*. A confidence level of *0.01* was used. Records where the hypothesis was rejected were deemed to be undergoing mechanical hindrances and were excluded from further analyses.

Complete switch interval measurement Complete switches were detected using the dual-threshold scheme of Figure 3.7, allowing intervals to be defined without sensitivity to incomplete switches that might otherwise skew the distributions toward a shorter timescale. Downward passages across the threshold α_{CW} marked the end of a CCW interval and the beginning of a CW interval while upward passages across α_{CCW} marked the end of a CW interval and the beginning of a CCW interval. The arbitrary value

of $\alpha = 2/3$ provided a sensible compromise between thresholds that were far from zero speed while remaining below the majority of the points in the fitted Gaussian curves.

Criteria for incomplete switch interval measurement Those records accepted for analysis as described above were used here. Detection of incomplete switches is sensitive to both the magnitude of the noise in the speed record and variations in motor speed due to short-term de-energisation and stator changes. To reduce false incomplete switch detection, incomplete switches were searched for within a particular CCW or CW interval only if that interval satisfied the following criteria, which resulted in incomplete switch detection that agreed with visual inspection.

a) The interval was long enough to allow automated Gaussian fitting of the outside portion of the speed histogram, as described, to obtain the mean μ and standard deviation σ of the speed during the interval.

b) The speed noise in the interval was small compared to the threshold for defining incomplete switches; specifically $\mu - 2\sigma > \beta_{CCW}$, where β_{CCW} was the threshold for detection of incomplete switches from the CCW state (defined similarly for the CW case).

c) Speed variations (on a slower time-scale) were small. To measure motor speed variation, a *0.5 s* window was ran across the interval (in *0.1 s* increments) with Gaussian fitting undertaken at each step to provide a set of window mean speeds μ_i. The episode was deemed stable if the range of μ_i was less than 2σ.

Incomplete switch interval measurement Incomplete switches were detected in a similar way to complete switches, using the additional CCW and CW thresholds $\beta_{CCW} = \beta\mu_{CCW}$ and $\beta_{CW} = \beta\mu_{CW}$, with $\beta < \alpha$. Incomplete switch events within a CCW interval were located by searching for a crossing of β_{CCW} followed by a crossing of α_{CCW}, corresponding to a transient reduction of speed by at least the factor of β (Figure 3.7). For the analysis of intervals between incomplete switches $\beta = 1/3$ was used. Similarly, incomplete switch events within a CW interval were located by searching for a crossing of β_{CW} followed by a crossing of α_{CW}. The later of the two threshold crossings was saved as the location of the incomplete switch event.

3.3 Summary

High resolution observation of bacterial flagellar motor switching was achieved by BFP interferometry of polystyrene beads attached to truncated flagellar of *E. coli* cells. Preliminary observations indicate the multi-state nature of the switch. Robust algorithms were developed to provide a means of extracting data of interest from noisy, switching records that experience multi-state activity. These algorithms represent an improvement on published algorithms for analyzing data of such a nature and should be generally useful for analyzing the multi-state longitudinal time series produced by switching motors.

Indeed, the algorithms were successfully adapted for use on switching records from *Rhodobacter sphaeroides* (*R. sphaeroides*). In contrast to the bi-directional motor of *E. coli*, *R. sphaeroides* operates a unidirectional motor, where CCW and stop states equate to the *E. coli* CCW and CW states. BFP interferometry experiments on *R. sphaeroides* by

T. Pilizota and M. Brown yielded records equivalent to those obtained from *E. coli* (T. Pilizota *et al.*, 2009), except at lower temporal and spatial resolution due to the relaxation dynamics of the *R. sphaeroides* flagella and bead assay used. The algorithms were modified and tested for applicability to the records and provided for use.

In the next chapter, we examine the multi-state behaviour of *E. coli*.

Chapter 4

Observations

4.1 Multi-state behaviour

4.1.1 Complete switches

A total of 3570 complete switches were measured according to the criteria and algorithms described in Chapter 3. Switches were observed with a broad range of durations across the population. The fastest were completed in less than 2 ms (Figure 4.1) and appear as abrupt changes in the unfiltered data, completed within a small fraction of the orbit. The duration of these events are close to the lower limit of temporal resolution; indeed, some of the events may be completed faster than is measurable due to the relaxation time of the hook.

The majority of switches have durations of order 10 ms (Figure 4.2). In the unfiltered data, the events typically proceed by a deceleration in speed to the point of reversal, and an acceleration in speed to stable rotation in the opposite direction. These events are visible over a larger portion of the trajectory.

Slower switches take tens of milliseconds (Figure 4.3). In contrast to the majority of switches, these appear more likely to undergo non-monotonic speed variation during the event, visible in both the filtered and unfiltered data. The speed is occasionally observed
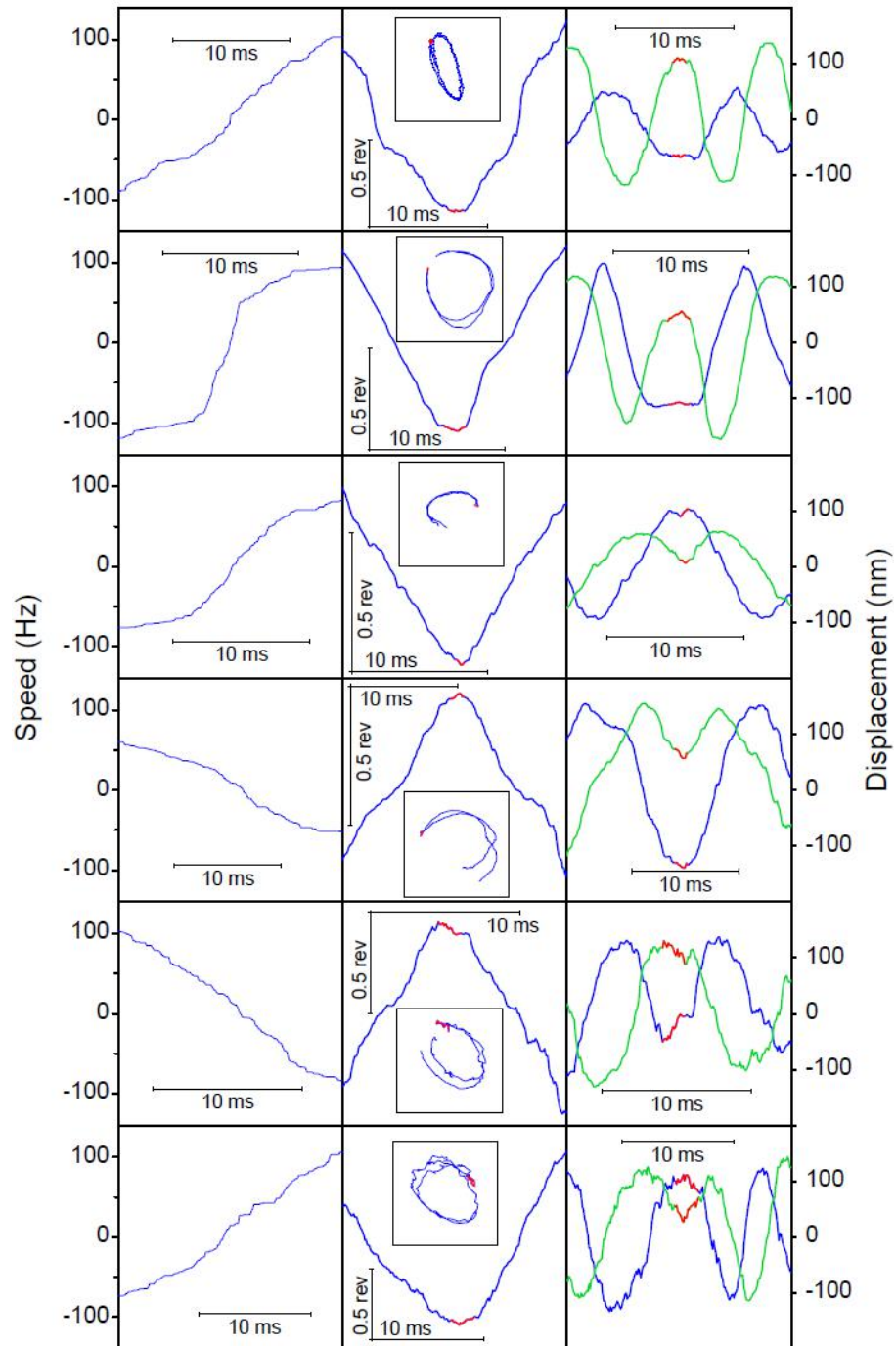
Figure 4.1 Fast switches. Left panels: 100 point median filtered speed trace. Centre panels: unfiltered bead angle trace. The duration of the switch, marked in red, was calculated as the interval during which the bead angle trace was statistically different from the CW and CCW motor states. The inset shows the unfiltered bead trajectory for the same time window. All insets show a range of 400 nm in x and y bead position. Right panels: The same data as the inset in the centre panel, shown as unfiltered bead position against time (x in blue, y in green). Switch durations (from top): 1.1 ms, 1.6 ms, 1.4 ms, 1.2 ms, 1.5 ms, 2.0 ms
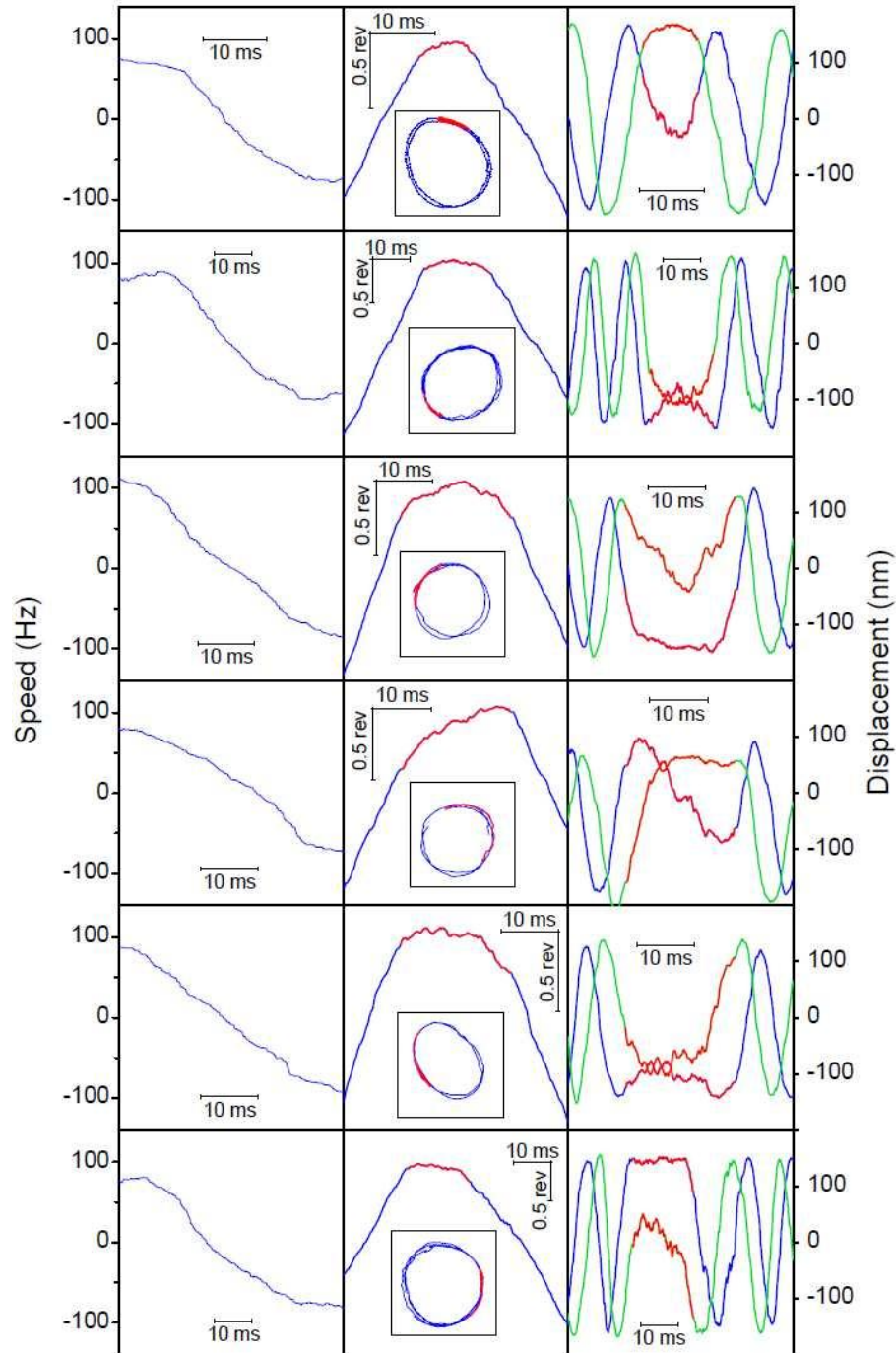
64

Figure 4.2 Typical switches. Left panels: 100 point median filtered speed trace. Centre panels: unfiltered bead angle trace. The duration of the switch, marked in red, was calculated as the interval during which the bead angle trace was statistically different from the CW and CCW motor states. The inset shows the unfiltered bead trajectory for the same time window. All insets show a range of 400 nm in x and y bead position. Right panels: The same data as the inset in the centre panel, shown as unfiltered bead position against time (x in blue, y in green). Switch durations (from top): 8.6 ms, 16.9 ms, 19.4 ms, 18.8 ms, 19.2 ms, 16.2 ms.
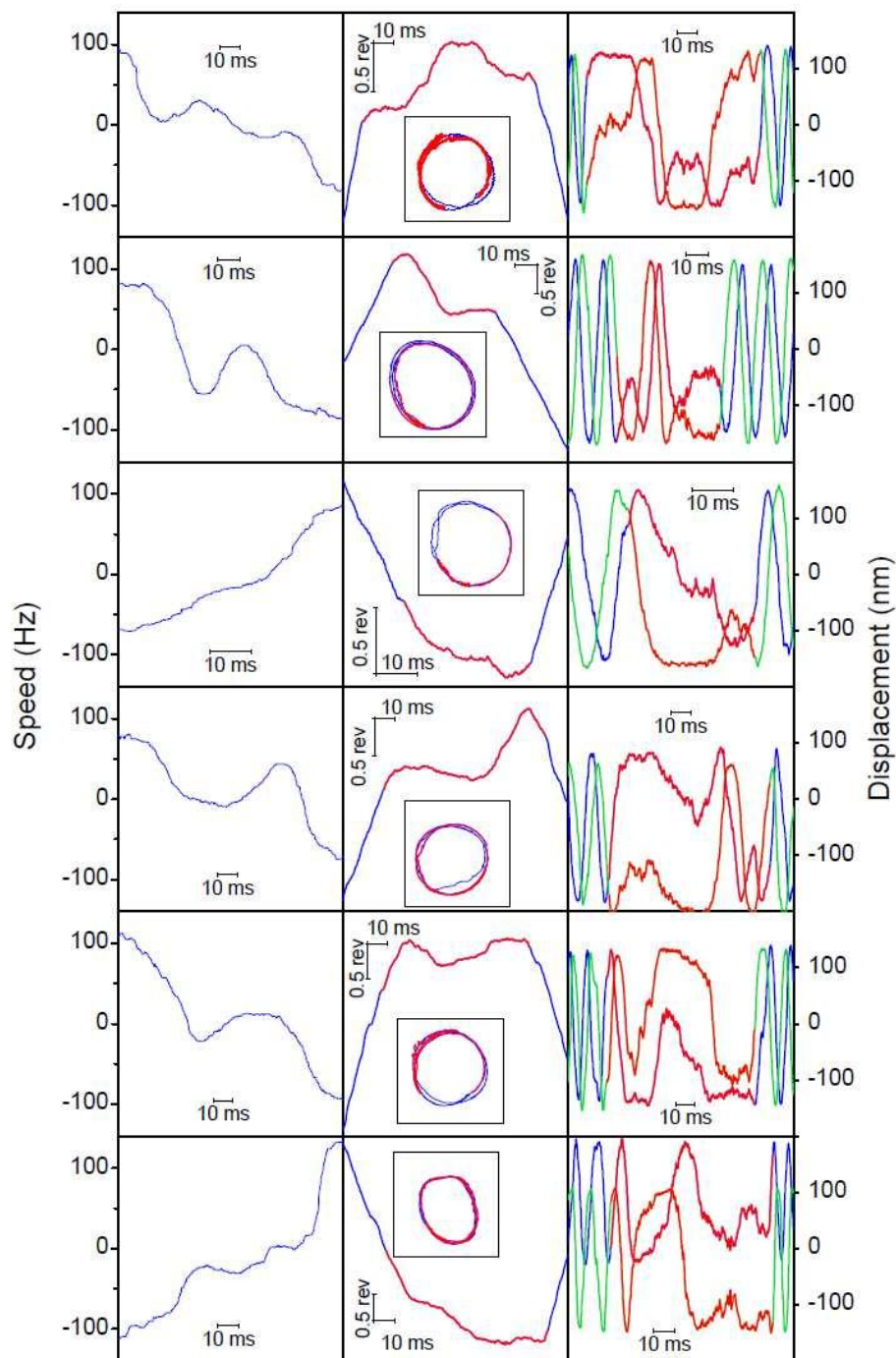
Figure 4.3 Slow switches. Left panels: 100 point median filtered speed trace. Centre panels: unfiltered bead angle trace. The duration of the switch, marked in red, was calculated as the interval during which the bead angle trace was statistically different from the CW and CCW motor states. The inset shows the unfiltered bead trajectory for the same time window. All insets show a range of 400 nm in x and y bead position. Right panels: The same data as the inset in the centre panel, shown as unfiltered bead position against time (x in blue, y in green). Switch durations (from top): 88.1 ms, 42.5 ms, 42.9 ms, 78.4 ms, 76.6 ms, 75.3 ms

to oscillate about zero speed, leading to multiple reversals before completion (clearly evident in the second, fourth and fifth switches shown in Figure 4.3). The unfiltered trajectories show that slow switch events can require almost one revolution for completion, and sometimes more than one revolution. The slowest switches observed take over 100 ms to complete (Figure 4.4). Some of these slow down close to zero speed, but do not appear to actually pause, as evident in the unfiltered (x, y) versus time data.

The distribution of switch durations across the population was constructed to quantify the observed variability. The distribution is peaked, with an average of ~ 20 ms, standard deviation of ~ 15 ms, and mode of ~ 8 ms (Figure 4.5, top). Subsets of the data sorted according to motor bias and switch direction (Figure 4.5) were similarly distributed, showing no clear dependence on either. The peak of the distribution occurs well above the hook-bead relaxation time, so is most likely real. The data are well fitted by a gamma distribution (not shown) and previous studies have attributed physical significance to the distribution fit parameters (Korobkova *et al.*, 2006). However, the observation of the reversible nature of switching rules out the idea that the switch duration distribution can be explained by an irreversible and hidden *n*-step Poisson Process occurring at rate *v*. Rather the peak is simply taken to indicate that there is a characteristic switch duration.

Further to the measures described in Chapter 3 to reduce the possibilities of artefacts, the observed variability in switch duration cannot be explained as an artefact of the elasticity of the hook or variability in the radius of rotation among the population (which would lead to variation in the relaxation time), since switch duration is observed to vary within single cells (Figure 4.6). The radius of rotation is clearly constant between switch events, as is presumably the hook elasticity. The variability within single cells for the population
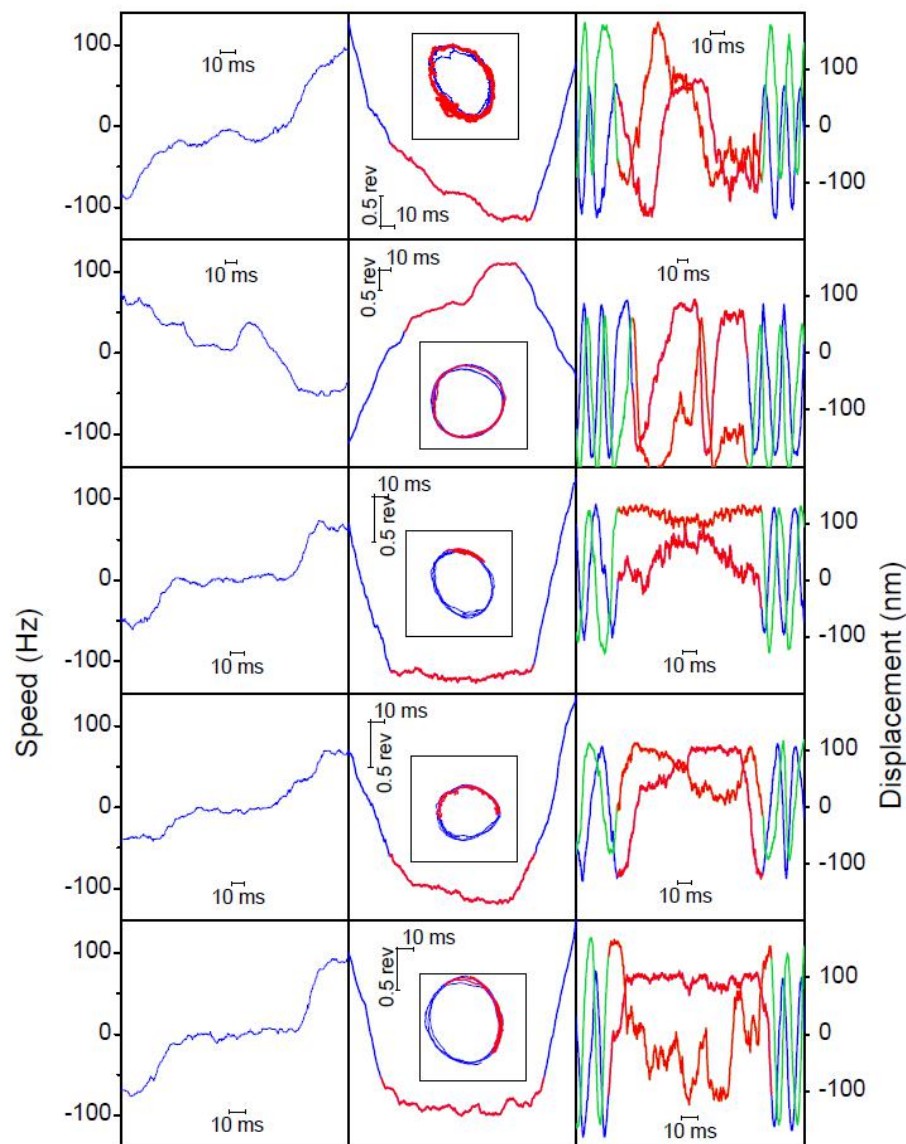
Figure 4.4 Very slow switches. Left panels: 100 point median filtered speed trace. Centre panels: unfiltered bead angle trace. The duration of the switch, marked in red, was calculated as the interval during which the bead angle trace was statistically different from the CW and CCW motor states. The inset shows the unfiltered bead trajectory for the same time window. All insets show a range of 400 nm in x and y bead position. Right panels: The same data as the inset in the centre panel, shown as unfiltered bead position against time (x in blue, y in green). Switch durations (from top): 101.2 ms, 101.5 ms, 100.2 ms, 104.7 ms, 100.2 ms
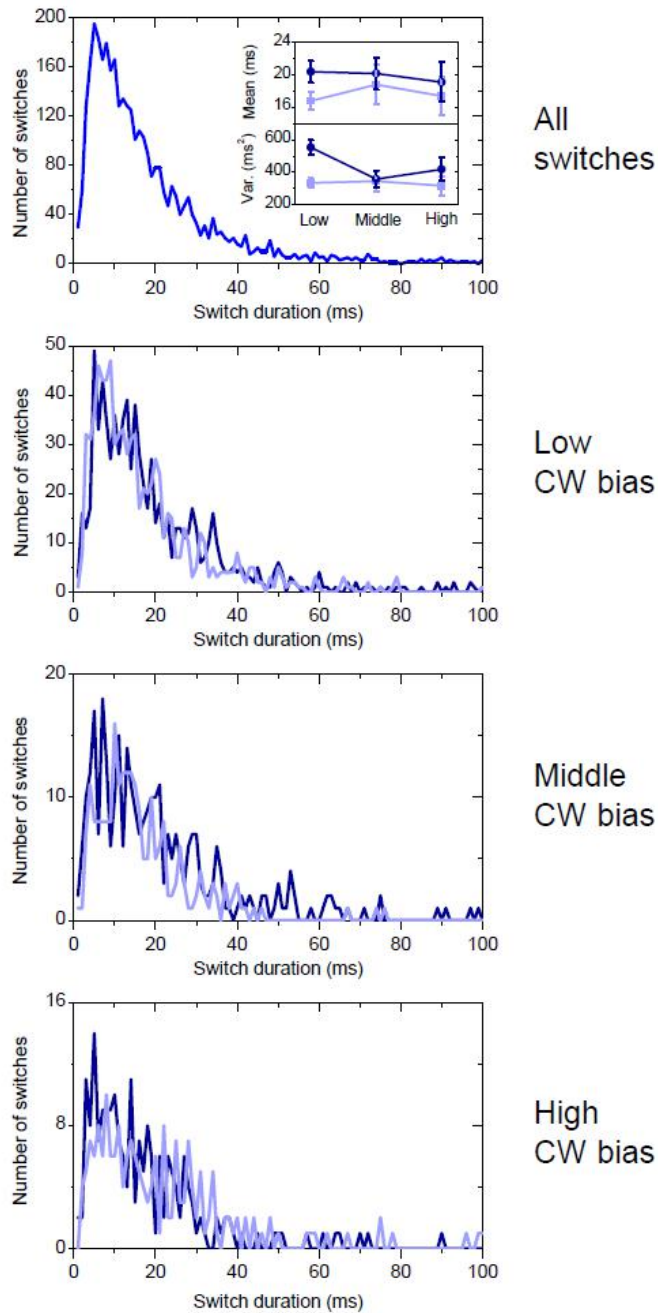
Figure 4.5. Switch duration distributions. Top: Switch duration distribution for all complete switches analysed. Inset, mean and variance of switch durations for CW-to-CCW (light blue) and CCW-to-CW (dark blue) switches for different ranges of CW bias (low = 0 – 1/3, 2459 switches; middle = 1/3 – 2/3, 521 switches; high = 2/3 – 1, 599 switches). Error bars are 99% confidence intervals. The associated distributions are shown in the bottom three panels.
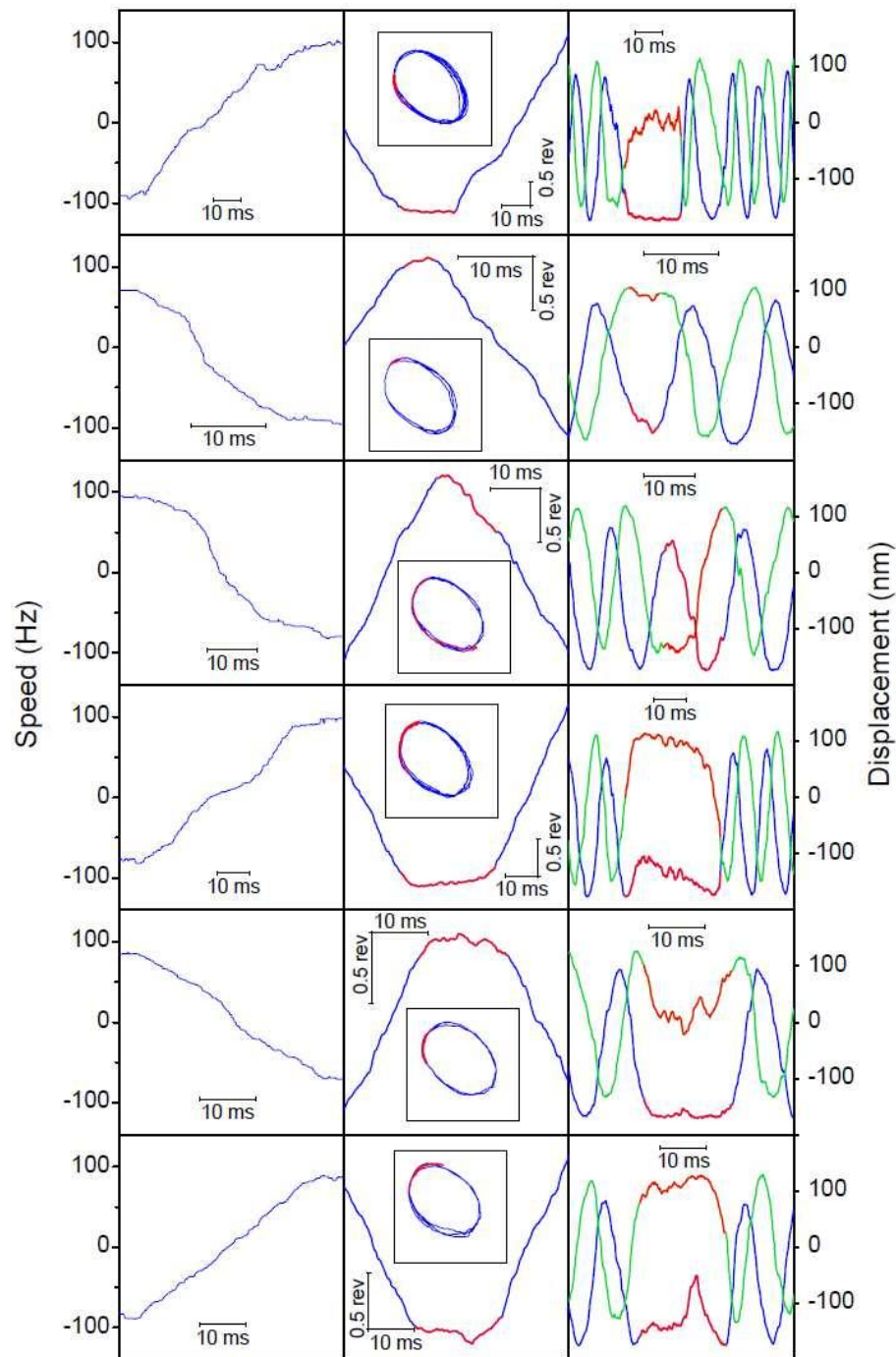
Figure 4.6 All of the 13 accepted complete switches from a single 30s cell record (see next page for the remaining seven switches). Left panels: 100 point median filtered speed trace. Centre panels: unfiltered bead angle trace. The duration of the switch, marked in red, was calculated as the interval during which the bead angle trace was statistically different from the CW and CCW motor states. The inset shows the unfiltered bead trajectory for the same time window. All insets show a range of 400 nm in x and y bead position. Right panels: The same data as the inset in the centre panel, shown as unfiltered bead position against time (x in blue, y in green). Switch durations (from top): 19.8 ms, 3.9 ms, 11.7 ms, 28.7 ms, 15.6 ms, 18.4 ms.
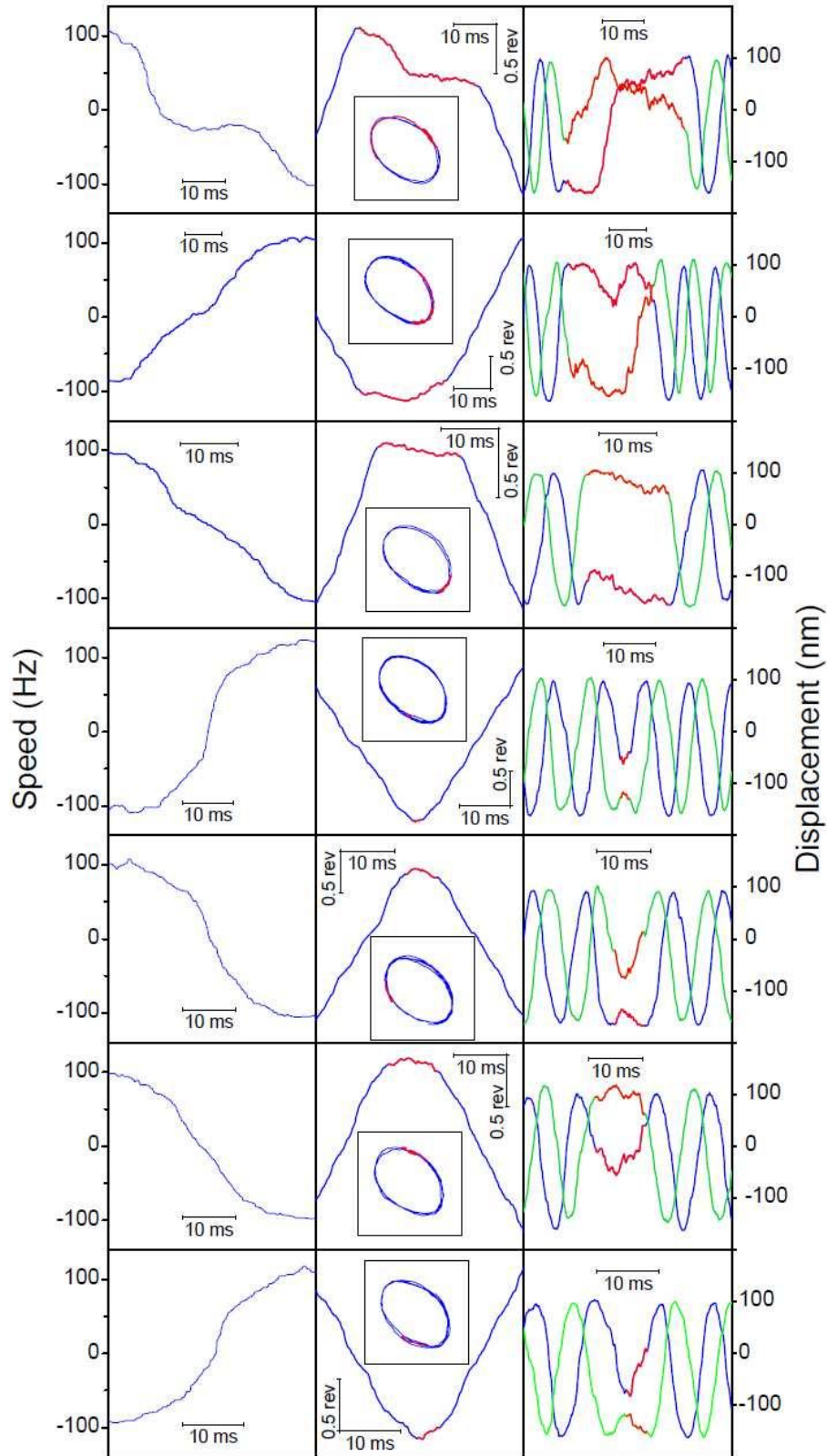
Figure 4.6 continued from the previous page. Switch durations (from top): 27.9 ms 22.9 ms, 14.2 ms, 1.6 ms, 5.4 ms, 9.2 ms, 3.4 ms.

is illustrated in Figure 4.7. Additionally, simulations conducted by F. Bai (using the Langevin simulation described in Chapter 5 with simulated instantaneous switches) indicates that the distribution of hook relaxation time is a tightly distributed gamma distribution with mean ~ 1 ms and standard deviation ~ 0.5 ms. To reproduce the observed population switch duration range, hook stiffness would need to vary between hooks over the full range of 1/10-1/100 of the published value.

Switch durations are not correlated with position of the event in the orbit, ruling out artefacts due to mechanical hindrances. The average magnitude of the correlation coefficient between switch duration and the angle at which a switch begins, assessed for each record with at least ten measured switch events (a total of 80 records), was 0.20. To assess the significance of this correlation, 100 sets of 10-20 pairs of uncorrelated switch durations and angles were generated to represent a 30 s record. Switch durations were drawn from a gamma distribution that fit the experimental switch duration distribution and switch angles from a uniform distribution. The magnitude of the correlation coefficient was calculated for each set, and the average correlation coefficient over the 100 sets was calculated for comparison to the experimental correlations. This was repeated fifty times, giving an estimate of 0.20 ± 0.02 for the magnitude of the average correlation coefficient due to sampling alone. This is equivalent to the experimental value, indicating no true correlations.

These data are in contrast to the previous observation that switches are completed within 1 ms (Kudo *et al.*, 1990). In the two switch events presented in that study, both appear to last about 10 ms by the definitions used for complete switching in this study, in
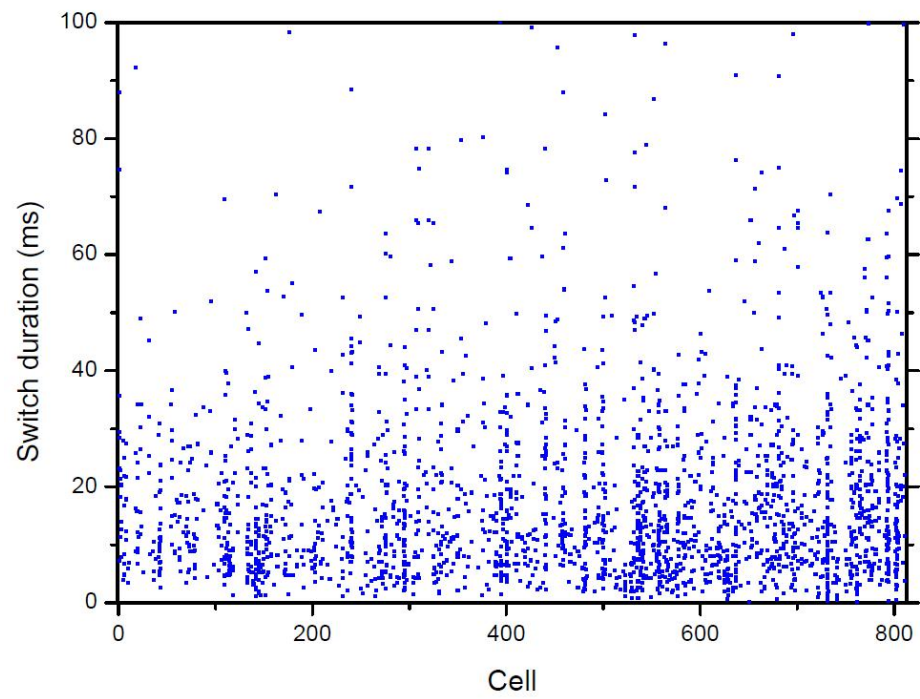
Figure 4.7. Scatter plot of the complete switch durations calculated from each of the 812 motors recorded. Durations are distributed within a single record, across the population range.

agreement with the characteristic duration observed here. It is unclear how the duration of the switch events were determined by Kudo *et al.*

4.1.2 Incomplete switches

Incomplete switches were present in all records. The events lead to transient decreases in speed to a variety of levels, including levels resulting in brief reversal (Figure 4.8). Incomplete switches also display non-monotonic speed variation. Events last of order 10 ms, clearly within the experimental resolution, such that incomplete switches cannot be the artefact of unresolved pairs of complete switches separated by a short time interval. The histogram of speeds for any given record does not clearly identify preferred speed levels, such as pausing. Indeed, during incomplete switch events the point of reversal appears to have no special significance, as was observed during complete switching. Nonetheless, incomplete switches may explain the observation of what were deemed pauses in lower time resolution studies (Lapidus *et al.*, 1988, Eisenbach *et al.*, 1990).

Incomplete switches occur as a Poisson process, as evidenced by the exponential distribution of intervals between events, measured as defined in Chapter 3 with $\beta = 1/3$ (Figure 4.9, left). The mean interval between incomplete switches from the CCW (CW) state increased with CCW (CW) bias (Figure 4.9, right); that is, an incomplete switch is less likely to occur when the flagellar switch is in the favoured state. The number of incomplete switches detected clearly depends upon the parameter β. The mean interval length for the largest data bin (CW bias 0.2) decreased linearly with β, becoming identical to the mean interval length between complete switches (see next section) as β
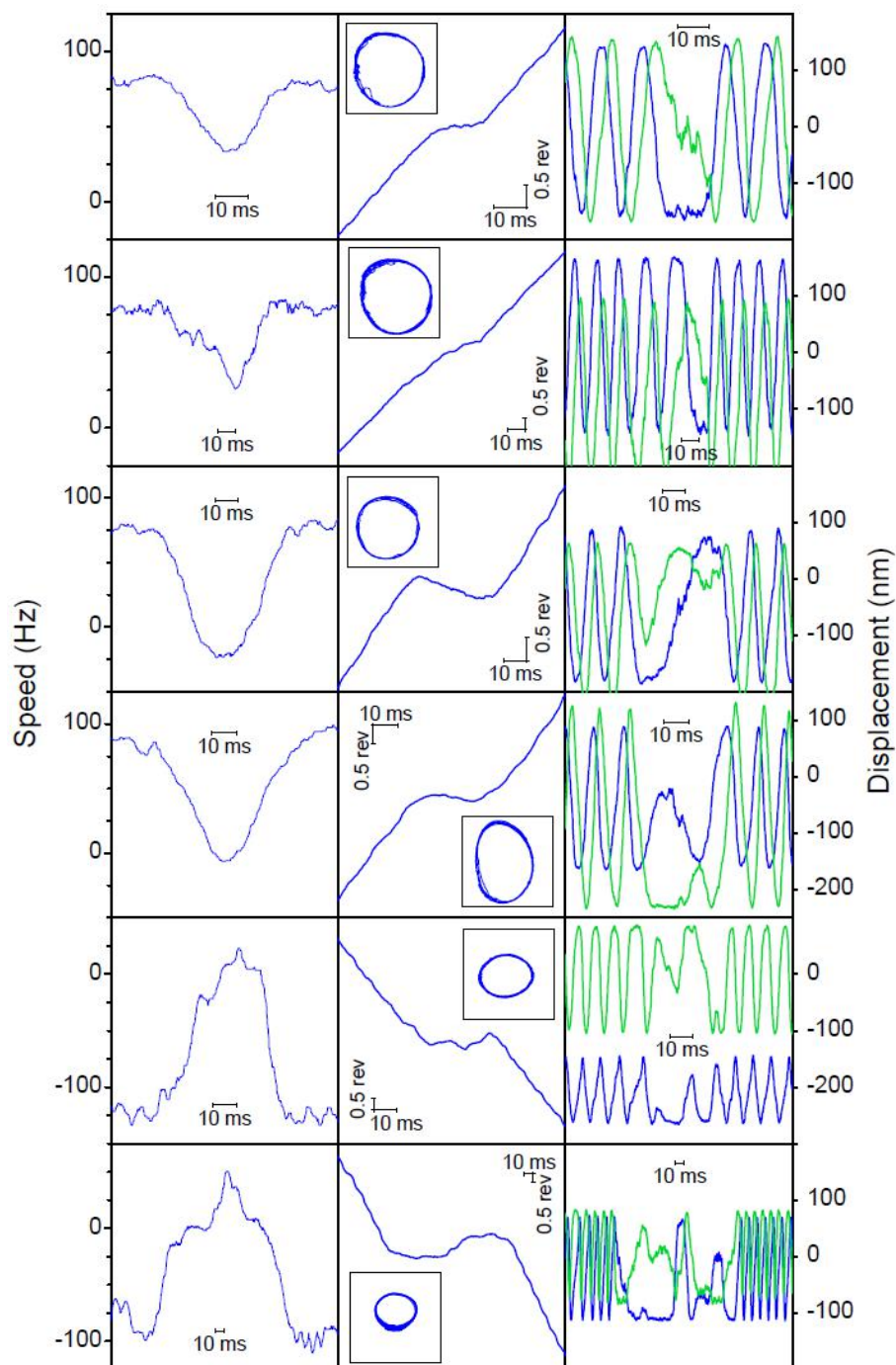
Figure 4.8. Incomplete switches. Left panels: 100 point median filtered speed trace. Centre panels: unfiltered bead angle trace. The inset shows the unfiltered bead trajectory for the same time window. All insets show a range of 400 nm in x and y bead position. Right panels: The same data as the inset in the centre panel, shown as unfiltered bead position against time (x in blue, y in green).
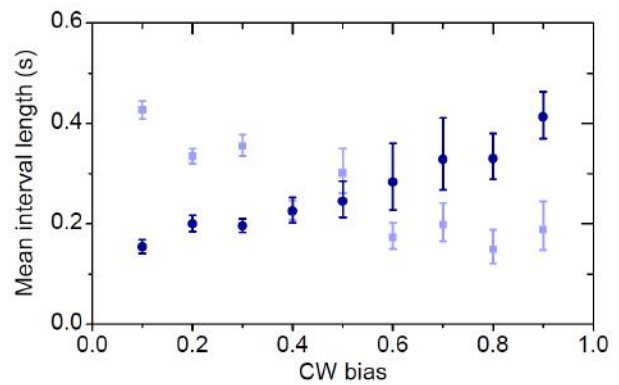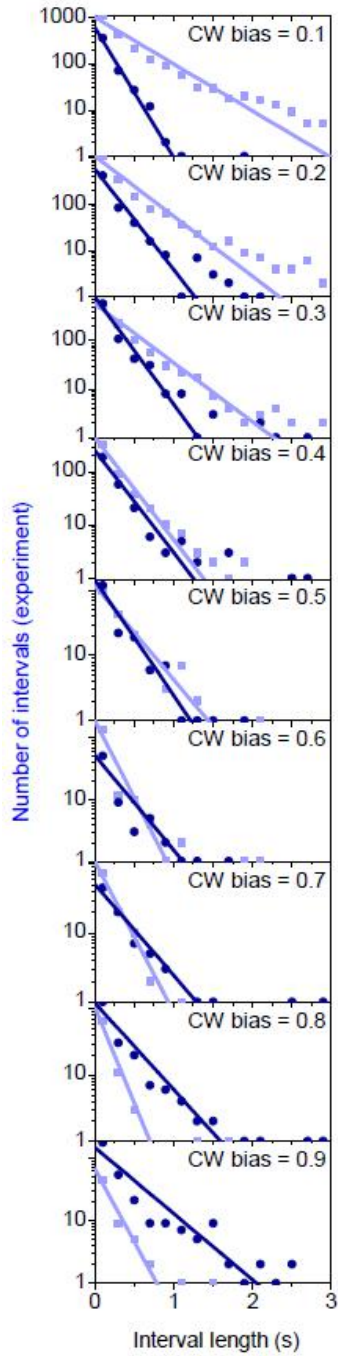
75

Figure 4.9. Intervals between incomplete switches with β = 1/3. CW data are represented by dark blue circles, CCW data by light blue squares. Left: interval distributions across the full bias range (from top to bottom: 0.1± 0.05, 0.2± 0.05, 0.3 ± 0.05, 0.4 ± 0.05, 0.5 ± 0.05, 0.5 ± 0.05, 0.7 ± 0.05, 0.8 ± 0.05, 0.9 ± 0.05). Lines are exponential maximum likelihood fits applied to the full datasets. Right: mean interval lengths obtained from the fits on the left. Error bars are 99 % confidence intervals.

tended to -2/3 (Figure 4.10, left). For these values of β, intervals remained exponentially distributed (Figure 4.10, right).

Further to the measures described in Chapter 3 to reduce the possibilities of artefacts, data were collected from a CheY-deleted and therefore non-switching *E. coli* strain. Strain KAF95 (*ΔcheY*, *ΔfliC*, *zeb741*::Tn*10*, *pilA*::Tn*5*, pFD313 (*fliC^{st}*, Ap^R)), derived from strain AW405 and plasmid pBR322, was provided as a gift from Prof. Howard Berg and Dr. Karen Fahrner. Data were collected in the same way as described for strain KAF84 in Chapter 3, providing a control on whether the observation of incomplete switches arose from artefacts of the rotation assay. Incomplete switches were absent in this strain (Figure 4.11), excluding such a possibility.

4.1.3 Angle clamp experiments

Independent evidence for the multi-state behaviour described in the above sections was obtained by using an optical trap to stall pairs of 0.5 micron beads attached to switching motors. Experimental data were collected by Dr. T. Pilizota and provided for analysis. Bead pairs rotated through ~ 90 degrees in the fixed optical trap provided by the Ytterbium laser (Figure 3.2) when the direction of motor torque reversed, while the Helium Neon laser provided position detection. The set up has a resolution of 1 ms (Pilizota *et al.*, 2007). Complete switches of finite duration and incomplete switching were observed as with rotating beads (Figure 4.12). Due to the low yield of appropriately positioned bead pairs in this technique, an insufficient quantity of data was collected for analysis of complete switch durations. In any case, due to the load dependent nature of complete switch frequency (Fahrner *et al.*, 2003, Yuan *et al.*, 2009) the distribution for
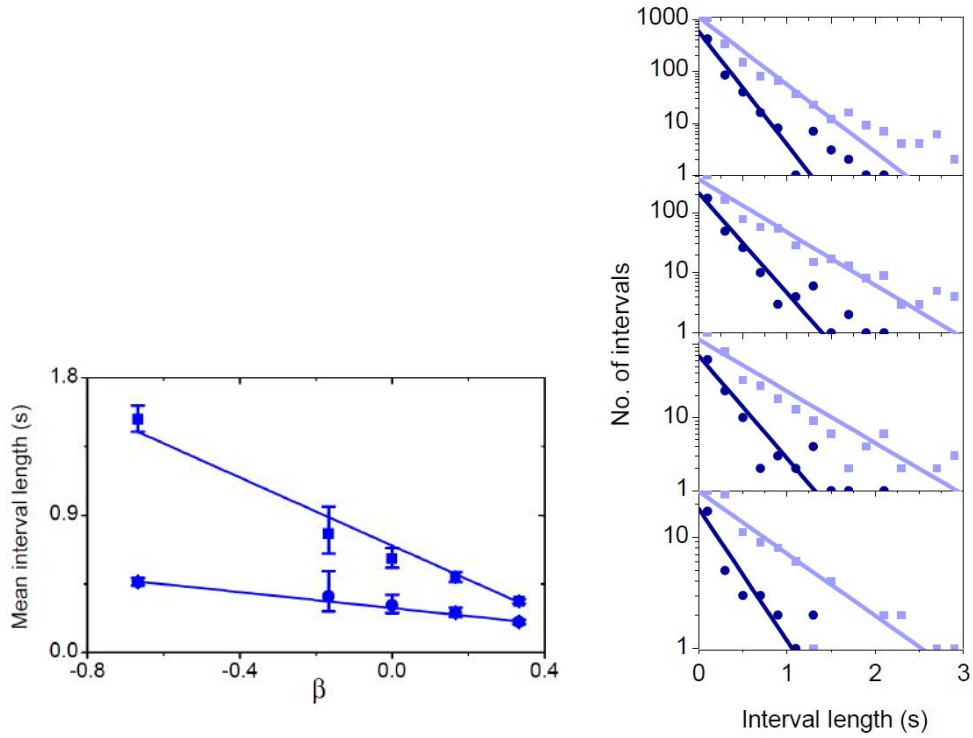
Figure 4.10. Incomplete switch interval dependence on β. CW data are represented by dark blue squares, CCW data by light blue circles. Left: linear variation of mean interval lengths between incomplete switches for the CW bias bin with the largest dataset (0.2 ± 0.05) with β. Mean interval lengths are obtained from the fits on the left. Also plotted are the mean complete switch interval lengths (see section 4.2), equivalent to an analysis with $\beta = -2/3$. Error bars are 99 % confidence intervals. Right: distributions of intervals, with varying β (from top to bottom, $\beta = 1/3, 1/6, 1/1000, -1/6$). Lines are exponential maximum likelihood fits to the full datasets.
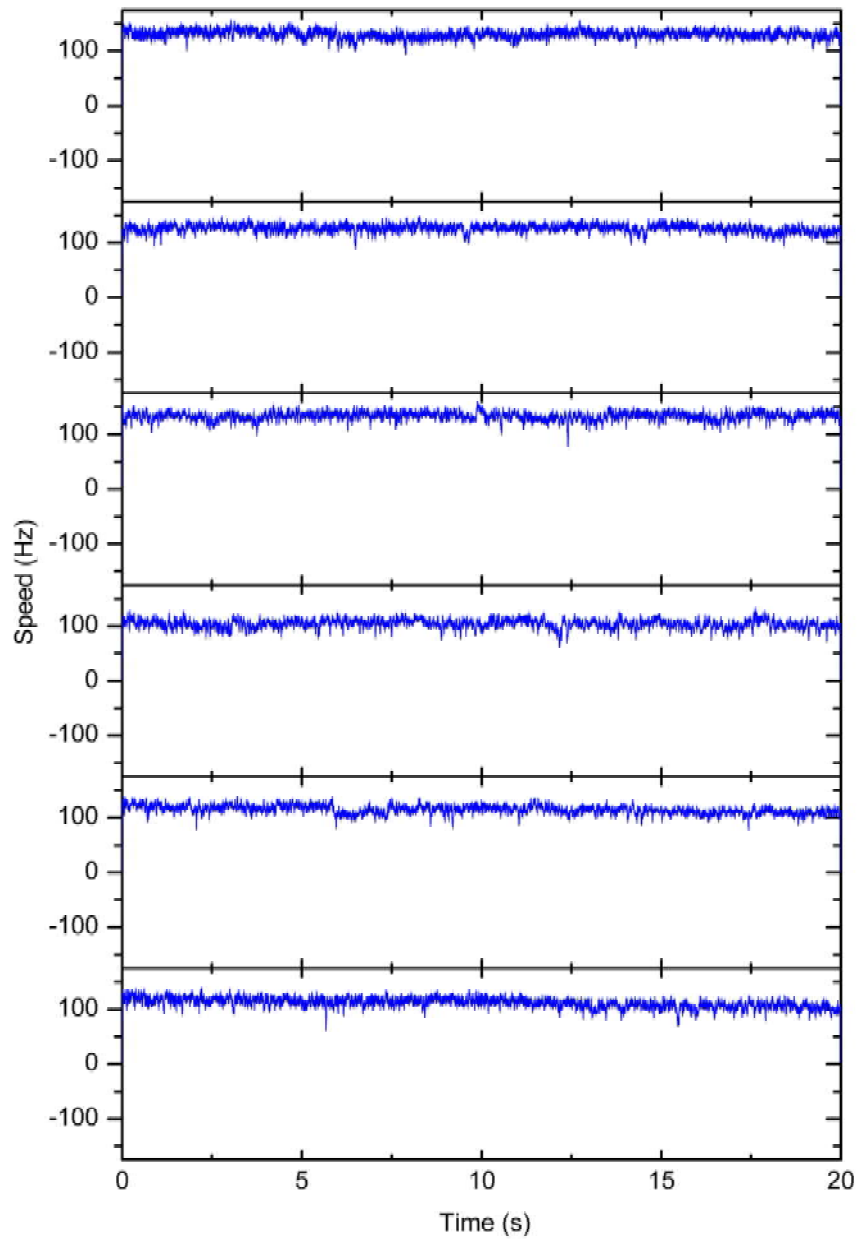
Figure 4.11. 20 s speed records from six different cells of an *E. coli* non-switching strain (KAF95 (*ΔcheY, fliC726*), pFD313 (pFD313 (*fliC^st^*, Ap^R^)). Incomplete switches are absent indicating that the bead assay is not susceptible to mechanical hindrances and that incomplete switching is dependent on motor switching.
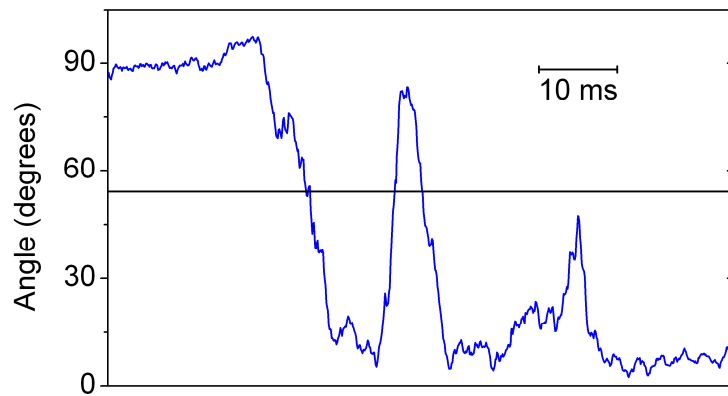
Figure 4.12. Non-instantaneous complete and incomplete switching observed using an optical trap to stall bead-pairs attached to the motor. Bead-pair angle is shown in blue, trap angle in black. CCW motor operation corresponds to about 90° and CW operation to about 10°. Angles were sampled at 10 kHz and are shown without filtering.

these motors at stall torque might not be comparable to the earlier data collected from motors at middle load.

4.2 Motor intervals

Intervals between complete switches were measured according to the criteria and algorithms described in Chapter 3. Importantly, the analysis is not affected by incomplete switching. Figure 4.13, left, shows interval distributions across the full bias range. Intervals are exponentially distributed in the measured range (~ 10 s) with bias dependent mean interval lengths. The superior resolution provided by BFP interferometry over tethered cell assays allows an assessment of intervals down to 10 ms after median filtering. Intervals were analysed for the bias bins with the largest amount of data and are exponentially distributed (Figure 4.13, right), with no sign of a double exponential as reported previously (Kuo and Koshland, 1989). It is possible the double exponential arose due to multiple crossing of the zero-speed threshold applied in that study, an artefact that is observed when the single-threshold scheme is applied to the current dataset (not shown).

Mean CW and CCW interval lengths vary in a reciprocal manner with bias (Figure 4.14, top), with the mean interval lengths robust to at least ± 20% changes in threshold and median filter level (Figure 4.14, centre). The free energy difference between the states varies approximately linearly between 2 k_BT and -2 k_BT over the range of bias that is approximately linear with CheY-P concentration (Figure 4.14, bottom), consistent with the previous relationship observed between free energy difference and CheY-P concentration (Sharf et al., 1998).
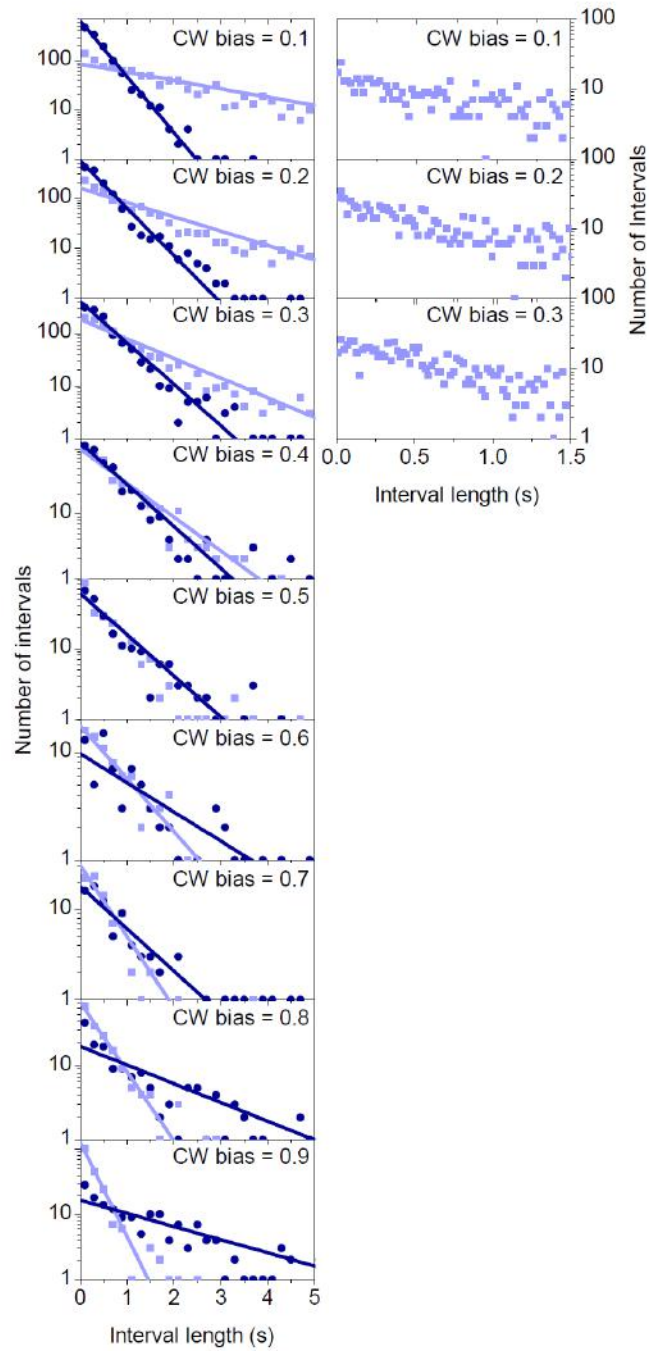
Figure 4.13. Intervals between complete switches. CW data are represented by dark blue circles, CCW data by light blue squares. Left: interval distributions across the full bias range (from top to bottom: 0.1± 0.05, 0.2± 0.05, 0.3 ± 0.05, 0.4 ± 0.05, 0.5 ± 0.05, 0.5 ± 0.05, 0.7 ± 0.05, 0.8 ± 0.05, 0.9 ± 0.05). Lines are exponential maximum likelihood fits applied to the full datasets. Right: data for the first three bias bins (the largest datasets) binned as in the study of Kuo and Koshland, 1989 (20 ms bins from 0 to 1.5 s).
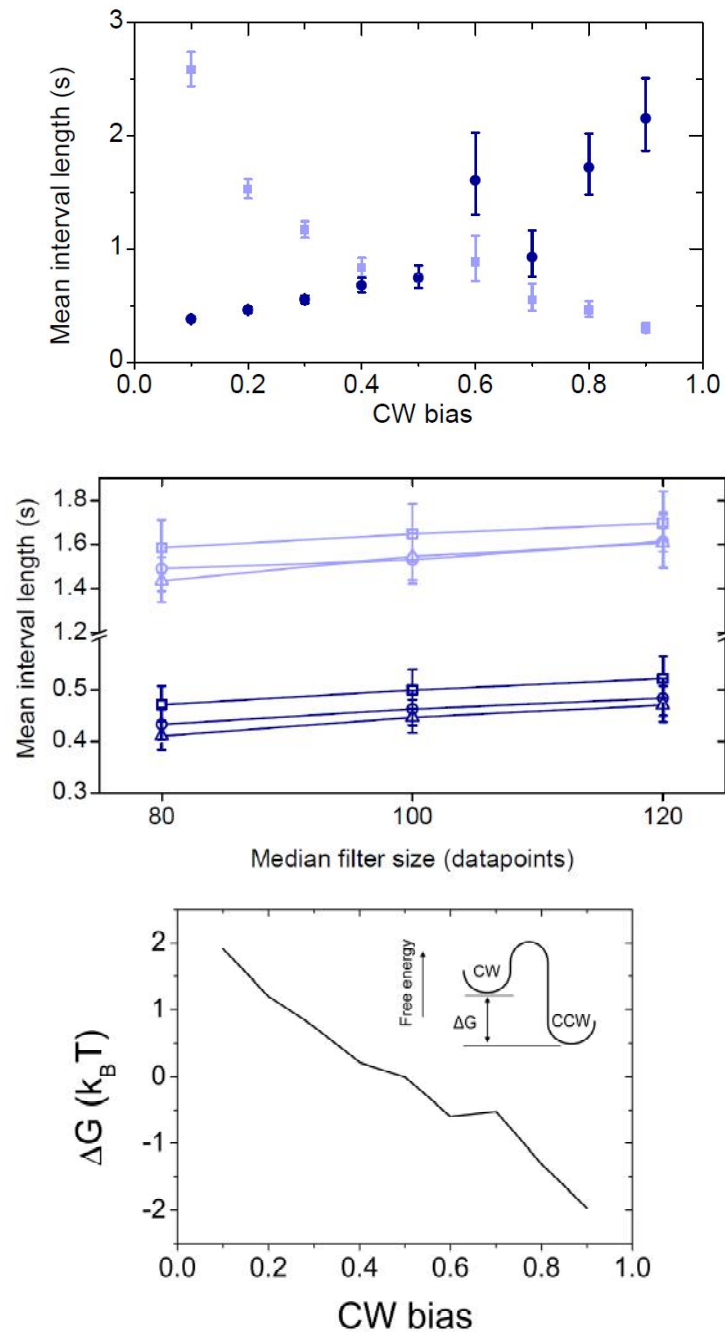
Figure 4.14. Top: mean interval lengths obtained from the fits in Figure 4.13. CW data are represented by dark blue circles, CCW data by light blue squares. Error bars are 99 % confidence intervals. Middle: robustness of interval finding algorithm to 20 % variations in filter and threshold level. Threshold levels are $\alpha = 0.83$ (squares), 0.67 (circles) and 0.59 (triangles) for CCW (light blue) and CW (dark blue) data. Error bars are 95% confidence intervals. Bottom: approximately linear variation with bias of ΔG between CW and CCW states, illustrated in the free energy diagram, inset.

These observations are in conflict with experiments reporting gamma distributed motor intervals (Korobkova *et al.*, 2006). Those experiments were conducted using unsheared flagella, as described in a previous study by the same group (Cluzel *et al.*, 2001) where bead attachment is evidently far from the motor, and the intact flagellum on its own contributes a viscous drag equivalent to a 0.5 μm bead attached to a flagellar stub. Consequently, the relaxation time of this system will be much larger than in the experiments conducted here. It is possible that gamma distributions arise through the loss of short intervals caused by the relatively low time resolution, or that the relaxation dynamics of the filament undergoing polymorphic transitions during the switch (Van Albada *et al.*, 2009) result in a characteristic interval length. Alternatively, the switching kinetics may have been different because of the permanently active CheY mutant used.

4.3 Conclusion

Bacterial flagellar switching has classically been understood in binary terms. This study has identified the multi-state nature of the switch. Switch events are not instantaneous, but show a broadly distributed duration, and incomplete switches are prevalent. Exponentially distributed intervals between complete switches demonstrate that switching approximates a two-state Poisson Process at lower time resolution, despite the underlying multi-state nature of the switch, in agreement with early phenomenological models. These data rule out the MWC model and provide qualitative support for the conformational spread model of allosteric cooperativity. The next chapter undertakes a quantitative comparison between the experimental data and theory.

Chapter 5

Model Agreement

5.1 Model

5.1.1 Conformational spread

Following previous application of the conformational spread model to the bacterial flagellar switch (Duke *et al.*, 2001), we consider the switch complex to be a ring of 34 identical protomers, each consisting of ~1 FliG, 1 FliM and a tetramer of FliN subunits. Each protomer possesses a single binding site, to which a CheY-P molecule can be bound (**B**) or not bound (**b**). Each protomer can independently exist in each of two conformations, active (**A**, corresponding to CW rotation) or inactive (**a,** corresponding to CCW). It is assumed that CheY-P binds the active state more strongly.

The reduced model of conformational spread described in Chapter 2 was applied. The magnitude of the free energy difference between activity states is E_A, independent of CheY-P binding. A free energy diagram of the four states of a single protomer and the transitions between them is shown in Figure 5.1, left, for the case of CW bias = 0.5. Without CheY-P bound the inactive (CCW) state is energetically favoured, and with CheY-P bound the active (CW) state is favoured, consistent with the known relationship between bias and CheY-P concentration (Cluzel *et al.*, 2000).
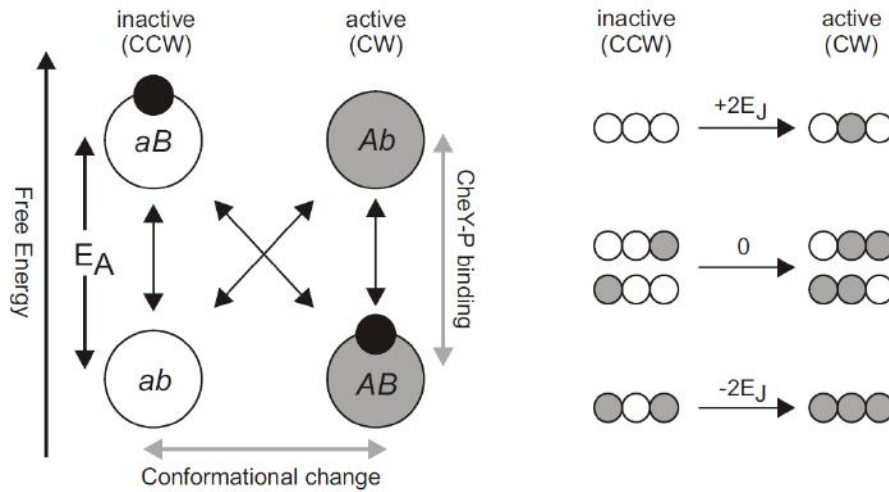
Figure 5.1. Conformational spread model of the bacterial flagellar switch. Left: the free energy diagram of the four states of a protomer and the transitions between them for the case of CW bias = 0.5, excluding free energy due to the conformation of neighboring protomers. CheY-P is shown as a black circle. Right: Interactions add 0, $+2E_J$ or $-2E_J$ to the free energy of a conformational change, depending on the state of adjacent protomers.

Figure 5.2. A generalized version of the free energy scheme shown in Figure 1, left. The free energy of conformational change is $\pm E_A$. The free energy of CheY-P binding is dependent on the CheY-P concentration as shown, with $E_C = - log_e(c/c_{0.5})$. If $E_C > 0$, the inactive state becomes more highly populated and hence CW bias < 0.5, while $E_C < 0$ similarly implies CW bias > 0.5.

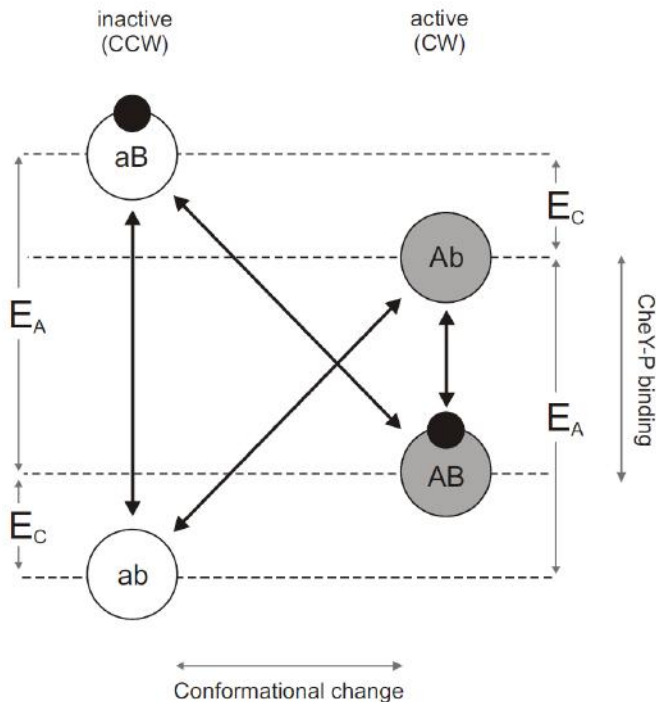In the ring, interactions between adjacent protomers favour pairs with the same conformation, such that the free energy of interaction is lower by E_J for any like pair compared to any unlike pair, independent of CheY-P binding. These interactions add 0, $+2E_J$ or $-2E_J$ to the free energy of a conformational change, depending on the state of adjacent protomers (Figure 5.1, right).

Rate constants for conformational change that satisfy detailed balance are expressed as:

$$k_{a \to A} = \omega_a \exp\left(\frac{\lambda_a}{k_b T} \Delta G(a \to A) \right)$$

$$k_{A \to a} = \omega_a \exp\left(\frac{\lambda_a - 1}{k_b T} \Delta G(a \to A) \right)$$

$\Delta G(a \to A)$ is the sum of the free energy changes associated with changes in activity and interaction, holding one of six values: $\pm E_A$, $\pm(E_A + 2E_J)$ or $\pm(E_A - 2E_J)$. The fundamental flipping frequency, ω_a, was set as 10^4 s^{-1}, a typical rate of protein conformational change and consistent with previous modelling of the switch complex (Duke *et al.*, 2001, Hille, 1992). Lacking information about λ_a, the parameter that specifies the degree to which changes in the free energy affect forwards as opposed to backward rate constants, an intermediate value of $\lambda_a = 0.5$ was selected.

As specified in the general model (Chapter 2), the free energy associated with CheY-P binding depends only on the conformation of the protomer bound, and not on adjacent protomers. Binding rates are expressed as:

$$k_{b \to B} = \frac{c}{c_{0.5}} \omega_b \exp\left(\frac{\lambda_b}{kT} \Delta G^*(b \to B) \right)$$

$$k_{B \to b} = \omega_b \exp\left(\frac{\lambda_b - 1}{kT} \Delta G^*(b \to B) \right)$$

where c is the concentration of CheY-P, $c_{0.5}$ is the concentration of CheY-P required for neutral bias, ω_b is the characteristic binding rate and $\Delta G^*(b \to B)$ is the free energy associated with binding when CheY-P is at the concentration $c_{0.5}$ ($= \pm E_A$). By consideration of detailed balance, the free energy of CheY-P binding is then:

$$\Delta G(b \to B) = \Delta G^*(b \to B) - \log_e\left(\frac{c}{c_{0.5}} \right) = -\log_e\left(\frac{c}{c_{0.5}} \right) \pm E_A$$

The protomer free energy diagram is redrawn for the case $c \neq c_{0.5}$ in Figure 5.2. A value of $\omega_b = 10$ s^{-1} was selected based on the experimentally determined CheY-P binding rate (Sourjik and Berg, 2002b), and consistent with previous modeling of the switch complex (Duke *et al.*, 2000), and $\lambda_b = 0$ such that the binding rate is independent of protomer conformation.

5.1.2 Simulation

Monte Carlo simulations of the conformational spread model described above were coded in C++ by Dr. B. Steel (postdoctoral researcher in the Berry Group, Department of Physics, University of Oxford) and provided for use. The simulation is described in this section. Each protomer is initially set to inactive and without CheY-P bound (interval analysis as described in Chapter 3 begins only from the first switch, so any initial perturbation of behaviour due to initial conditions will not affect the final analysis).

Following on from initial conditions, each protomer n of the ring is assigned two transition times, A_n and B_n, at which it will undergo a state change associated with (A) activation or inactivation and (B) binding or release of CheY-P. For a rate constant k the time for each forthcoming transition was calculated as $t-t_0 = -log_e(rand)/k$, where t_0 is the simulation time at which the calculation is made and *rand* is a random number (8 byte double) generated in the interval 0 to 1 according to the Mersenne-twister algorithm (Matsumoto and Nishimura, 1998). The simulation iteratively progresses to the earliest time present in the arrays A and B, and modifies the state of the corresponding protomer accordingly. New transition times A_n and B_n are then calculated for that protomer, and, if the transition was associated with a change in activity of that protomer, then transition times A_{n+1} and A_{n-1} for the two neighbouring protomers are also recalculated. The number of active protomers and bound CheY-P were recorded at times $m\Delta t$, for integer m up to 300,000 and $\Delta t = 0.1$ms, and passed to a Langevin simulation

5.1.3 Langevin dynamics

To allow direct comparison between the output of the conformational spread model and experimental data, a linear dependence of motor speed on the number of active protomers in the ring was assumed. This assumption is based on the motor containing a large number of independent units (Reid *et al.*, 2006) each of which generates constant torque in a direction specified by the state of the nearest rotor protomer (the assumption is expected to breakdown at low numbers of stator units, as discussed in Chapter 6). A Langevin simulation, which considers Brownian motion in a potential, was adapted from Xing *et al.*, 2006, and modelled the viscous load of the bead connected to the motor by a

flexible tether, thereby converting simulated activity on the ring into rotation angle of the bead. Rotor position is updated at each simulation step of length Δt following:

$$\theta_{rotor}(t + \Delta t) = \theta_{rotor}(t) + V_{rotor}(t)\Delta t\ ;$$

motor speed is proportional to ring activity and is given by $V_{rotor} = V_0\,(N_{CCW}(t) - 17)\,/\,17$ where V_0 is the maximum speed and $N_{CCW}(t)$ is the number of inactive subunits outputted by the Monte-Carlo simulation. Bead position is updated by introducing a Wiener process:

$$\theta_{bead}(t + \Delta t) \approx \theta_{bead}(t) + \frac{\Gamma}{\zeta_{bead}}\Delta t + Z\frac{1}{\kappa}\left(1 - e^{-2\frac{\kappa.k_B T}{\zeta_{bead}}\Delta t}\right)\ ;$$

here Z is a normal random variable with zero mean and unit variance, ζ_{bead} is the drag coefficient of the bead, Γ is the torque delivered through the flexible linkage in the hook/flagellum that can be modeled by assuming an ideal elastic spring:

$$\Gamma = \kappa(\theta_{rotor} - \theta_{bead})\ ;$$

κ is the experimentally determined stiffness of the hook/flagellum (Block *et al.*, 1991). The Langevin simulation described above was coded in C++ by Dr. B. Steel and provided for use.

5.1.4 Choice of energy parameters

Simulation θ_{bead} records were split into 30s records and analyzed identically to experimental records as described in Chapter 3. The resulting simulation speed records

were binned by CW bias rather than the underlying value of $c/c_{0.5}$. The simulated CheY-P concentration was varied to obtain the desired CW bias.

Energy parameter maps were constructed in an attempt to find suitable values of E_A and E_J for comparison to experiment. The mean complete switch duration, mean complete switch interval and mean incomplete switch interval were measured from simulated data (binned at 0.5 CW bias) as a function of E_A and E_J across the ranges $0.2 < E_A < 1.0$ and $3.7 < E_J < 4.5$ (Figure 5.3).

The relationships observed between the energy values and switching behaviour are consistent with our understanding of the conformational spread model. Events proceed via the nucleation of a new domain, at an energy cost of $2E_J \pm E_A$, and the domain spreads around the ring, with the free energy change for each protomer undergoing a conformational change equal to $\pm E_A$. Upon completion of the spread to encompass the entire ring, the energy of the system reduces by $2E_J \pm E_A$. Complete and incomplete switching depend on nucleation and spread, and are thus a function of both E_A and E_J, while the duration of a complete switch depends only on spread, and thus is only a function of E_A.

The maps do not appear to identify a single pair of energy values for E_A and E_J that are able to accurately reproduce all three of the experimental means. This was confirmed by conducting a parameter space search for solutions, the results of which are shown in Figure 5.4. The curves identify E_A and E_J values that provide separate agreement for switch duration, complete switch interval, or incomplete switch interval means. The three curves do not have a common intersection, and demonstrate that the conformational
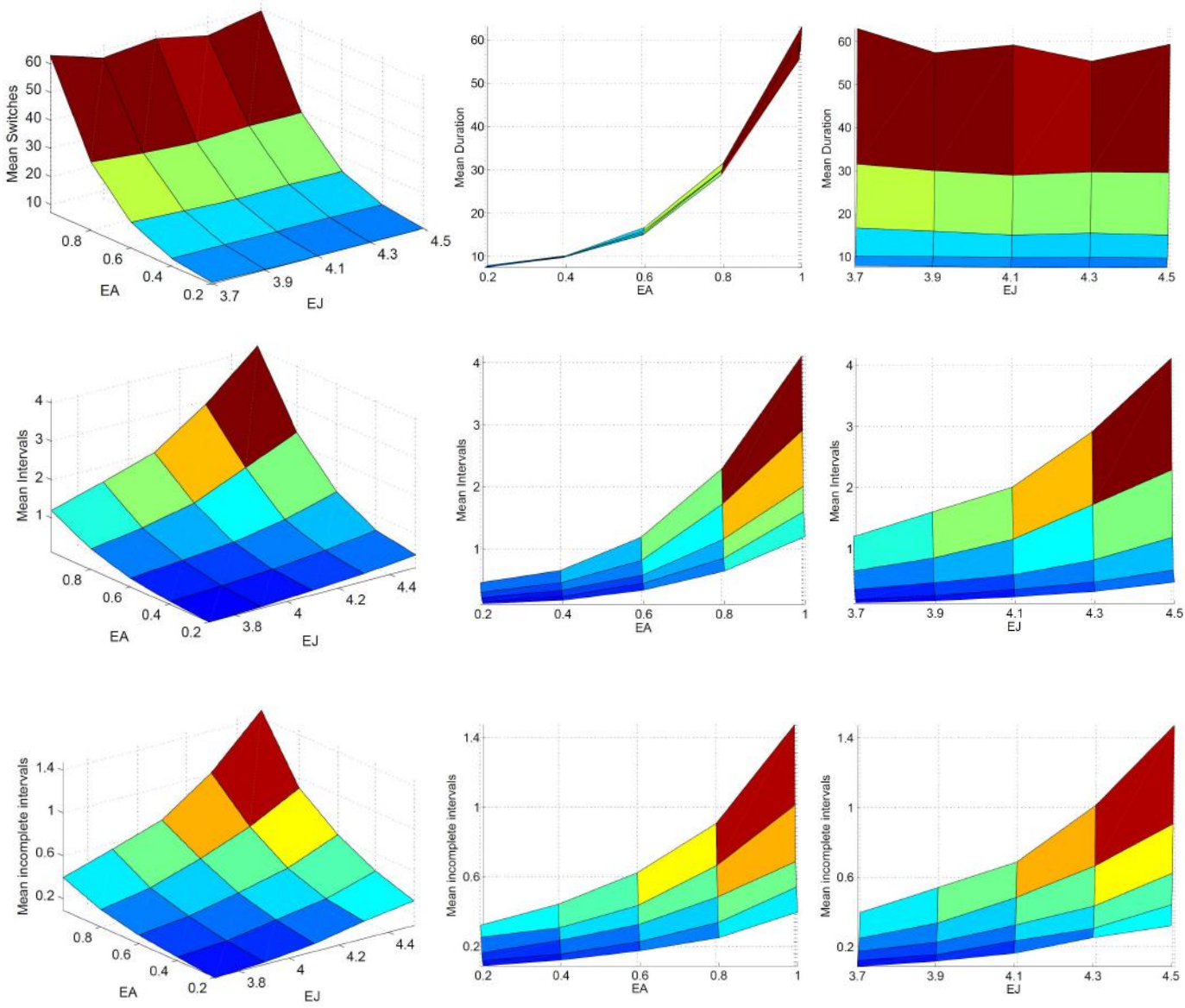
Figure 5.3. Energy landscapes for mean complete switch duration (top, with the map rotated to identify E_A and E_J dependencies to the right), mean complete switch interval length (middle) and mean incomplete switch interval length (bottom).
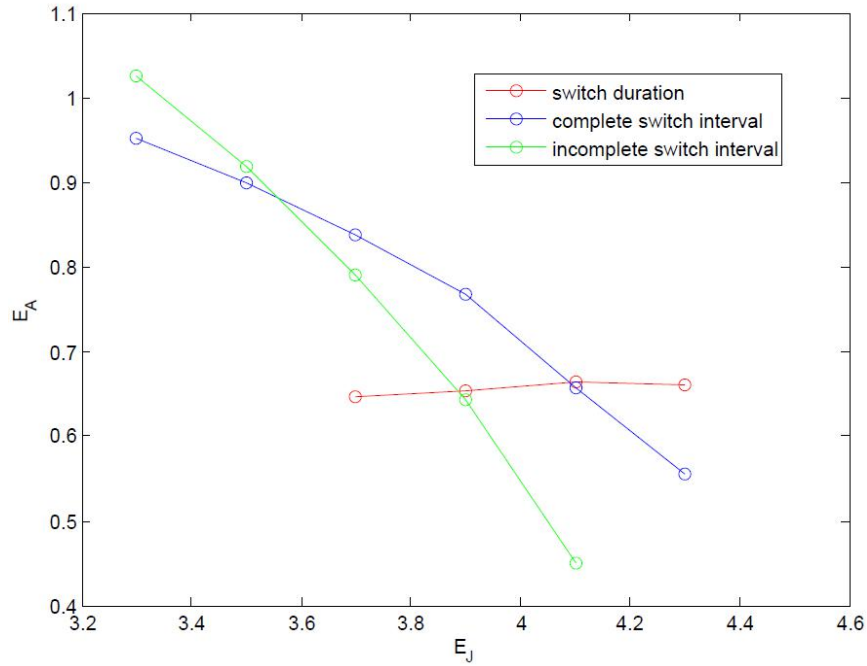
Figure 5.4. Solutions for agreement between experiment and simulation. For each E_J value considered, an E_A value was determined by using MATLAB's fminsearch function to locate a stable minimum of the cost function $(S-E)^2/E^2$, where S and E denote simulation and experimental mean values respectively for either mean switch duration (18.72 ms, obtained from all 3579 switches analyzed), mean complete switch interval or mean incomplete switch interval (0.75 s or 0.25 s respectively, obtained from the 448 intervals from the records where the CW bias was between 0.45 and 0.55). S_q were obtained from identical analysis of 50 separate 30 s simulations with the parameter $c/c_{0.5}$ set to 1 to give an average bias of 0.5. Starting values for E_A were either 1 k_BT or 0.6 k_BT, chosen to provide stable solutions.

spread model (with the fixed selected values for ω_a, ω_b, λ_a, λ_b) is only able to provide close agreement for any two of the experimentally determined means.

We choose to optimise agreement for complete switching (mean duration and mean interval at 0.5 CW bias). A 2-D parameter space search was conducted for suitable E_A and E_J values in the vicinity of the unique solution identified in Figure 5.4. MATLAB's fminsearch function was used to locate the stable minimum of the cost function $\Sigma_q(S_q\text{-}E_q)^2/E_q{}^2$, where S and E denote simulation and experimental mean values respectively for the mean switch duration ($q=1$) and mean complete switch interval ($q=2$). E_1 =18.72 ms, obtained from all 3579 switches analyzed, while E_2 = 0.75 s, obtained from the 448 intervals from the records where the CW bias was between 0.45 and 0.55. S_q were obtained from identical analysis of 50 separate 30 s simulations with the parameter $c/c_{0.5}$ set to 1 to give an average bias of 0.5. Starting values of $E_J = 4\ k_BT$ and $E_A = 1\ k_BT$ were used. Final values were $E_J = 4.13\ k_BT$ and $E_A = 0.66\ k_BT$.

These fitted energy values are sensitive to the fixed parameters ω_a, ω_b, λ_a, λ_b. Consequently, they are unlikely to represent precisely the true free energy values associated with conformational changes and coupling in the bacterial flagellar switch. However, it is worth noting that the fitted value of E_A appears to be consistent with previous experimental findings. The rates of switching in the absence of CheY at low temperature provided the free energy difference between CW and CCW ring conformations as a function of temperature up to about 10 °C. An extrapolation of the data provided an estimate of the free energy difference between ring conformations at room temperature (about 15 k_BT). Meanwhile, the theoretical free energy difference

between ring conformations in the absence of CheY-P is $34E_A$, approximately 20 k_BT with the fitted E_A here.

5.2 Agreement

5.2.1 Multi-state behaviour

The constrained simulated speed records (Figure 5.5 and Figure 5.6) are qualitatively indistinguishable from the experimental records, exhibiting complete and incomplete switching between CW and CCW states. The simulated records were analysed using algorithms identical to those applied to experimental records, as described in Chapter 3 (Figure 5.7).

The similarity between the simulated and experimental multi-state behaviour is clearly evident (Figure 5.8). The fastest switches are observed to be completed in less than 2 ms, undergoing an abrupt change in rotation direction. Typically, switches last of order 10 ms, with a smooth deceleration, reversal and acceleration phase. Slower switches are observed lasting tens of millseconds, and are more likely to exhibit non-monotonic speed variation, a signature observed in slower experimental switches. The slowest switches last over 100 ms. Interestingly, these often display the behaviour observed in very slow experimental switches, where motor rotation plateaus for a sustained period at an intermediate speed (typically close to zero) before completion.

Complete switch durations are distributed equally to the experimental data (Figure 5.9). The agreement is notable for the fact that only the mean switch duration was used to constrain the simulations. Simulations reproduce the peaked distribution, and subsets of

Figure 5.5. Full 30 s record of a typical unfiltered simulation of the conformational spread model, showing the number of active protomers in the ring (blue) and the number of CheY-P molecules bound (green). The trace is split into 5 s sections top to bottom.

Figure 5.6. The corresponding simulated speed record computed from the subunit record of Figure 5.5, for direct comparison to experimental data (median filtered (100 points) and including the effect of the bead linkage). The trace is split into 5 s sections top to bottom.

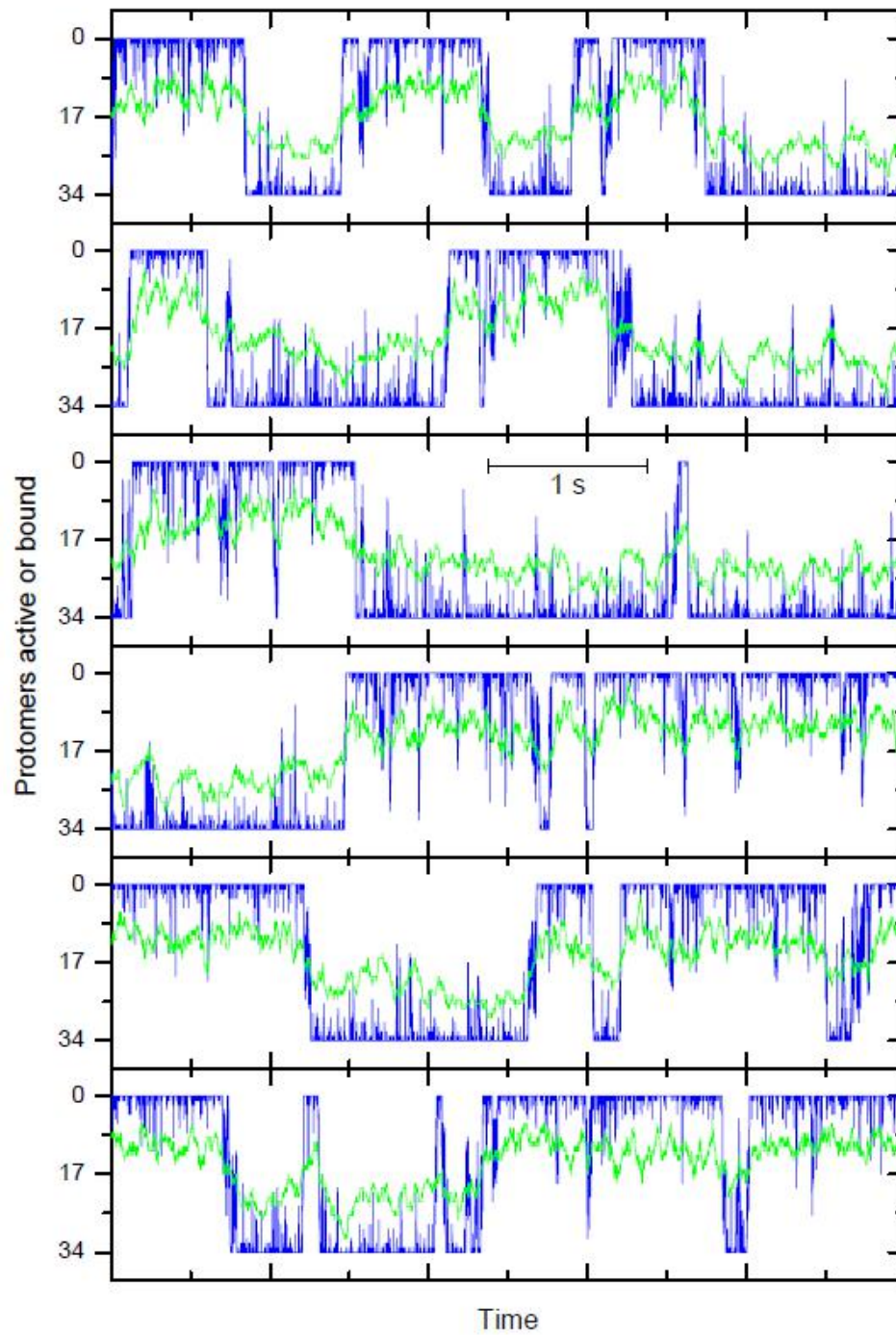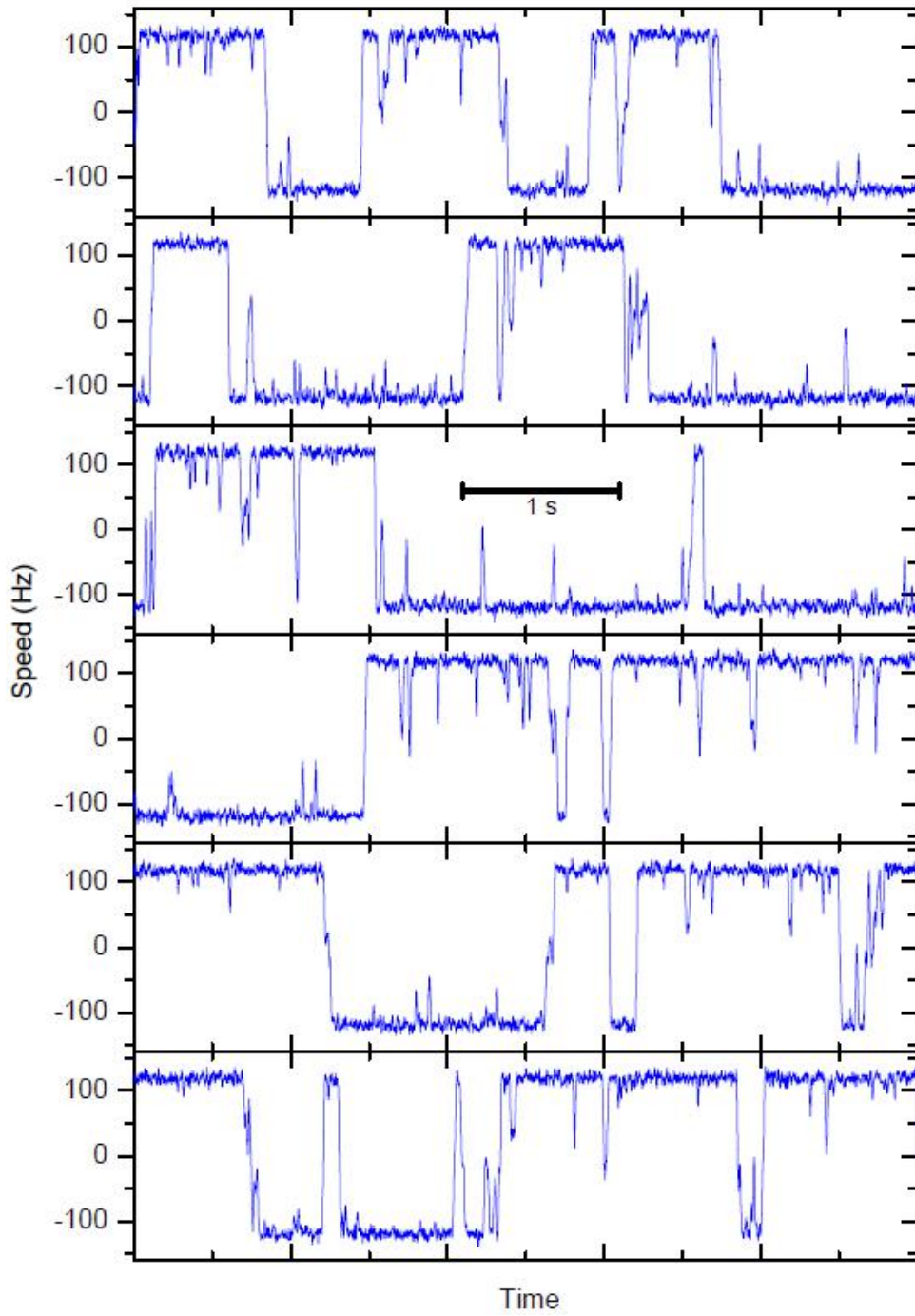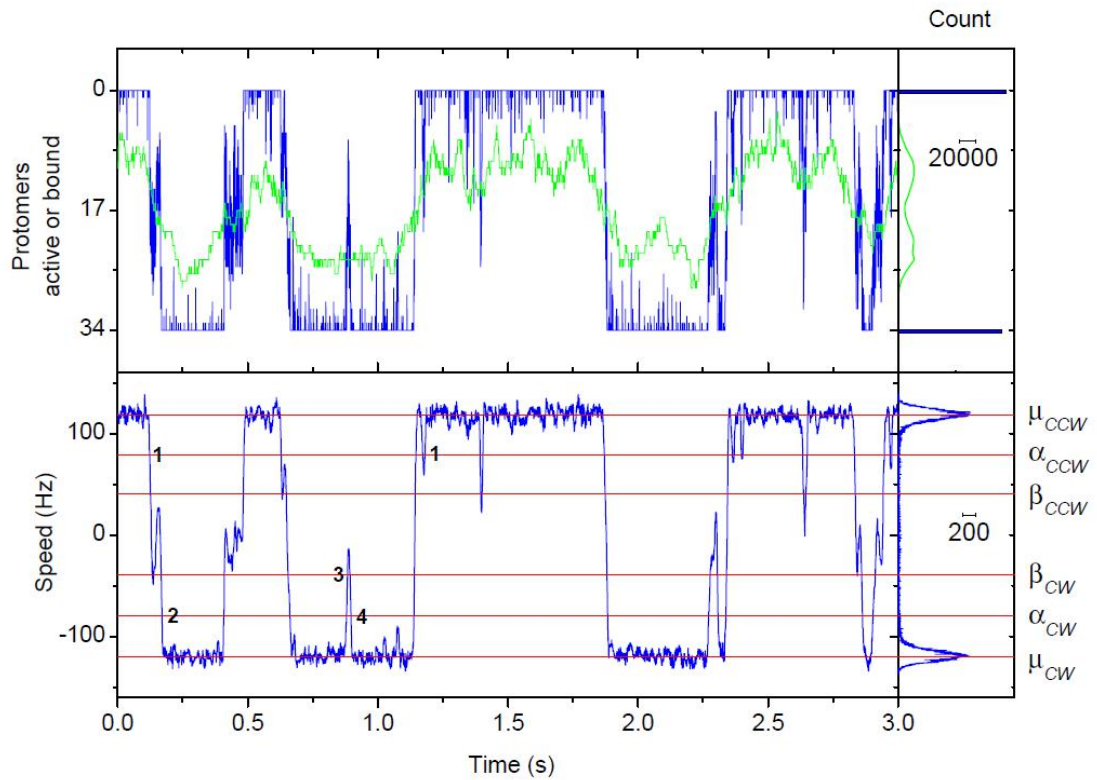Figure 5.7. Analysing simulated records. Top: three seconds of a typical unfiltered simulation record of the conformational spread model, showing the number of active protomers in the ring (blue) and the number of CheY-P molecules bound (green). To the right is shown activity and binding histograms for the full 30 s record. Bottom: the corresponding simulated speed record for direct comparison to experimental data, median filtered (100 points) and including the effect of the bead linkage. The motor speed histogram for the full 30 s record is used to set the α and β thresholds. Indicated are the passages of the thresholds that define switching behaviour. 1 alone: not scored. 1→2: complete switch (CCW→CW). 3→4: incomplete switch from the CW state. Switching from the opposite state is defined similarly.
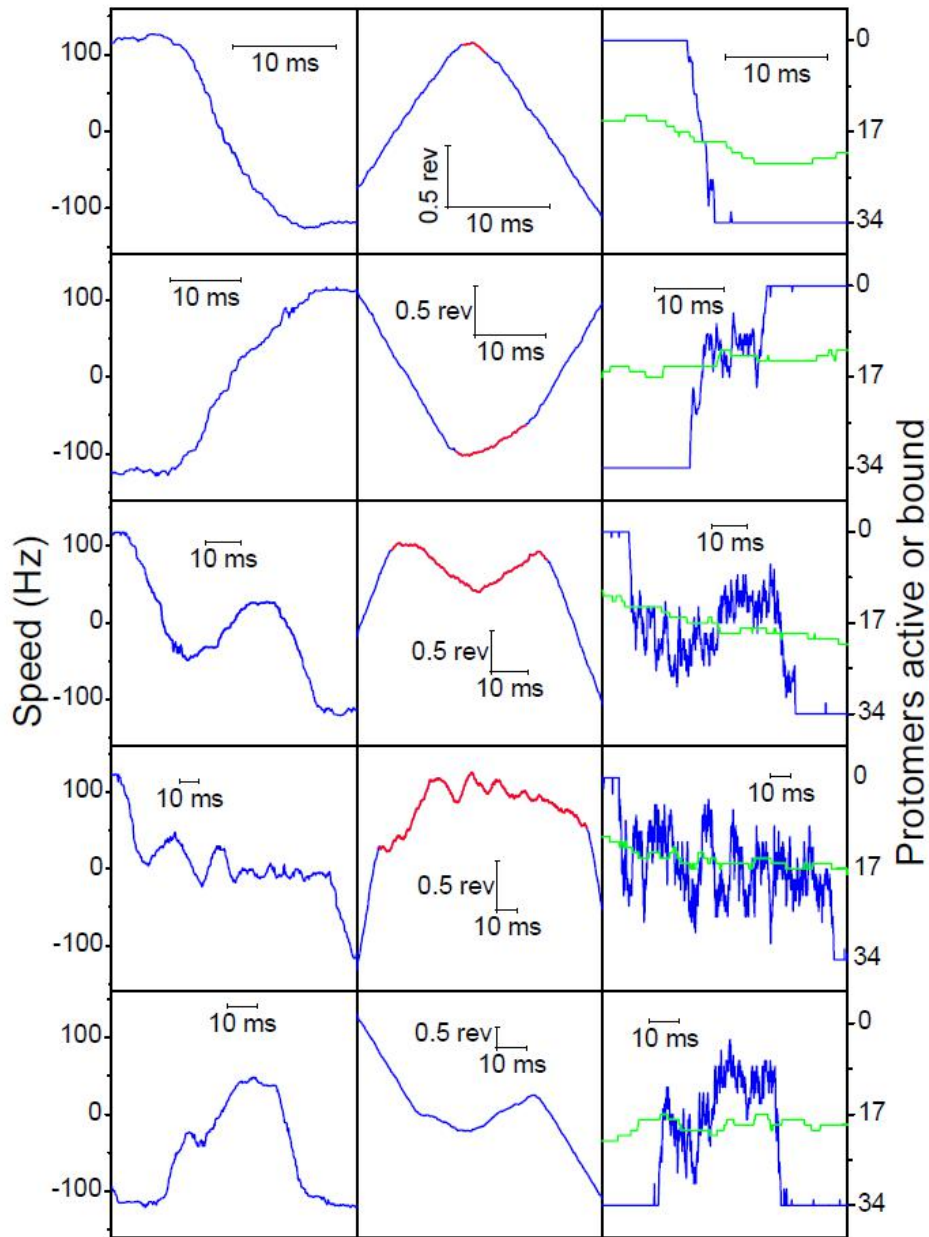
Figure 5.8. Multi-state behaviour in simulation records. Left panels: 100 point median filtered speed trace. Centre panels: unfiltered bead angle trace. The duration of the switch, marked in red, was calculated as the interval during which the bead angle trace was statistically different from the CW and CCW motor states, as with the experimental data. Right panels: the number of active protomers (blue) and bound CheY-P molecules (green) in the simulation. Switch durations (from top): 2 ms, 9.9 ms, 42.9 ms, 105.6 ms. The bottom dataset displays an incomplete switch leading to transient reversal of rotation.
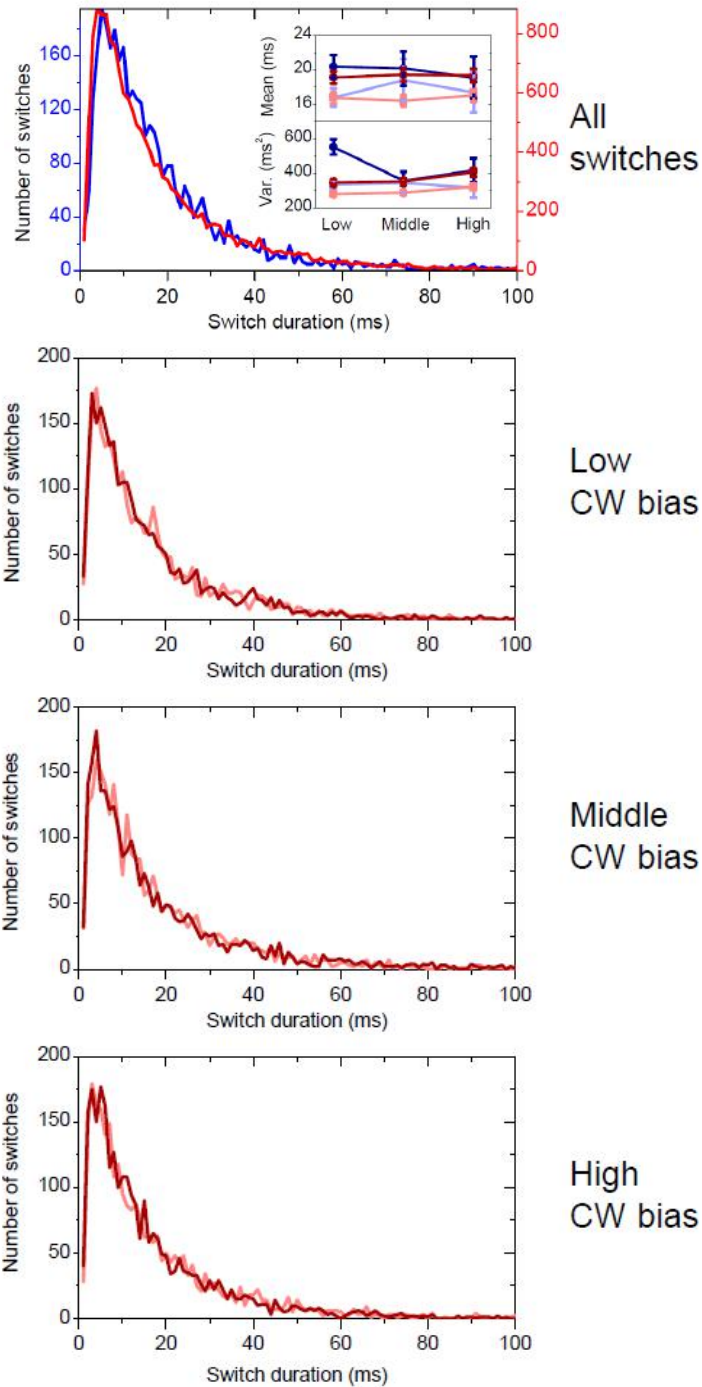
Figure 5.9. Top: Comparison of simulated experimental switch duration distributions. Experimental data are in blue, simulation data are in red. Inset: mean and variance of switch durations for CW-to-CCW (light coloured datapoints) and CCW-to-CW (dark coloured datapoints) switches for different ranges of CW bias (low = 0 – 1/3, middle = 1/3 – 2/3, high = 2/3 – 1). Error bars are 99% confidence intervals. The associated distributions are shown in the bottom three panels.

the data sorted according to bias and switch direction do not display clear trends, as observed in experiment. A consideration of conformational spread kinetics might have suggested that switches from the favourable to the unfavourable state would take longer to complete. It may be that in this scenario, only the fastest switches can survive to encompass the ring for completion, opposing the expected trend.

Incomplete switches were not fitted in the constrained model but nonetheless display qualitatively similar behaviour to experiment (Figure 5.8), with events undergoing non-monotonic speed variation and occasionally being responsible for reversals. The events occur as a Poisson process with bias-dependent rate constants, showing broad quantitative agreement with experiment (Figure 5.10). As in the experimental data, the exponential distributions are conserved across β, and mean intervals exhibit the same linear relationship with β (Figure 5.11). In the context of conformational spread, β is related to the extent of the spread during the incomplete switch, further indicating that the dynamics of the switch out of equilibrium are similar in experiment and simulation.

The frequency of incomplete switching is higher in experiment than in simulation. Agreement may improve upon a more thorough search of the model parameter space, to include an examination of the parameters ω_a, ω_b, λ_a and λ_b. Closer agreement might also be achieved by introducing torque-generating units into the simulation: the current simulation treats the switch as a 34-state system; reducing this to a ~ 10 state system (Reid *et al.*, 2006) will lead to further discretisation of speed. Activating ~ 1 in ~ 10 units will lead to a larger fluctuation in speed than activating ~ 1 in 34 protomers, increasing the number of incomplete switches detected. It is also possible that the higher frequency
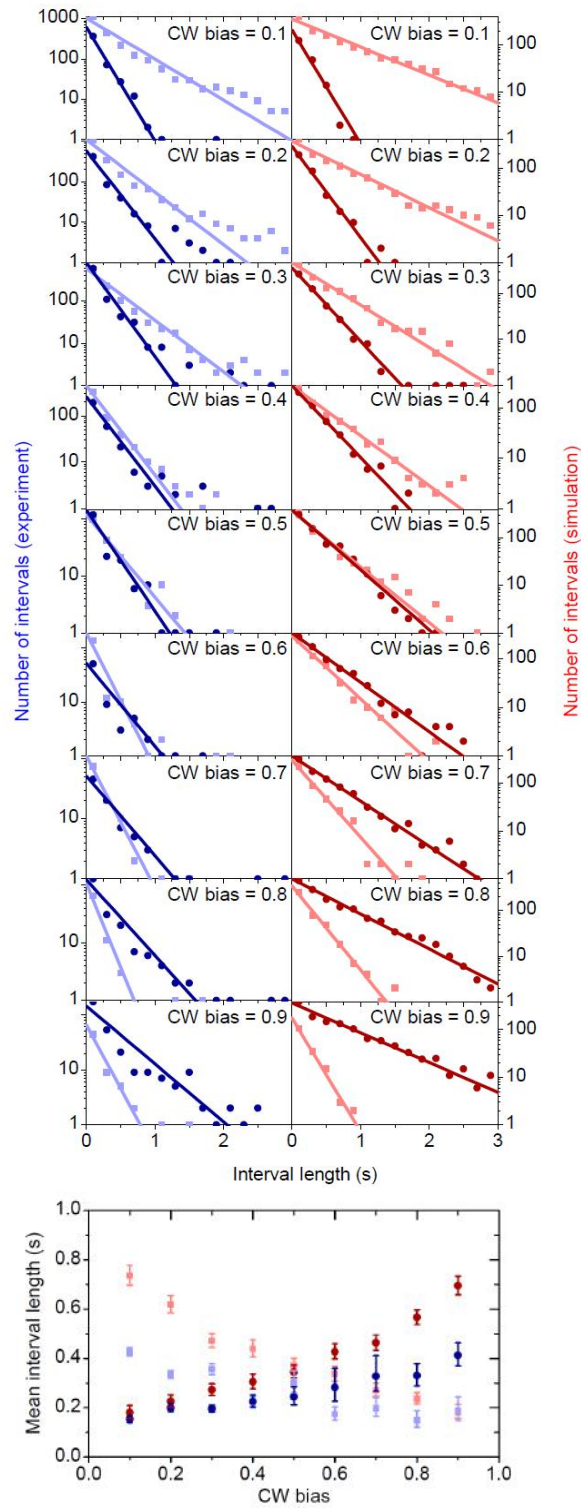
Figure 5.10. Intervals between incomplete switches. Experimental data are in blue, simulated data in red. CW data are represented by dark blue circles, CCW data by light blue squares. Top: distributions of intervals at a range of CW biases ((from top to bottom: 0.1± 0.05, 0.2± 0.05, 0.3 ± 0.05, 0.4 ± 0.05, 0.5 ± 0.05, 0.5 ± 0.05, 0.7 ± 0.05, 0.8 ± 0.05, 0.9 ± 0.05). Lines are exponential maximum likelihood fits applied to the full datasets. Bottom: mean interval lengths obtained from the fits above. Error bars are 99 % confidence intervals.
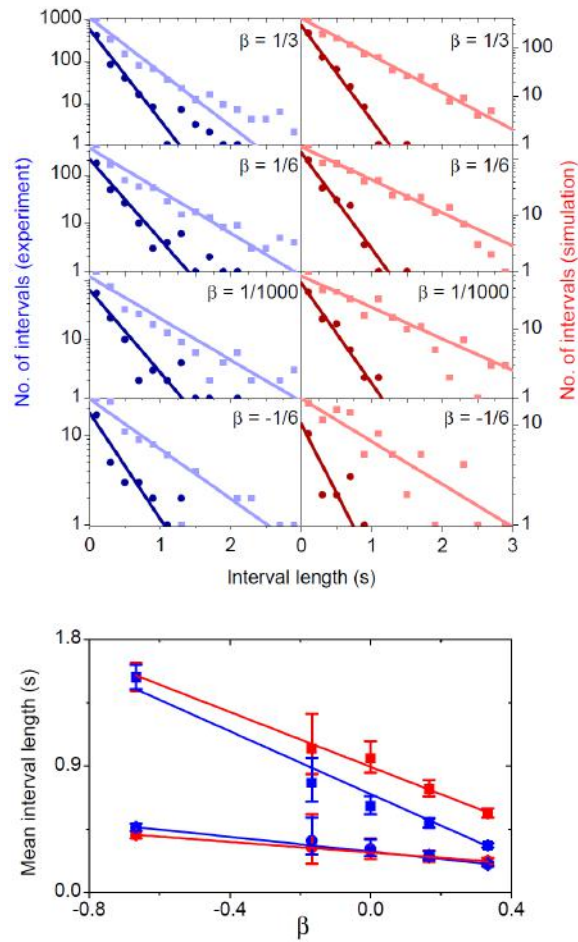
Figure 5.11. Incomplete switch interval dependence on β. Experimental data are in blue, simulated data in red. CW data are represented by dark blue squares, CCW data by light blue circles. Top: distributions of intervals between incomplete switches for the CW bias bin with the largest dataset (0.2 ± 0.05), with varying β (from top to bottom, $\beta = 1/3$, $1/6$, $1/1000$, $-1/6$). Lines are exponential maximum likelihood fits to the full datasets. Right: linear variation of mean interval lengths with β obtained from the fits on the left. Also plotted are the mean complete switch interval lengths (see section 5.2.2), equivalent to an analysis with $\beta = -2/3$. Error bars are 99 % confidence intervals.

of incomplete switching in experiments is an artefact of noise, despite the measures described in Chapter 3 to reduce such effects.

5.2.2 Motor intervals

The intervals between complete switches are distributed exponentially with bias-dependent mean interval lengths in very close agreement with the experimental data (Figure 5.12), despite only having constrained the simulations with the mean interval length at 0.5 CW bias. Evidently, the simulated flagellar switch can also be regarded as a two state Markov system at lower time resolutions. Figure 5.13 displays the full datasets. The insets show the data plotted on a log-log scale; the absence of linearity here demonstrates that unlike at long timescales (Korobkova *et al.*, 2004) the experimental data do not follow a power law distribution on short timescales.

The agreement between experimental and simulated intervals provides the basis for an assessment of missed events. It is possible that very short intervals were missed due to experimental noise and filtering, which would affect the complete switch interval distributions. Missed events would also have consequences for incomplete switching, whereby filtered pairs of complete switches separated by a short time interval are misclassified as an incomplete switch. The concern was addressed by analyzing the simulation protomer records, which are free from noise and filtering, with an analogous interval measurement algorithm to that described in Chapter 3, but with thresholds set to detect transitions between 0 and 34 active subunits. These data are found to be exponentially distributed with rate constants in very good agreement with the simulation distributions (Figure 5.14). This approach is equivalent to simulation techniques used for
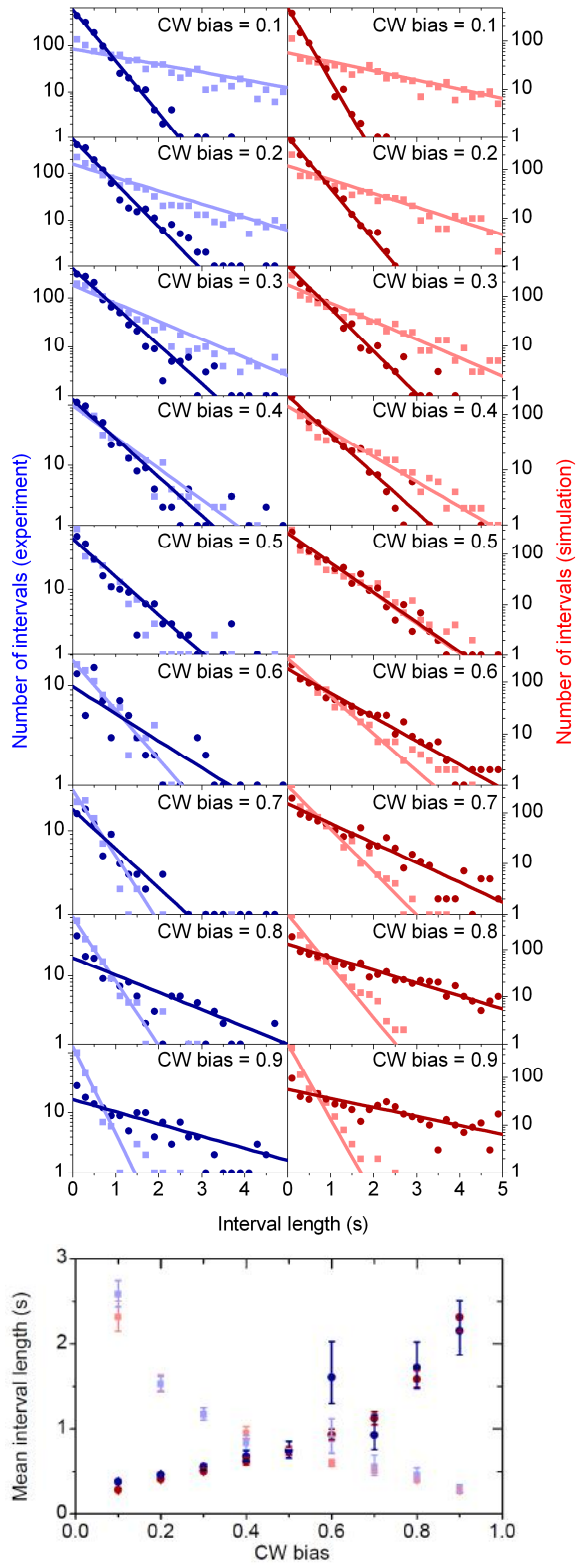
Figure 5.12. Distributions of intervals between complete switches at a range of CW bias values (0.1 ± 0.05, 0.2 ± 0.05, 0.3 ± 0.05, 0.4 ± 0.05, 0.5 ± 0.05, 0.6 ± 0.05, 0.7 ± 0.05, 0.8 ± 0.05, 0.9 ± 0.05 top to bottom). Experimental data are in blue, simulated data in red. CW data are represented by dark blue circles, CCW data by light blue squares. Lines are exponential maximum likelihood fits applied to the full datasets. Bottom: mean interval lengths obtained from the fits above. Error bars are 99 % confidence intervals.

105
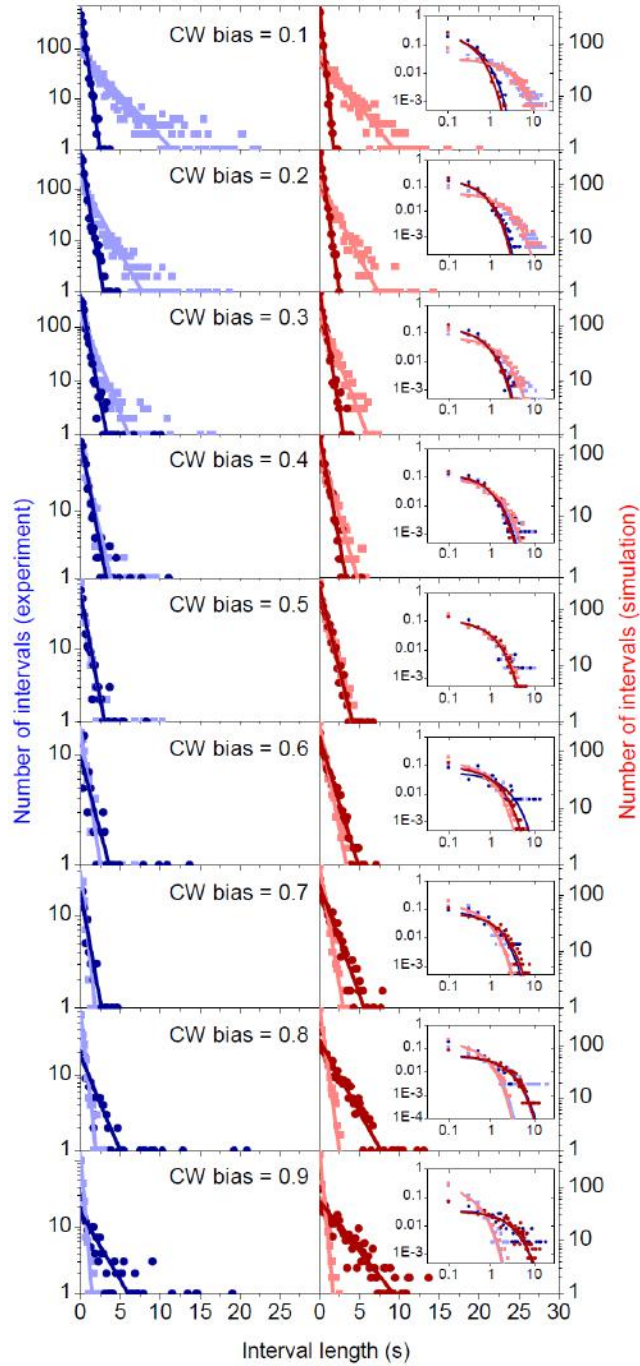
Figure 5.13 Distributions of intervals between complete switches at a range of CW bias values (0.1 ± 0.05, 0.2 ± 0.05, 0.3 ± 0.05, 0.4 ± 0.05, 0.5 ± 0.05, 0.6 ± 0.05, 0.7 ± 0.05, 0.8 ± 0.05, 0.9 ± 0.05 top to bottom). Experimental data are in blue, simulation data are in red. CW data are represented by dark circles, CCW data by light squares. Lines are exponential maximum likelihood fits applied to full datasets. Insets are the same data plotted on log-log scale, demonstrating the lack of a power law distribution in all bias bins.

Figure 5.14. Assessment of missed events. Simulated data are in red, protomer record data are in green. CW data are represented by dark circles and CCW data by light squares. Top: distributions of intervals between complete switches across the full bias range. Lines are exponential maximum likelihood fits. Bottom: mean intervals from the fits above. Error bars are 95 % confidence intervals.

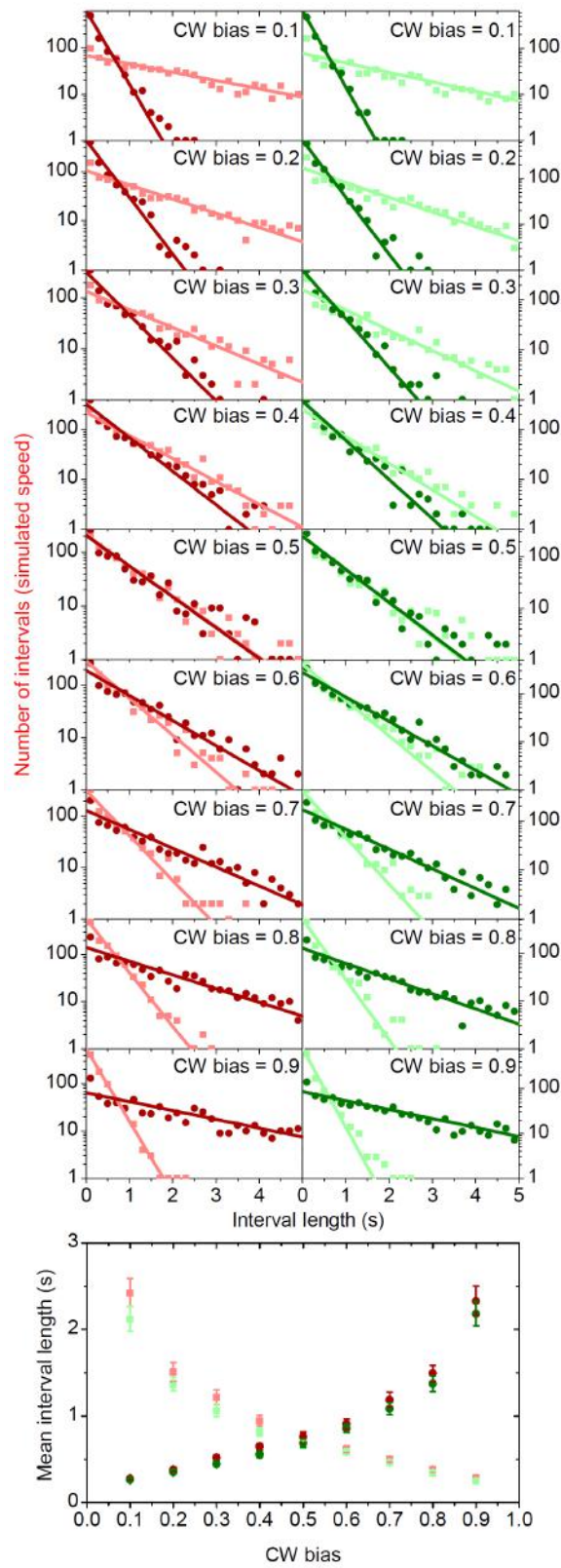determining the significance of missed events in ion channel record analysis (Qin and Li, 2004), and suggests that missed events are unlikely to be an issue in the experimental data.

5.2.3 Cooperativity

A final and important test of the constrained model is whether it reproduces the high cooperativity observed in previous experiments (Cluzel *et al.*, 2001), while maintaining a minimal binding cooperativity (Sourjik and Berg, 2002b). The construction of a Hill plot confirms this to be the case (Figure 5.15), with $h_Y = 3.5$ and $h_R = 9.4$.

The value of the binding cooperativity is slightly higher than experimentally observed, although that number is expected to be an underestimate due to confounding cytoplasmic contributions (Sourjik and Berg, 2002b). Equivalent FRET experiments on single motors may provide closer agreement. Such experiments may be able to resolve the difference in the number of bound CheY-P molecules between CW and CCW states. Figure 5.7, top, shows a subtle shift in the bound fraction around a switch event, associated with the difference in dissociation constants between CW and CCW states in the model. (A lag-correlation analysis of the protomer and binding series did not identify a clear correlation between changes in binding and protomer activity, suggesting that binding sometimes leads and sometimes lags subunit activity). However, the two populations are clearly evident over the course of 30 s (as seen in the histogram of Figure 5.7, top, right).
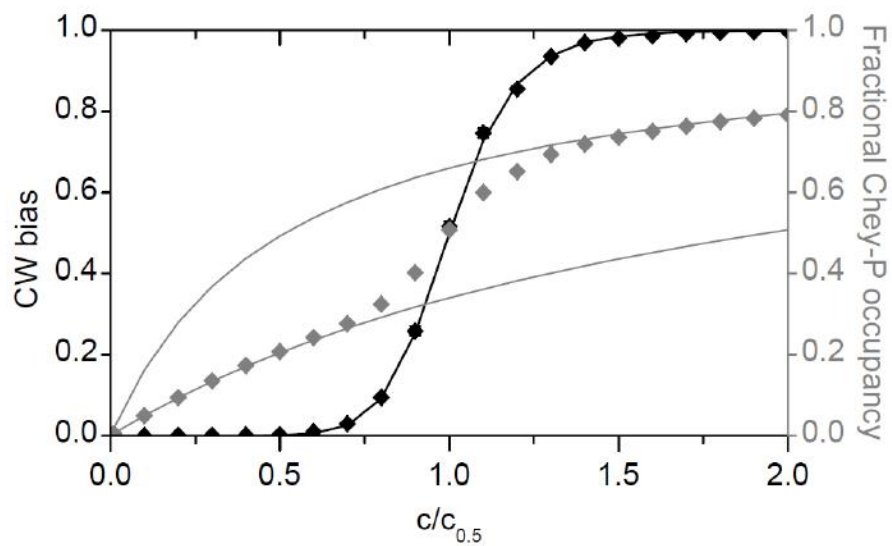
Figure 5.15. Simulated bias (black diamonds), and fraction of protomers with CheY-P bound (grey diamonds), versus CheY-P concentration parameter ($c/c_{0.5}$). A Hill fit (not shown) to the simulated bias gave a Hill coefficient of 9.4, but the bias is also well fit (black line) using a Hill coefficient of 10.1 as experimentally determined previously (Cluzel *et al.*, 2000). The simulated binding curve is bounded by the single-site Michaelis Menten dissociation curves for inactive (lower grey curve) and active protomers (upper grey curve), as expected from the model. Error bars showing standard errors of the mean are smaller than the symbols.

5.3 Conclusion

Having constrained the conformational spread model on the basis of a small subset of the experimental data, remarkable agreement was found between experiment and simulation across the entire dataset. We conclude that conformational spread provides an accurate representation of the flagellar switch, and the means by which signals are amplified at the end of the *E. coli* chemosensory pathway.

Modern theoretical treatments of allosteric regulation indicate that the conformational heterogeneity that results from stochastic coupling, both between different subunits and between binding and conformation, may be a selectable trait (Hilser, 2010). Presumably the protomers of the complex could have evolved to be more tightly coupled, suggesting that the multi-state activity observed here may provide functional advantages in flagellar switching. During chemotactic tumbling, the CW rotating filament undergoes a partial transition from a stable left-handed state to an unstable right-handed state. It has been argued that sufficiently long CW rotation would result in the formation of a stable right-handed state, ceasing tumbling (Macnab and Ornston, 1977). The possibility that intermittent pausing prevents this transformation has been discussed (Eisenbach *et al.*, 1990) and would appear to offer an advantage to multi-state switching over binary behaviour.

At lower time resolution the switch can be approximated as a two state system, which affords the convenience of applying the MWC model. The parameters of the MWC model are related to the conformational spread parameter E_A. The equilibrium constant, L, is given by $exp(\Delta G/k_B T)$ where ΔG is the free energy difference between CW and CCW states in the absence of ligand, equal to nE_A, where n is the number of protomers.

Meanwhile, the ratio of active to inactive dissociation constants is *exp(2E$_A$/k$_B$T)*. The understanding of receptor cooperativity in MWC terms helped to explain the variability in cluster sensitivity and amplification (Sourjik and Berg, 2004, Endres *et al.*, 2009), as discussed in Chapter 2. The switch does not appear to display any adaptation, such that the sensitivity of the switch to CheY-P concentration remains fixed at ~ 1 / 3 μM, and amplification is currently understood to be constant. However, the MWC framework may explain the apparent lowering of sensitivity with temperature (Turner *et al.*, 1999): the equilibrium constant increases with temperature (Turner *et al.*, 1996), leading to a decrease in sensitivity (see Chapter 2). Eventually, Turner *et al.* found that the physiological range of CheY-P concentration was unable to achieve high CW bias. At this point, it is possible that the switch sensitivity was beyond the operational value of 3 μM. This may have some bearing on thermotaxis, the biased random walk towards areas of preferable temperature (Sourjik and Wingreen, 2007), and also the pathway details of bacteria found naturally at different temperatures. For comparison, Haemoglobin is tuned between species living in different oxygen environments, with studies demonstrating that mutations at the interface of tetramer subunits are responsible for shifts in $K_{1/2}^{-1}$ (Koshland and Hamadani, 2002).

More widely, this work represents the first instance where the data appear to require the abandonment of classical allostery in favour of the general allosteric scheme to explain the conformational dynamics of a protein. Recent advances in resolving the functional states of a number of proteins have necessitated extensions of the classical models (Viappiani *et al.*, 2004, Karpen and Ruiz, 2002), suggesting other systems in which conformational spread may be observed. With the classical models encompassed at its

parameter space limits, we expect the model to be generally useful in understanding

allosteric cooperativity in proteins.

Chapter 6

Further work

6.1 Towards higher resolution

Important unknowns still surround the flagellar switch, with players in the network still being investigated. The dicarboxylate molecule fumarate, an intermediate in the citric acid cycle, has been shown to effect switching by lowering the free energy of the CW state relative to the CCW state in the presence and absence of CheY (Prasad *et al.*, 1998). Fumarate is unable to bind any element of the switch complex; instead, interaction proceeds via the membrane bound enzyme fumarate reductase, which is ordinarily responsible for converting fumarate to succinate for the purposes of anaerobic respiration (Cohen-Ben-Lulu *et al.*, 2008). The fumarate-bound enzyme binds FliG, although the details of docking between the membrane bound protein and rotating FliG are unclear. Fumarate reductase deletions result in poor motility due to reduced flagella number and non-switching motors, demonstrating an important role in both assembly and switching.

Another intriguing area is the role of acetylation, a second form of covalent modification to CheY, achieved by autoacetylation with acetyl coenzyme A (AcCoA) as an acetyl donor (Barak *et al.*, 2006), or catalysed by AcCoA synthetase with acetate or AcCoA as an acetyl donor (Barak *et al.*, 2004). Disruption of these mechanisms results in defective chemotaxis. Early investigation indicated that CheY acetylation increases the probability

of CW rotation (Barak *et al.*, 1992, Ramakrishnan *et al.*, 1998). However, a recent study determined that acetylation interferes with the binding of CheY to CheA, CheZ and FliM (Liarzi *et al.*, 2010). Since the concentrations of acetate, AcCoA and AcCoA synthetase depend on the metabolic state of the cell, acetylation may provide a means of connecting the chemotaxis pathway to metabolism.

Meanwhile, phosphorylation crosstalk between the dozens of two-component signalling pathways in the cell may present further sources of regulation. Further biochemical work is required to understand these mechanisms, but improvement in the biophysical techniques used to study flagellar rotation will provide further insight into the switching mechanism, and more generally, the kinetics of conformational spread.

At higher resolution, one may expect to detect $n+1$ discrete speed levels during motor switching, associated with the periodicity of the switch complex (n ~ 34) or more likely, the number of stator units applying torque (n ~ 10). Furthermore, interesting switching signatures should arise as the number of stator units present in the motor decreases. The linear relationship assumed between ring state and speed is reasonable for a complete complement of stator units, but is expected to breakdown at lower numbers. At this point the number, arrangement and turnover dynamics of units may have a significant effect on switching behaviour. With sufficient resolution, the stepping motion of the motor will become visible, providing the ultimate view of these kinds of activity, as well as insight into the difference between CW and CCW rotation at the mechano-chemical cycle level.

For motivation, we briefly consider the stepping behaviour of a switching motor with one stator unit. A modified version of the simulation code described in section 5.1.2 was used

here, written in MATLAB. In addition to transition times for changes in activity and binding on the ring, a transition time is assigned for the next conformational change of a single stator unit. The unit is assumed to be a Poisson stepper. The rate of stepping is set by considering a motor rotating at 100 Hz (a reasonable value at low load, where one stator drives the motor as fast as a full complement (Yuan and Berg, 2008)), with 26 steps per revolution (Sowa *et al.*, 2005). The rotor, upon which the stator acts, is assumed to consist of 26 FliG subunits and 34 FliM subunits, arranged according to the model of Brown *et al.*, 2007, where eight approximately uniformly spaced FliM subunits do not communicate with FliG. A one-to-one correspondence in activity is assumed between the remaining 26 FliM-FliG pairs, where the activity of FliM is according to the constrained conformational spread model of Chapter 5. The angle of the rotor in units of steps relative to an arbitrary start angle is noted at every iteration of the Monte Carlo simulation and saved at the sampling frequency. The stator unit remains fixed relative to this start angle. Upon conformational change of the stator unit, the state of the local FliG subunit determines the direction of the step. Following on from the crossbridge-type stepping mechanism (Kojima and Blair, 2002) that considers a high duty ratio (Ryu *et al.*, 2000), it is assumed that the step is only taken if the destination subunit shares the same state as the local subunit. Switch events in the simulation are shown in Figure 6.1. Evidently, the motor is brought to a near stand-still during complete and incomplete switches, taking only a few steps backwards and forwards about a fixed angle for most of the duration of the event, as it catches up with the boundaries of CW and CCW activities on the ring.

Recent work on the low load regime of motor function (Yuan and Berg, 2008, Yuan *et al.*, 2009) identifies the next generation of bacterial flagellar motor experiments that will

Figure 6.1. Examples of switching events at the stepping resolution, with one stator. The activity of the switch is shown in blue, while the stepping of the motor is shown in green. 26 steps correspond to one revolution. The motor pauses as the switch undergoes conformational spread. The figure is continued on the next page.

116

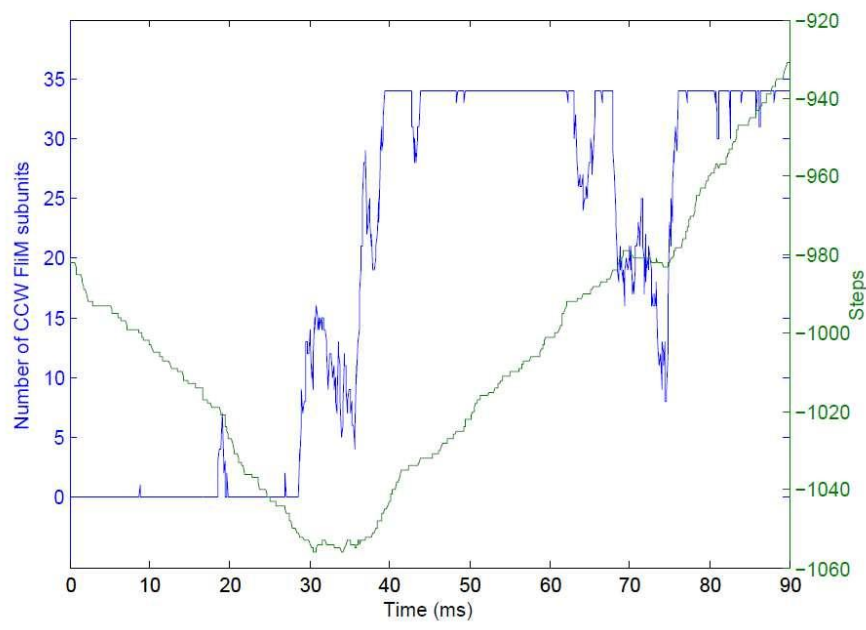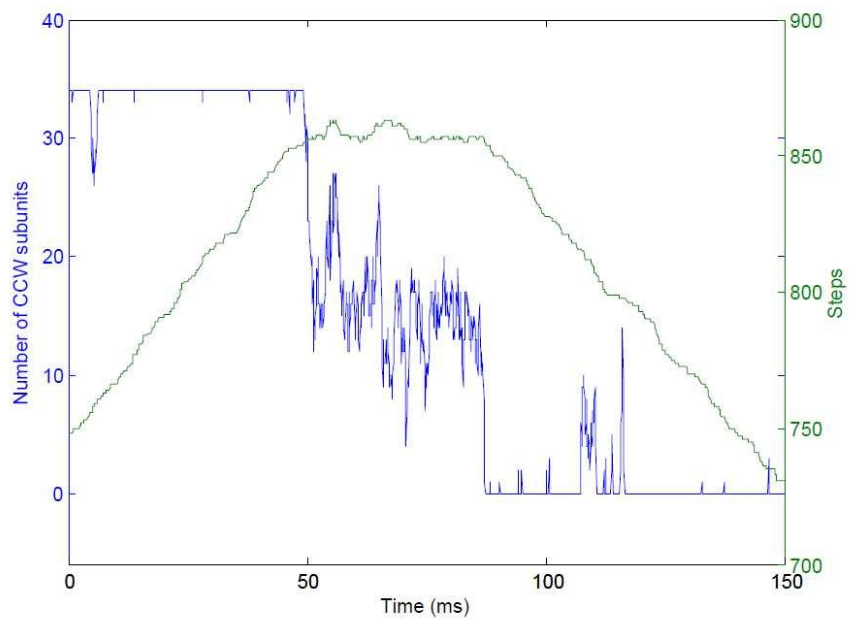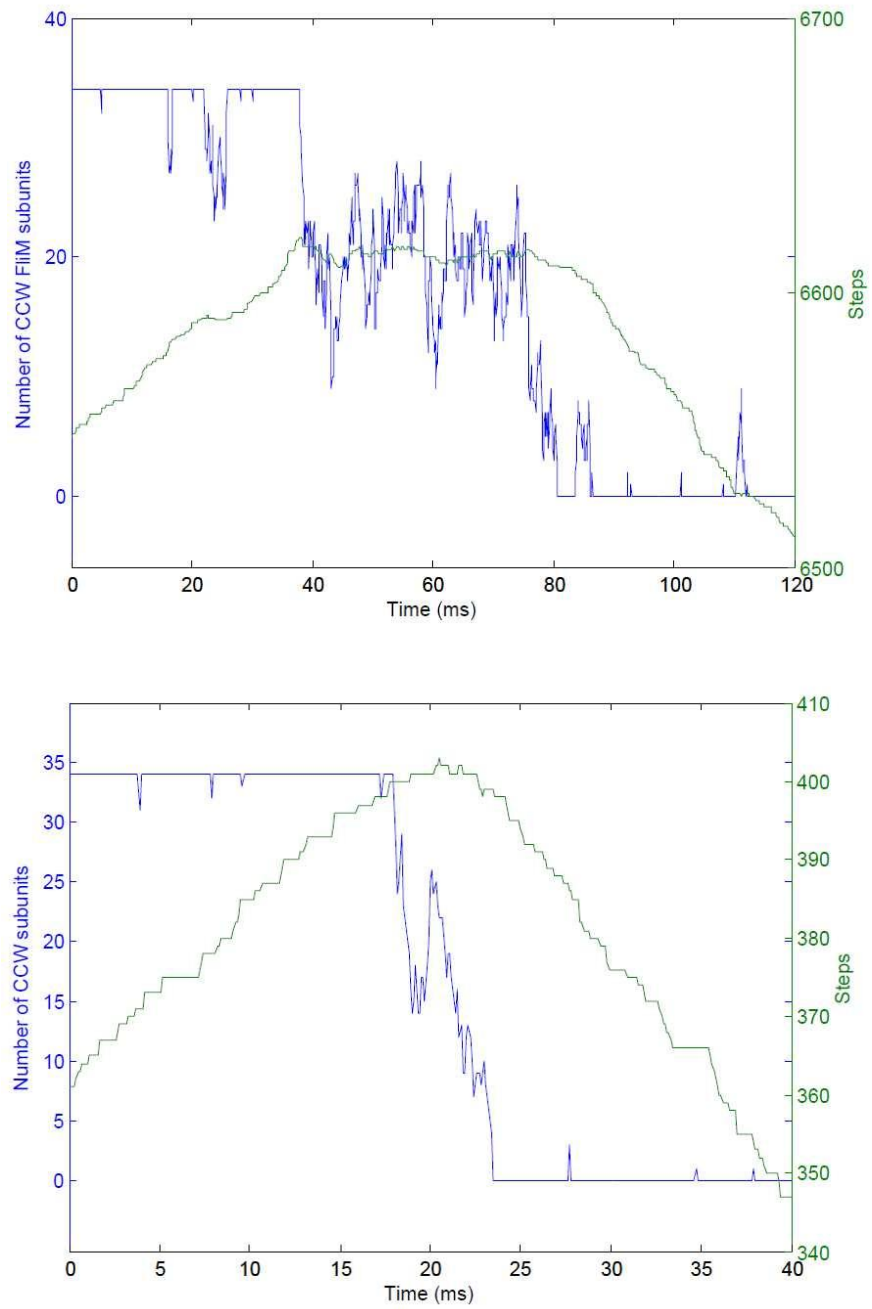Figure 6.1 continued. Examples of switching events at the stepping resolution, with one stator. The activity of the switch is shown in blue, while the stepping of the motor is shown in green. 26 steps correspond to one revolution. The motor pauses as the switch undergoes conformational spread.

allow investigation of this kind of behaviour. The monitoring of gold nanoparticles attached directly to hooks as described in Chapter 1 provides a two fold advantage for switch experiments. Firstly, the size of the particle and absence of flagellar stub reduces the relaxation time, and lower limit of time resolution, to ~ 8 μs for a gold nanoparticle of diameter 80 nm (Baker and Berry, 2009), over 100 times shorter than the relaxation time of a 0.5 μm diameter plastic bead. This is sufficient to observe stepping at rotation rates of order 100 Hz. Secondly, it appears that switching kinetics will be slower at low load. Yuan and Berg, 2009, demonstrated that the conformational spread model reproduces the relationship between switching rates and load, in the low load regime, if the fundamental flipping frequency decreases with decreasing load. In conformational spread simulations (Chapter 5), the switch duration, and complete and incomplete switch intervals increase for reduced flipping frequency (Figure 6.2). Consequently, it is expected that all elements of switching will slow down with decreasing load, providing an improved ability to resolve multi-state behaviour. The first steps towards realising this level of resolution are described in the next section.

6.2 Experimental preliminaries

Strain An existing strain from Dr. Y. Sowa (a former postdoctoral researcher in the Berry group) was selected for low-load switching experiments on the basis of being wild-type for chemotaxis, and lacking filaments and stators (YS33 (ΔpilA, fliC::Tn10, ΔmotAmotB)). An existing plasmid (pDB27 (motAmotB Arabinose inducible, Ampicillin resistant)) was selected for stator protein induction.
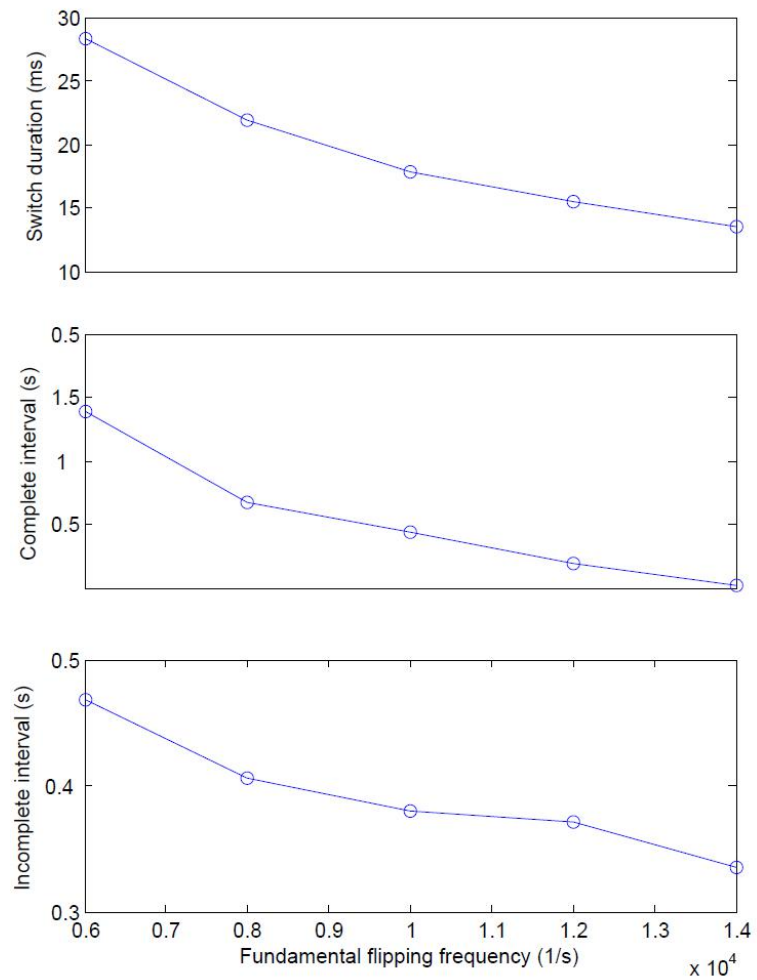
Figure 6.2. Switching as a function of fundamental flipping frequency in simulations of the constrained conformational spread model described in Chapter 5. Each data point represents the mean of the feature in question, measured from 50 records, each 30 s long.

Competent cells were prepared using the calcium chloride method of Sambrook and Russell, 2001. 3 µl of plasmid was transformed by incubation with 200 µl of the competent cells on ice for 1 hour, followed by 2 min at 42 °C and 2 min on ice. 1 ml of LB was added and incubated at 37 °C for 1 hour. The mixture was spread on LB-agar plates containing ampicillin and stocks produced.

Sample preparation Cells were grown aerobically from a 100 µl aliquot of frozen stock for 5 h at 30 °C with shaking at 180 rpm, in tryptone broth (1% tryptone; 0.5% sodium chloride) containing ampicillin antibiotic at 100 µM to preserve plasmids. 100 nm gold nanoparticles (Corpuscular Inc., USA) were attached to cell hooks by antibody interaction as follows, based on the protocol of Yuan and Berg, 2008. Primary antibody (rabbit anti-hook antibody, provided as a gift from H. C. Berg) was purified using a purchased kit (Dojin-Do, Japan). Secondary antibody (goat anti-rabbit antibody, Sigma-Aldrich, UK) was conjugated to LC-SPDP (Sigma-Aldrich, UK) for attachment to gold. 500 µl of 2.5 mg/ml secondary antibody (diluted by PBS-EDTA) was combined with 12.5 µl of 20 mM LC-SPDP in DMSO and incubated for 30 min. The product was filtered with a Zeba spin column (Perbio Science, UK) following kit instructions. Antibody aliquots were stored at -80 °C.

500 µl of gold stock solution was combined with 3 µl of secondary antibody – LC-SPDP and incubated for 3 hrs. 500 µl of the solution was combined with 10 µl of 1mM MPEG-SH (Sigma-Aldrich, UK) in DMSO. MPEG serves as blocker to prevent gold interaction with cell bodies. The product was incubated overnight and stored at 4 °C for use within two weeks.

1 ml of cell culture was washed three times with final suspension in 400 μl of motility buffer (6.2 mM K_2HPO_4, 3.8 mM KH_2PO_4; 0.1mM EDTA at pH 7.0). 1 μl of primary antibody stock was diluted 100 times, and 10 μl of the product combined with 100 μl of cell solution. Product was incubated for 25 min allowing conjugation of primary antibody to hooks. Coverage was assessed by tethered cell analysis (hook-only cells do not tether unless treated).

Product was washed three times with final suspension in 40 μl of motility buffer. This was added to the pellet produced by spinning down 100 μl of gold solution. The product was incubated for 25 minutes, allowing conjugation of gold to hooks. The product was washed and resuspended in 200 μl of motility buffer, for use in a standard tunnel slide (see Chapter 3 for description). Full protocol details are given in Appendix A.

Observations An existing laser darkfield microscopy setup constructed by Dr. Y. Sowa and Dr. B. Steel was used for sample assessment. Laser light is focused by an objective lens onto the sample. The back-scattered light from gold nanoparticles is collected by the objective lens and focused onto the CCD of a high speed camera, for position detection of the nanoparticle by Gaussian fitting. A brightfield illumination path allows candidate spinners to be located. Of the number of cells with gold attached (of order 10 %), less than 10 % are found to be spinning and typically only one spinner of sufficient quality is found per slide. The low yield of the assay prevents the high volume of data collection that will be necessary to elucidate the workings of the motor and switch. Investigation continues into improving the yield of the assay.

Microscope stage system The improved resolution provided by the gold nanoparticle assay increases the need to reduce external noise sources. The commercial coarse dovetail stage and fine-positioning piezo stage in the current setup are chief contributors, coupling mechanical and electrical noise to the sample (personal communication, Dr. B. Steel). The high-end piezo system used to locate motors in previous investigations (Sowa *et al.*, 2005) provided a resolution of ~ 0.1 nm in positioning. High-end differential micrometers are only able to achieve resolutions up to ~ 20 nm, but may be sufficient for locating the size of markers (~ 100 nm) intended for use. Meanwhile, the micrometer setup is without electrical noise and is expected to provide greater system stiffness than the piezo setup. The design of a stable piezo-less stage is detailed here, inspired by an existing piezo-carrying coarse stage system designed by Dr. R. Berry.

The basic design comprises a three-axis stage around the objective lens (Figure 6.3). Full technical drawings of the system are provided in Appendix B. Translation in the x axis is allowed through three double-row ball bearing linear stages (part no. M-UMR5.16, Newport, UK). Translation is controlled by a differential micrometer (part no. DM11-16, Newport, UK) screwed into the central linear stage. Each linear stage contains two springs; all springs except for the outer pair in the farther two linear stages from the micrometer are removed to reduce the load on the micrometer to an acceptable level. These farther linear stages are spaced as widely as possible to increase stability. Translation in the y axis is performed similarly.

The z-plate is mounted kinematically. Here, x and y translation of the z-plate is restrained by a kinematic screw (part no. 9377-K, Newport, UK) through the z-plate, mounted into a conical section of the base plate. Pitch and yaw of the z-plate is restrained by another
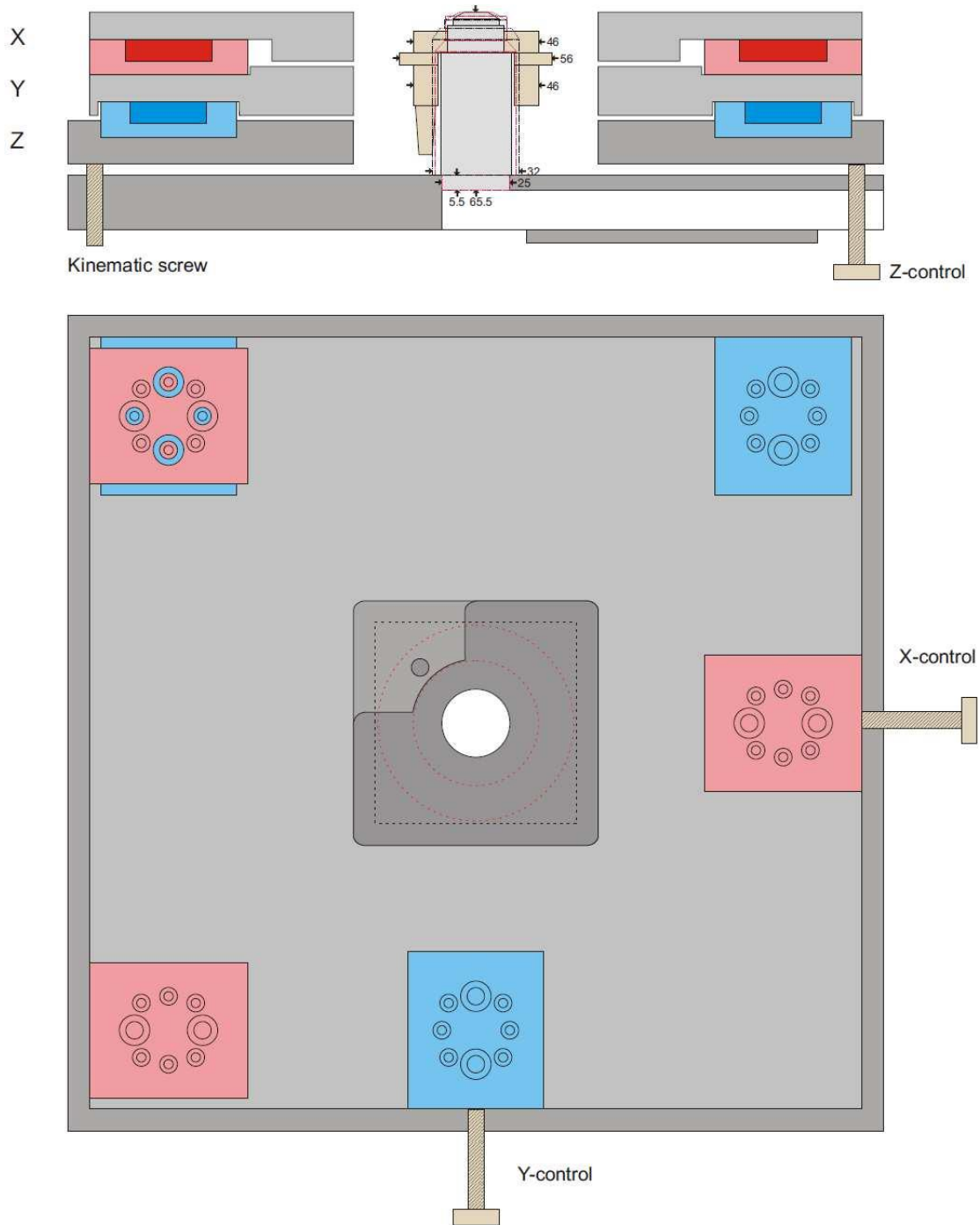
Figure 6.3. Basic design of piezo-less stage. The top diagram shows selective side sections, while the bottom diagram shows selective plan views. Linear stages for x-axis control are shown in red, those for y-axis control in blue (light elements are secured to the plate below, while dark elements are secured to the plate above, allowing relative movement). Only one of the two kinematic screws is visible. The objective, shown with custom temperature controller attached (together with the limits of other objectives available for use, depicted by dotted lines), is screwed into the base-plate with the tunnel for the scattered light path visible in the side section. Objective dimensions are in mm. The z-plate tongue for locking is visible near to the objective screw hole in the plan view. Red dotted lines represent the the limits of the temperature controller, while black dotted lines represent the limits of plate movement

kinematic screw through the base-plate mounted into a v-shaped groove section of the z-plate. Translation in the z-axis is then possible via roll of z-plate in the v-shaped groove section. Roll is controlled by a high-load bearing micrometer (part no. MDE216, Elliot Scientific, UK) screwed into the base plate and mounted onto a flat section of the z-plate. Kinematic mounts are constructed from steel and inserted into the aluminium plates, for extra hardness. During measurement, noise may be reduced by locking the z-plate to the base-plate. This is achieved with a screw passing through both plates; the screw passes through the z-plate at a tongue-section protruding into the central aperture close the objective lens. This section is reduced in thickness to allow flexing of the z-plate and fine-adjustment of the z-axis position.

It is reasoned that a larger mass will be less susceptible to mechanical noise: the dimensions of the plates are made as large as possible given restrictions on optical air table space, and as thick as possible given the restriction of objective lens height. (The objective is mounted directly into the base plate, allowing the back aperture to be as close as possible to a mirror collecting back-scattered laser light. This ensures that the maximum amount of light is collected. The light is directed through a tunnel within the base plate before exiting for imaging). The central aperture in the plates is made as large as necessary to allow for the fitting of a custom temperature controller (provided by M. Baker) to the objective lens. The base plate is mounted on a custom optical box housing opto-mechanics for the darkfield and brightfield light paths. The box contains pillars to support the stage, with spacing calculated to avoid standing wave modes in the setup.

Using these designs, the stage is currently under construction by the workshop in the Department of Physics, University of Oxford. It is hoped that the setup will provide the basis for low noise, high resolution experiments on bacterial flagellar motor dynamics.

Appendix A

A1. Tunnel slide

To construct the tunnel slide:

1. Wash 22 x 22mm clean coverslip with clean water and place in laminar flow to dry.
2. Clean slide with ethanol and lay down two pieces of tape (avoiding air bubbles) to make tunnel.
3. Lay dry coverslip (hair-dry if necessary) over tunnel and 'colour-in' with pipette tip to achieve good contact.
4. With razor, cut away excess tape.
5. Shear 0.7 ml of culture 50 times with shearing device – maintain high pressure through shearing.
6. Spin cells 7000 rpm for 2 mins
7. Empty supernatant, add 1ml of motility buffer (MB), and pipette up-and-down to stir.
8. Repeat step 6/7 twice, but after last spin add 250 μl of MB.

To load the tunnel slide:

9. Flow 10 ul of polylysine into the tunnel, and use tissue to wick exiting flow. Leave for 1 minute.
10. Wick through 50 μl of MB to wash.
11. Wick though 10 μl of cell solution.
12. Leave slide inverted in humidity chamber for 10 minutes.
13. Wick though 50 μl of MB to wash.
14. Wick though 10 μl of bead solution
15. Leave slide inverted in humidity chamber for 10 minutes.
16. Wick though 50 μl MB to wash and exchange buffers
17. Seal tunnel ends with grease to avoid evaporation.

A2. Flow slide

To construct the flow slide:

1. Wash 22 x 40mm clean coverslip with clean water and place in laminar flow to dry.
2. Clean slide with ethanol and lay down tape across all three holes evenly.
3. With razor, cut out Y-channel and remove with tweezers.
4. Place coverslip over Y-channel and fully 'colour-in' tape with pipette tip

To prepare the cells:

5. Shear 14 ml of cell culture 50 times with shearing device (do two lots of 7ml).
6. Spin cells 7000 rpm for 2 mins, empty suspension, add 1ml of motility buffer (MB), pipette and vibrate to stir.
7. Repeat step 6 twice – after last spin add 250 μl of MB

To load the flow slide:

8. Inject MB into entry tube 1 with syringe to fill slide system and seal entry tube 2
9. Inject polylysine into entry tube 1 with syringe and leave for 1 min.
10. Inject MB to wash
11. Inject cells and leave for 15 min
12. Inject MB to wash
13. Inject beads and leave for 10 min
14. Inject MB to wash
15. Attach MB container and attractant container to entry tubes and close ends with clips

A3. Gold nanoparticle assay

Preparing primary antibody

1. Purify 50 μL of rabbit anti-hook antibody from Howard Berg's laboratory using IgG purification kit-A (Dojin-Do) following kit instructions.
2. Measure purified antibody using the Bradford Method. BSA or purchased IgG (R5506 from Sigma, UK) can be used for standard calibration curve.
3. The purified antibody may be around 0.25 mg/mL
4. Fast freeze aliquots in liquid nitrogen and store in -80 C freezer.

Preparing secondary antibody

1. Wash Zeba spin column using PBS-EDTA following kit instructions.
2. Mix 500 μL of 2.5 mg/mL IgG (diluted by PBS-EDTA) and 12.5 μL of 20 mM LC-SPDP in DMSO and incubate for 30 min.
3. Filter with washed column.
4. Fast freeze aliquots (5-10 μL) in liquid nitrogen and store at -80 C freezer.

Preparing gold nanoparticle solution

1. Vortex gold stock (stored in 4 C fridge).
2. Combine 500 μL of gold stock and 3 μL of IgG LC-SPDP (stored in -80 C freezer), then straight away vortex for 1 s, avoiding bubbles throughout.
3. Incubate for 3 hrs.
4. Combine the 500 μL of gold solution with 10 μL of 1mM MPEG-SH in DMSO (stored in -20 C freezer), and vortex for 5 s, avoiding bubbles throughout.
5. Incubate overnight (12-14 hours).
6. Store in 4 C fridge and use within two weeks

Preparing the tunnel slide

1. Wash 1mL of cell culture (spin down in centrifuge (always at 7000 rpm for 2 min), remove supernatant and resuspend in 1 mL motility buffer (MB). Repeat another two times with final suspension in 400 μL of MB.

2. Dilute 250 μg/mL of purified rabbit anti-hook antibody (αFlgE) down to 2.5 μg/mL, placing on ice during preparation.

3. Combine 100 μL of the cell culture and 10 μL of antibody. Flick to mix and incubate for 25 minutes. Store remaining antibody in -20 C freezer and diluted antibody in fridge, for use within a couple of weeks.

4. Spin down and remove all supernatant carefully with a pipette, and resuspend in 300 μL of MB. Repeat another two times with final suspension in 40 μL of MB.

5. Spin down 100 μL of gold nanoparticle solution and remove as much supernatant as possible, carefully with pipette.

6. Combine 40 μL of the cell culture to the remaining gold pellet and mix with pipette, being careful to avoid bubbles.

7. Incubate for 25 min

8. Spin down, remove all supernatant carefully with pipette and resuspend in 200 μL of MB.

9. Proceed with tunnel slide.

Appendix B

B.1 Stage plans

Overleaf are technical drawings for the x,y,z and base plates of the piezoless stage discussed in Chapter 6, as well as the optics box on which the stage is mounted.

X plate (top)

Drawing scale 2:1. Real world dimensions in mm.
(x, y) drill coordinates in mm, with origin (0, 0) at
bottom-left corner of plate.

◎ M3 counterbored clearance

▱ 284

129.5

25   15

(19, 265)   (39, 265)

(19, 245)   (39, 245)

(129.5, 202) (142, 202) (154.5, 202)

▱ 90

⌀ 10

These nine holes around
square aperture: M4 tap, 9mm deep

(82, 154.5)

(202, 154.5)   (245, 152)   (265, 152)

(82, 142)

(142, 142)   (202, 142)

(82, 129.5)

(202, 129.5)   (245, 132)   (265, 132)

(129.5, 82)   (142, 82)   (154.5, 82)

(19, 39)   (39, 39)

(19, 19)   (39, 19)

X plate (bottom)

Drawing scale 2:1. Real world dimensions in mm.
(x, y) drill coordinates in mm, with origin (0, 0) at
bottom-left corner of plate.

A

B

3

52

67

67

52

52

67

116

3

A

8

8

8

B

18

Y plate (top)

Drawing scale 2:1. Real world dimensions in mm.
(x, y) drill coordinates in mm, with origin (0, 0) at
bottom-left corner of plate.

◎ M3 counterbored clearance

3

☐ 284

129.5

(19, 265)   (39, 265)

A →

(245, 265)   (265, 265)

25

15

52

(19, 245)   (39, 245)

(245, 245)   (265, 245)

These four holes:
M3 clearance only,
no counterbore

59

☐ 90

⌀ 10

59

(255, 154.5)

(142, 142)

52

(242.5, 142)   (267.5, 142)

B →

(255, 129.5)

116

59

(29, 41.5)

(16.5, 29)   (41.5, 29)

C →

52

3

(29, 16.5)

A

3

5

3

B

5

C

3
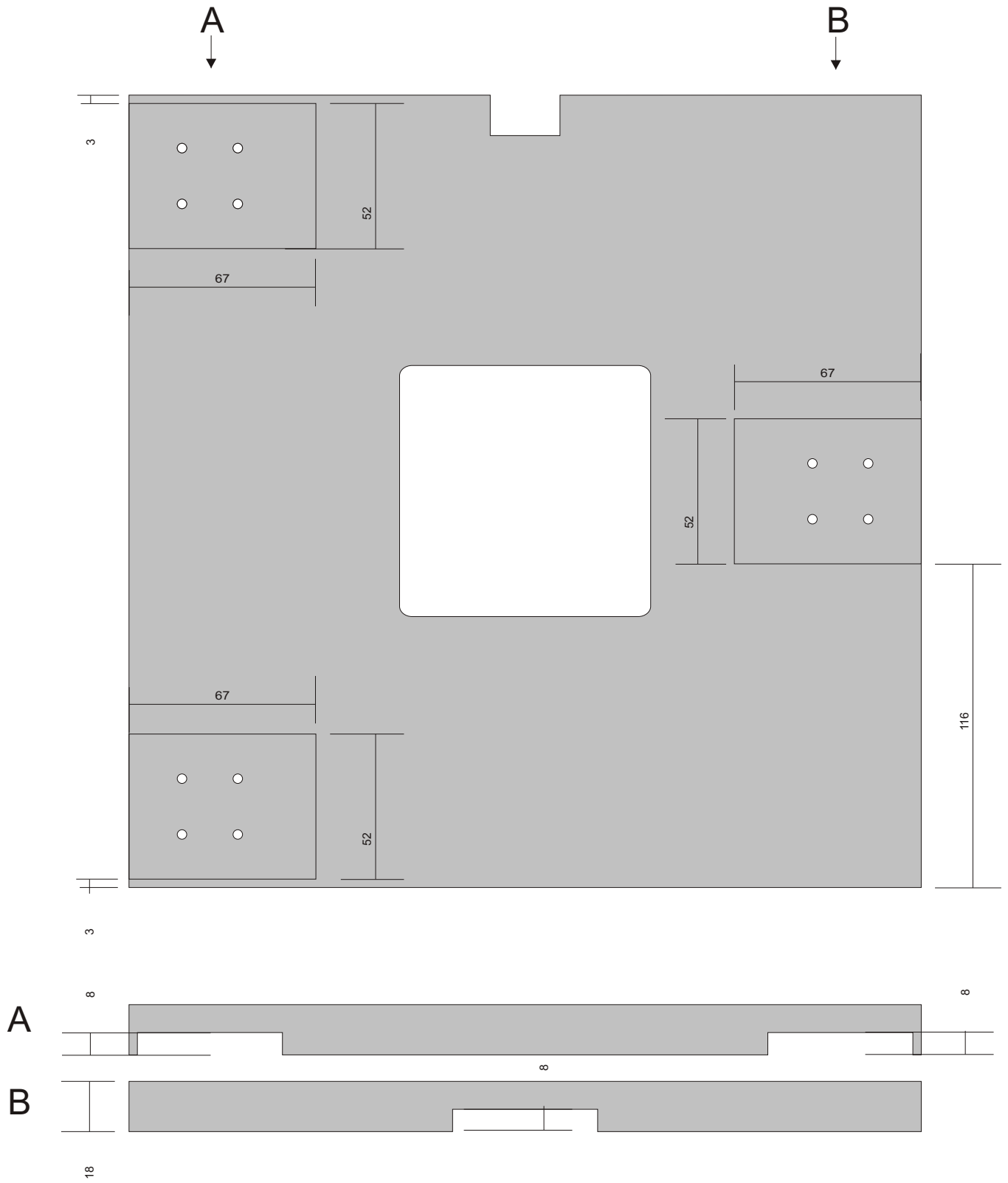
5

18

Y plate (bottom)

Drawing scale 2:1. Real world dimensions in mm.
(x, y) drill coordinates in mm, with origin (0, 0) at
bottom-left corner of plate.

M6 counterbored clearance

M3 counterbored clearance

3

3

These four holes:
M3 clearance only,
no counterbore

67

67

52

52

52

67

116

Z plate (top)

Drawing scale 2:1. Real world dimensions in mm.
(x, y) drill coordinates in mm, with origin (0, 0) at
bottom-left corner of plate.

▱ 300

11

11

7

7

⌀ 8.8 +/- 0.03
(150, 290)

(37, 275)

(263, 275)

(24.5, 262.5)

(49.5, 262.5)

(250.5, 262.5)

(250.5,262.5)

60

60

(37, 250)

(263, 250)

52

52

A →

▱ 90

48

4mm thick
tongue

(129.5, 170.5)

M6
clearance

⌀ 47

48

⌀ 10

52

(150, 49.5)

67.5

(137.5, 37)

(162.5, 37)

(150, 24.5)

B →

124

6

6

A

16

6

6

B

6

6

Z plate (bottom)

Drawing scale 2:1. Real world dimensions in mm.
(x, y) drill coordinates in mm, with origin (0, 0) at
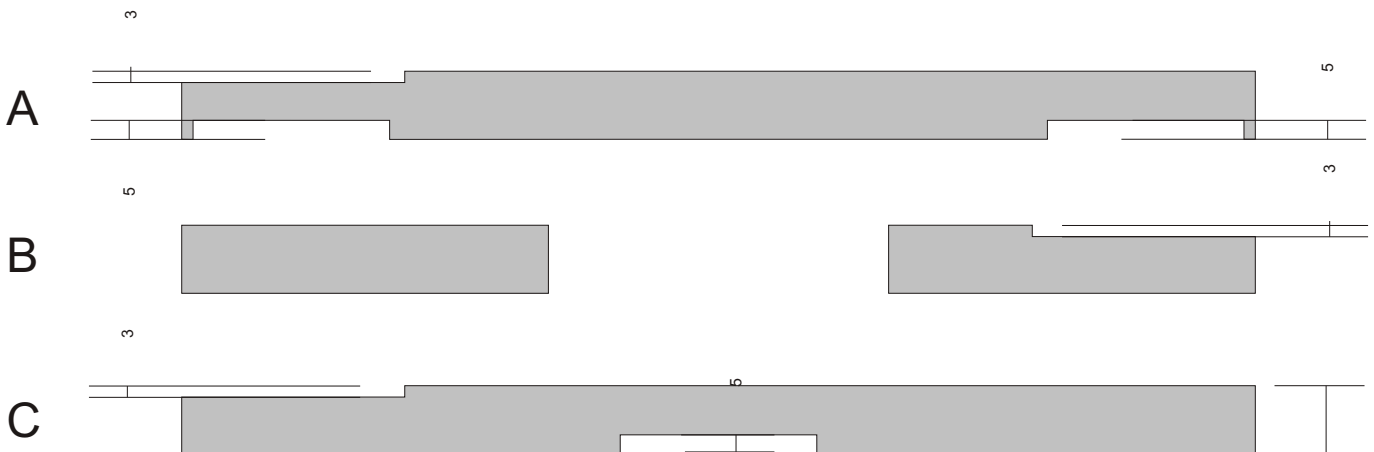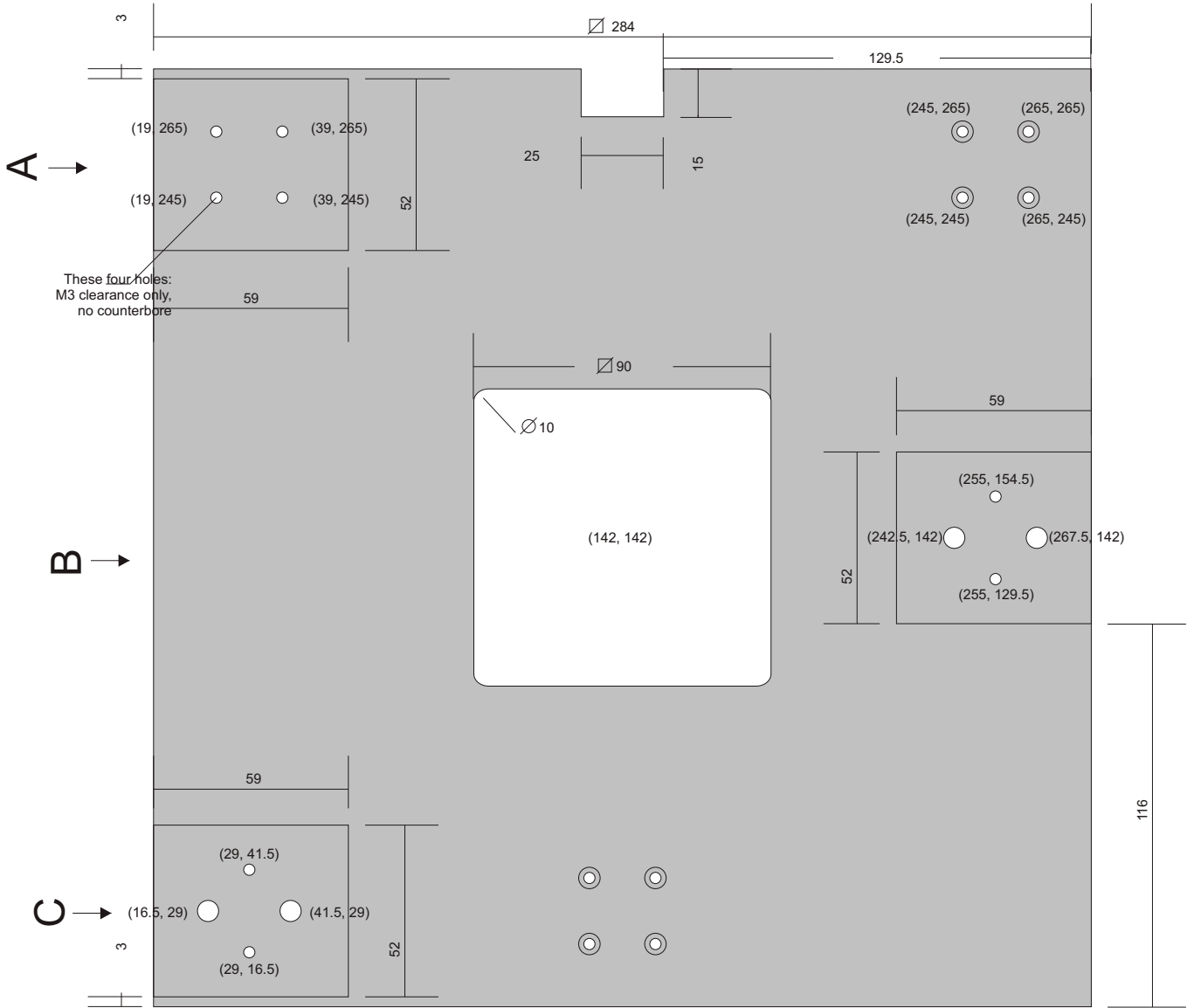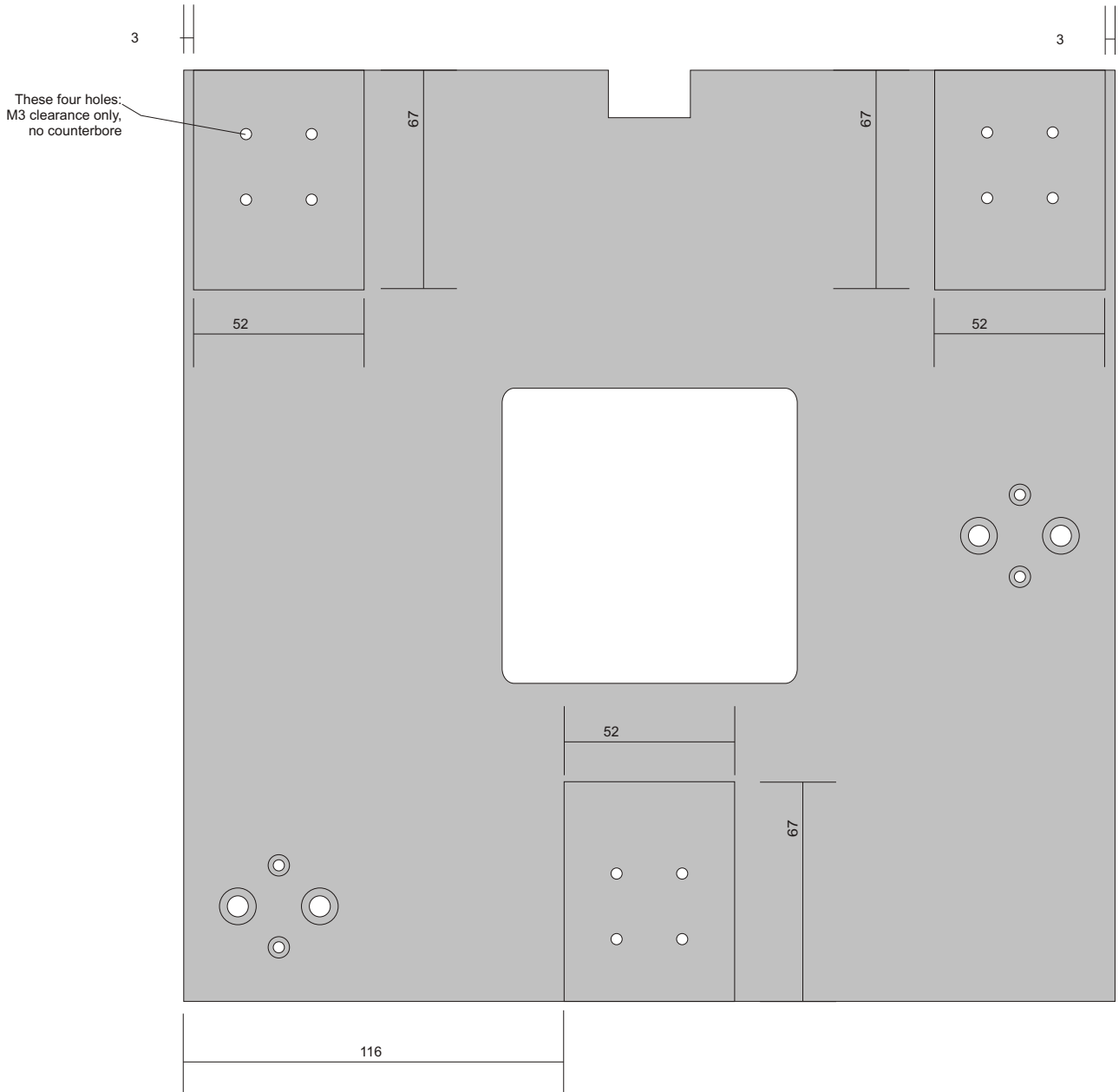bottom-left corner of plate.

M6 counterbored clearance

M3 counterbored clearance

M3 counterbored clearance

counterbore: ⌀ 10.4, depth 0.8

Steel piece depicted below to be
screwed into this corner

These two holes:
M3 tap, 3mm deep

⊿25

(5.25, 19.75)

(19.75, 5.25)

These two holes:
M3 tap, 3mm deep

⊿25

Steel piece depicted below to be
screwed into this corner

(294.75, 19.75)

(280.25, 5.25)

Drill out triangular
cross-section groove,
4mm in width
3mm deep

⊿25

63.4 degrees

(5.25, 19.75)

(19.75, 5.25)

5

Top

Side

6

⊿25

Top

(19.75, 19.75)
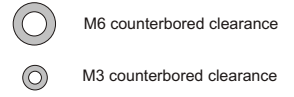
(5.25, 5.25)

Side

6

Base plate (top)

Drawing scale 2:1. Real world dimensions in mm.
(x, y) drill coordinates in mm, with origin (0, 0) at
bottom-left corner of plate.
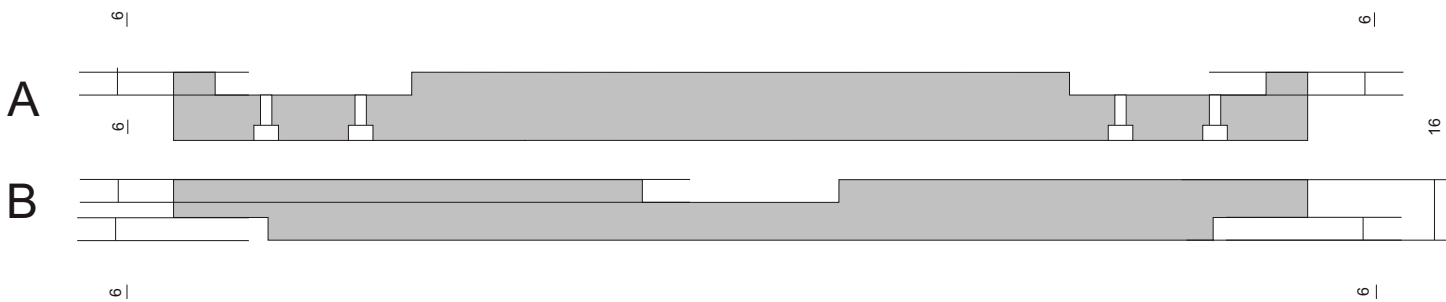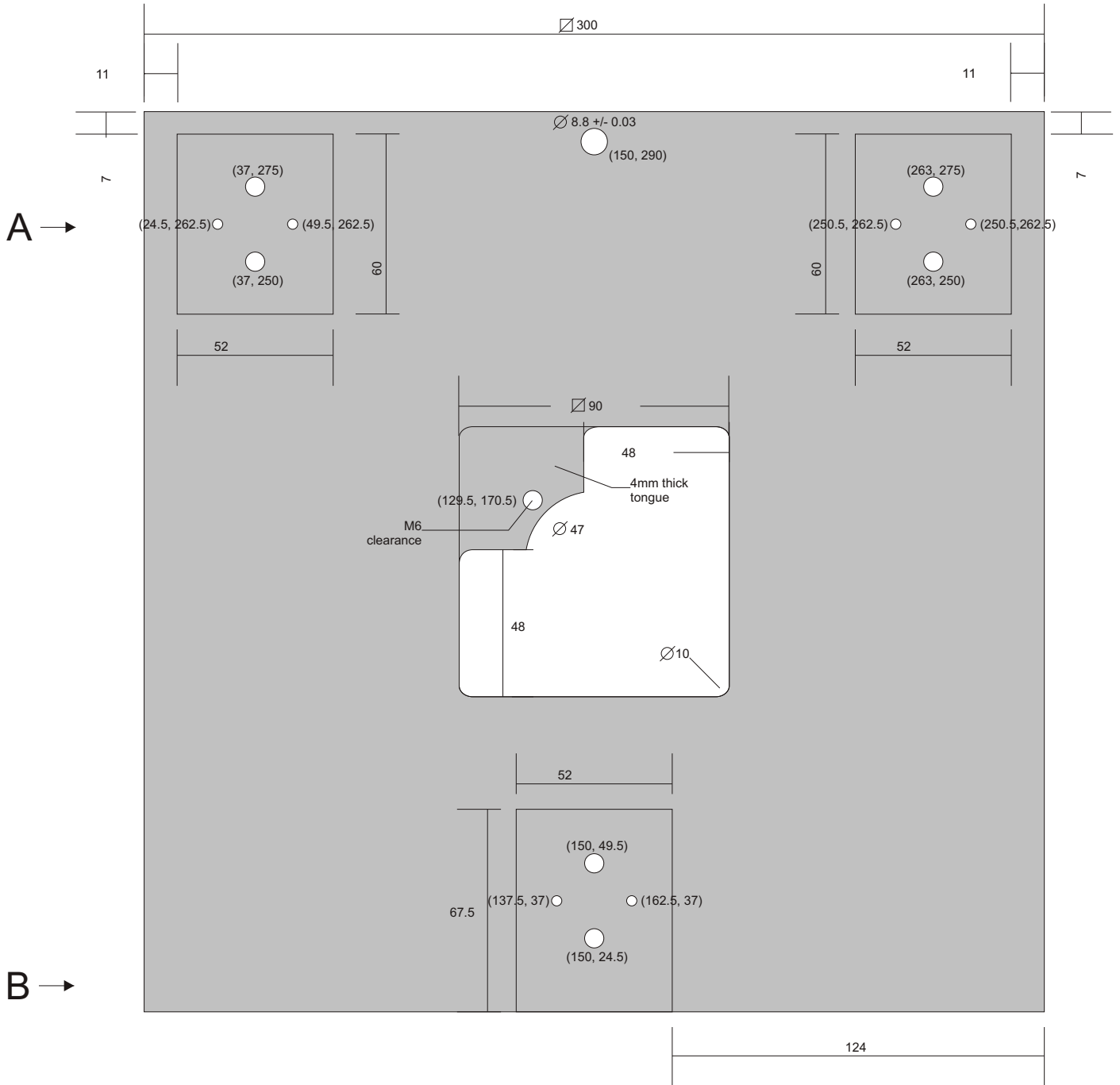
◯ M6 counterbored clearance

◯ M3 counterbored clearance

▱ 25

Top

(5.25, 19.75)

(12.5, 15)

(19.75, 5.25)

drill out cone,
4mm in diameter
3mm deep

6

Side

(142.75, 294.75)

(157.25, 280.25)

(12.5, 287.5) (62.5, 287.5) (112.5, 287.5) (187.5, 287.5) (237.5, 287.5) (287.5, 287.5)

Steel piece depicted above to be
screwed into plate here

These two holes:
M3 tap, 3mm deep

▱ 25

(12.5, 237.5) (137.5, 237.5) (162.5, 237.5) (212.5, 237.5) (287.5, 237.5)

M6 tap, 15mm deep

(12.5, 187.5) (137.5, 187.5) (162.5, 187.5) (212.5, 187.5) (287.5, 187.5)

(129.5, 170.5)

(150, 150)

Tap should be determined from
microscope objective (to be provided)

(12.5, 137.5) (287.5, 137.5)

(112.5, 112.5)

(12.5, 87.5) (212.5, 87.5) (287.5, 87.5)

⌀ 8.8 +/- 0.03

(10, 10)

Counterbore:
⌀ 17, 3.5mm deep

(290, 10)

⌀12

(62.5, 12.5) (137.5, 12.5) (212.5, 12.5)

To hold steel
adaptor depicted
below

counterbore: ⌀ 10.4, depth 0.8

▱ 300

⌀ 16.98

Top

M9.5X
0.5-6g
thread

3.5

Cross-section

11.98

14.5

Base plate (bottom)

Drawing scale 2:1. Real world dimensions in mm.
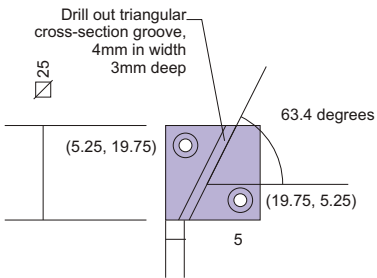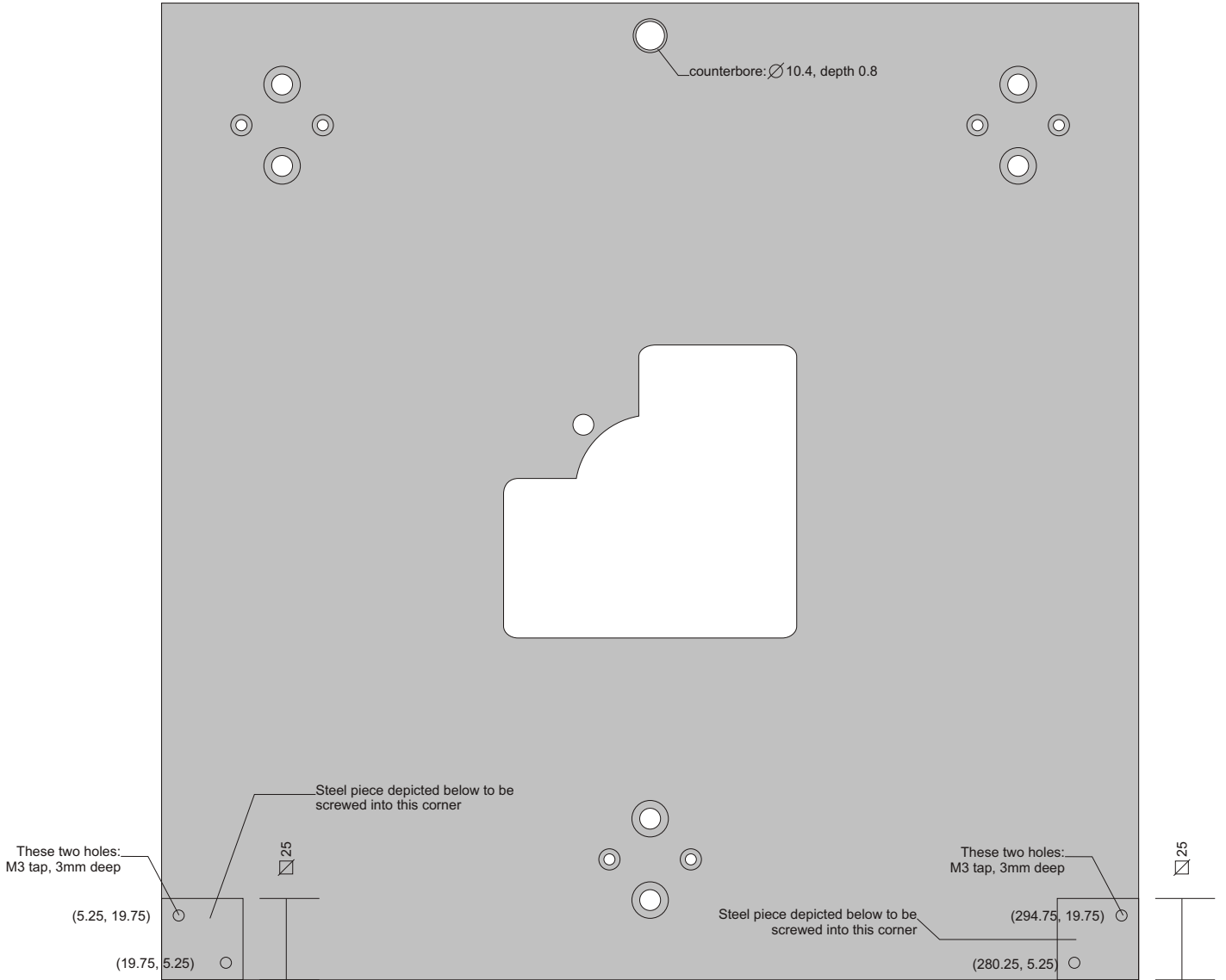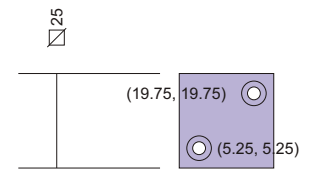(x, y) drill coordinates in mm, with origin (0, 0) at
bottom-left corner of plate.

B   B   C   C

A →

45 degree slant

$\varnothing 36$

(135, 165)   (165, 165)   (195, 165)   (225, 165)   (255, 165)

(150, 150)

These four holes around the aperture:
3 mm deep, # 4-40 tap

$\varnothing 12$

(135, 135)   (165, 135)   (195, 135)   (225, 135)   (255, 135)

144

These six holes parallel to the tunnel
(will accommodate cover depicted below):
M3 tap, 3mm deep

7

Counterbore:
$\varnothing 19$, 5.5mm deep

$\varnothing 12$

20

A

6mm thick

7

(20, 37.5)   (50, 37.5)   (80, 37.5)

45

20   (0, 0)

(20, 7.5)   (50, 7.5)   (80, 7.5)

102.5

M3 counterbored clearance

Optics box

Drawing scale 2:1. Real world dimensions in mm.
(x, y) drill coordinates in mm, with origin (0, 0) at
bottom-left corner of plate.

Top and bottom view

Part A

Part C

Part D

Part B

Rectangular cut-out (7mm deep) only on top side

Part E

64

47

Part E

Outer
face

(10, 117.5)

(210, 117.5)

(285, 117.5)

(10, 75)

(210, 75)

(285, 75)

(10, 32.5)

(210, 32.5)

(285, 32.5)
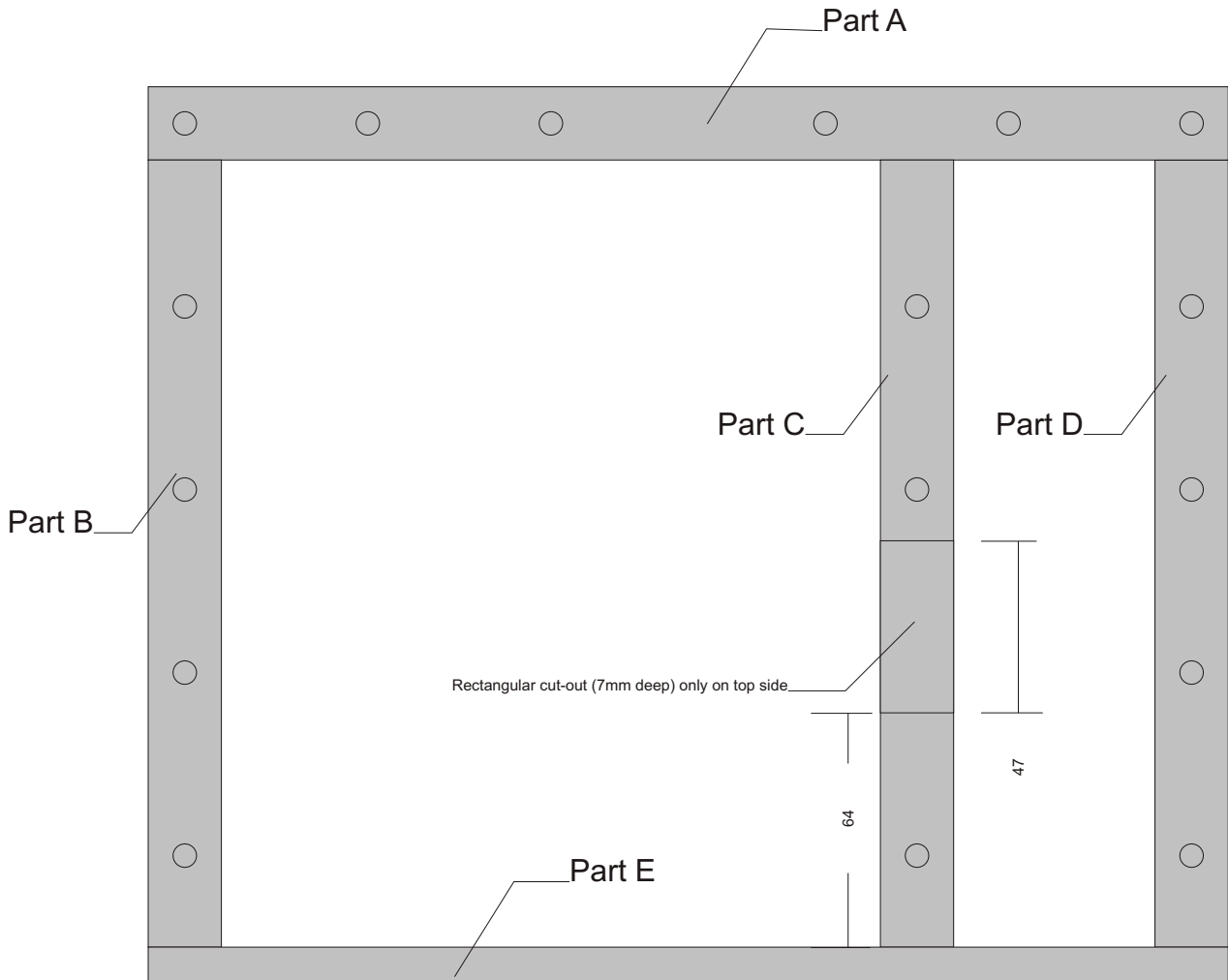
Top/
bottom

Optics box

Drawing scale 2:1. Real world dimensions in mm.
(x, y) drill coordinates in mm, with origin (0, 0) at
bottom-left corner of plate.

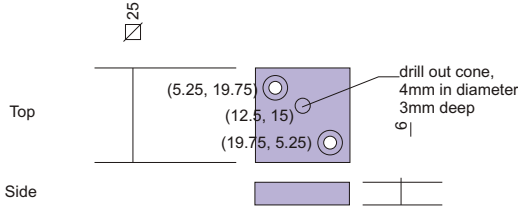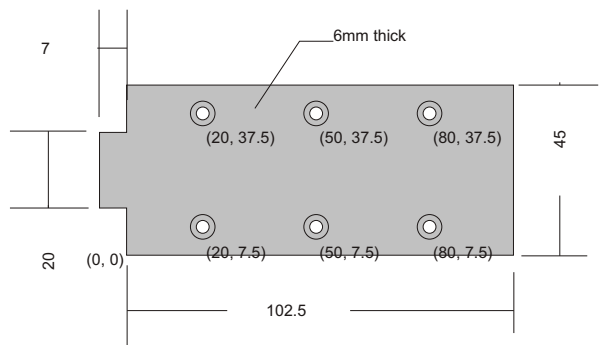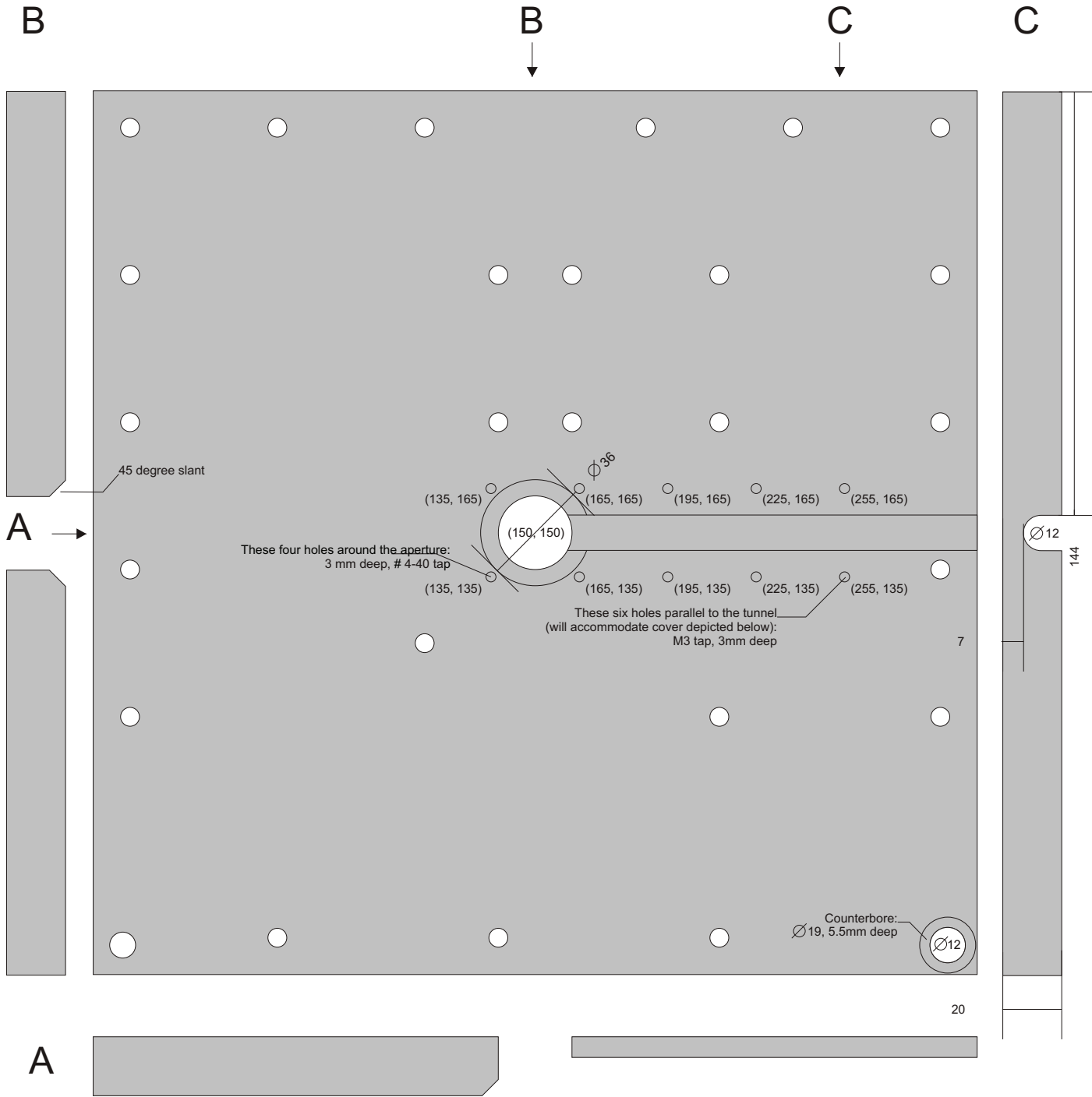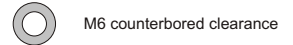M6 counterbored clearance

M6 tap, 20mm deep

Part A

Top/bottom

20

(10, 10)   (60, 10)   (110, 10)   (185, 10)   (235, 10)   (285, 10)

Outer face

(10, 117.5)   (210, 117.5)   (285, 117.5)

43

⌀ 5   ⌀ 5

(10, 75)   (210, 75)   (285, 75)

150

92

(10, 32.5)   (210, 32.5)   (285, 32.5)

51

295
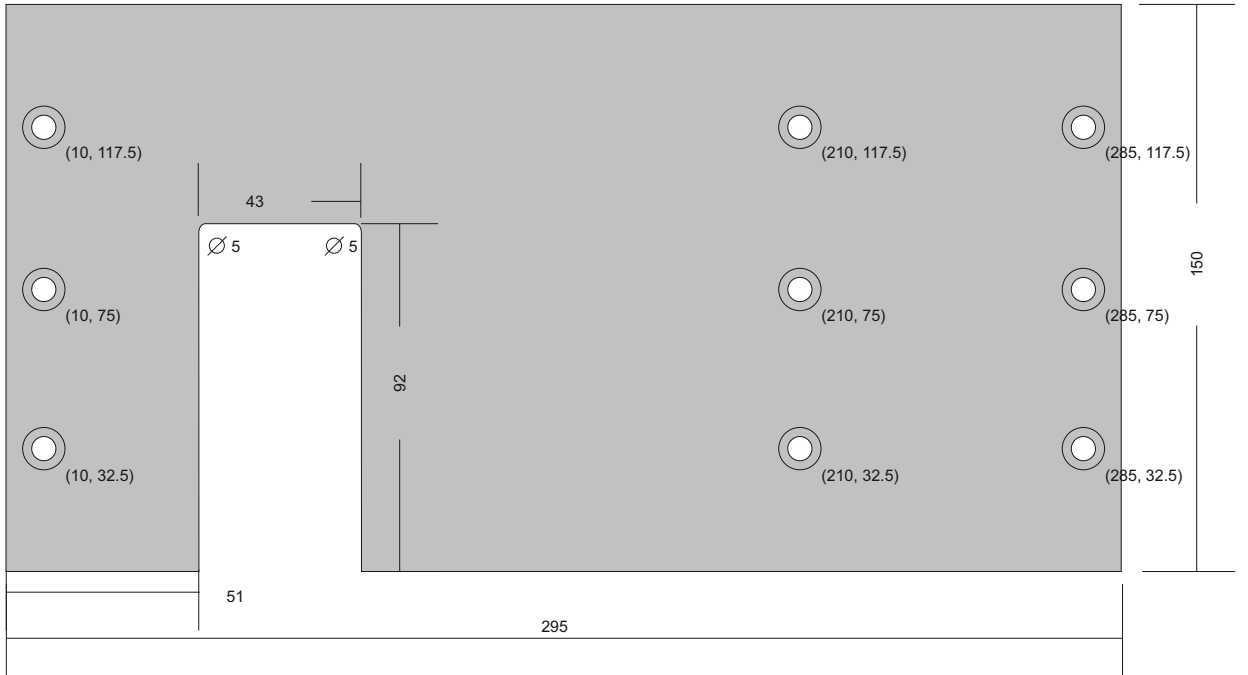
Part B (nb. Part C and D are Part B without the rectangular cut out)

Sides

215

(10, 117.5)

43

⌀ 5   ⌀ 5

(10, 75)

150

92

66

(10, 32.5)

20

Top/bottom

(25, 10)   (75, 10)   (125, 10)   (175, 10)
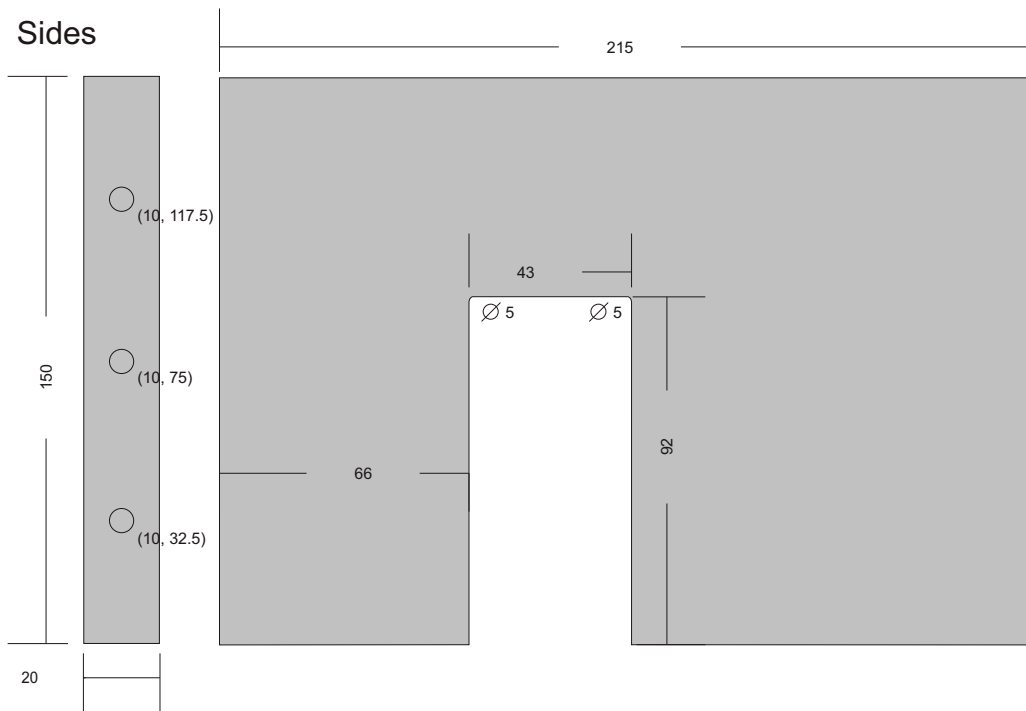
References

ADAIR, G. S. (1925). The Hemoglobin system. VI. The oxygen dissociation curve of Hemoglobin. J Biol Chem, 63, 529-545

ALON, U., CAMARENA, L., SURETTE, M. G., AGUERA Y ARCAS, B., LIU, Y., LEIBLER, S. & STOCK, J. B. (1998). Response regulator output in bacterial chemotaxis. EMBO J, 17(15), 4238-4248.

AMES, P. & PARKINSON, J. S. (1994). Constitutively signaling fragments of Tsr, the *Escherichia coli* serine chemoreceptor. J Bacteriol, 176(20), 6340-6348.

AMES, P., STUDDERT, C. A., REISER, R. H. & PARKINSON, J. S. (2002). Collaborative signaling by mixed chemoreceptor teams in *Escherichia coli*. Proc Natl Acad Sci U S A, 99(10), 7060-7065.

APPLEBY, J. L. & BOURRET, R. B. (1998). Proposed signal transduction role for conserved CheY residue Thr87, a member of the response regulator active-site quintet. J Bacteriol, 180(14), 3563-3569.

ASAI, Y., YAKUSHI, T., KAWAGISHI, I. & HOMMA, M. (2003). Ion-coupling determinants of Na+-driven and H+-driven flagellar motors. J Mol Biol, 327(2), 453-463.

BAKER, M. D., WOLANIN, P. M. & STOCK, J. B. (2006a). Signal transduction in bacterial chemotaxis. Bioessays, 28(1), 9-22.

BAKER, M. D., WOLANIN, P. M. & STOCK, J. B. (2006b). Systems biology of bacterial chemotaxis. Curr Opin Microbiol, 9(2), 187-192.

BARAK, R., WELCH, M., YANOVSKY, A., OOSAWA, K. & Eisenbach, M. (1992). Acetyladenylate or its derivative acetylates the chemotaxis protein CheY in vitro and increases its activity at the flagellar switch. Biochemistry 31, 10099–10107.

BARAK, R., PRASAD, K., SHAINSKAYA, A., WOLFE, A. J. & EISENBACH, M. (2004). Acetylation of the chemotaxis response regulator CheY by acetyl-CoA synthetase purified from *Escherichia coli*. J Mol Biol, 342(2), 383-401.

BARAK, R., YAN, J., SHAINSKAYA, A. & EISENBACH, M. (2006). The chemotaxis response regulator CheY can catalyze its own acetylation. J Mol Biol, 359(2), 251-265.

BERG, H. C. & BROWN, D. A. (1972). Chemotaxis in *Escherichia coli* analysed by three-dimensional tracking. Nature, 239(5374), 500-504.

BERG, H. C. & ANDERSON, R. A. (1973). Bacteria swim by rotating their flagellar filaments. Nature, 245(5425), 380-382.

BERG, H. C. & TEDESCO, P. M. (1975). Transient response to chemotactic stimuli in *Escherichia coli*. Proc Natl Acad Sci U S A, 72(8), 3235-3239.

BERG, H. C. & PURCELL, E. M. (1977). Physics of chemoreception. Biophys J, 20(2), 193-219.

BERG, H. C., MANSON, M. D. & CONLEY, M. P. (1982). Dynamics and energetics of flagellar rotation in bacteria. Symp Soc Exp Biol, 35, 1-31.

BERG, H. C. & TURNER, L. (1993). Torque generated by the flagellar motor of *Escherichia coli*. Biophys J, 65(5), 2201-2216.

BERG, H. C. (2003). The rotary motor of bacterial flagella. Annu Rev Biochem, 72, 19-54.

BEZDEK, J. C. & HATHAWAY, R. J. (2002). VAT: a tool for visual assessment of (cluster) tendency. Proc IJCNN, Piscataway, NJ, 2225-2230.

BLAIR, D. F. & BERG, H. C. (1990). The MotA protein of *E. coli* is a proton-conducting component of the flagellar motor. Cell, 60(3), 439-449.

BLOCK, S. M., SEGALL, J. E. & BERG, H. C. (1983). Adaptation kinetics in bacterial chemotaxis. J Bacteriol, 154(1), 312-323.

BLOCK, S. M., BLAIR, D. F. & BERG, H. C. (1991). Compliance of bacterial polyhooks measured with optical tweezers. Cytometry, 12(6), 492-496.

BOHR, C., HASSELBALCH, K. & KROGH, A. (1904). Über einen in biologischer Beziehung wichtigen Einfluss, den die Kohlensäurespannung des Blutes auf dessen Sauerstoffbindung übt. Skand Arch Physiol 16, 401–412.

BORNHORST, J. A. & FALKE, J. J. (2000). Attractant regulation of the aspartate receptor-kinase complex: limited cooperative interactions between receptors and effects of the receptor modification state. Biochemistry, 39(31), 9486-9493.

BOURRET, R. B. & STOCK, A. M. (2002). Molecular information processing: lessons from bacterial chemotaxis. J Biol Chem, 277(12), 9625-9628.

BRAUN, T. F. & BLAIR, D. F. (2001). Targeted disulfide cross-linking of the MotB protein of *Escherichia coli*: evidence for two H(+) channels in the stator Complex. Biochemistry, 40(43), 13051-13059.

BRAUN, T. F., AL-MAWSAWI, L. Q., KOJIMA, S. & BLAIR, D. F. (2004). Arrangement of core membrane segments in the MotA/MotB proton-channel complex of *Escherichia coli*. Biochemistry, 43(1), 35-45.

BRAY, D., BOURRET, R. B. & SIMON, M. I. (1993). Computer simulation of the phosphorylation cascade controlling bacterial chemotaxis. Mol Biol Cell, 4(5), 469-482.

BRAY, D., LEVIN, M. D. & MORTON-FIRTH, C. J. (1998). Receptor clustering as a cellular mechanism to control sensitivity. Nature, 393(6680), 85-88.

BRAY, D. (2002). Bacterial chemotaxis and the question of gain. Proc Natl Acad Sci U S A, 99(1), 7-9.

BRAY, D. & DUKE, T. (2004). Conformational spread: the propagation of allosteric states in large multiprotein complexes. Annu Rev Biophys Biomol Struct, 33, 53-73.

BREN, A. & EISENBACH, M. (1998). The N terminus of the flagellar switch protein, FliM, is the binding domain for the chemotactic response regulator, CheY. J Mol Biol, 278(3), 507-514.

BREN, A. & EISENBACH, M. (2000). How signals are heard during bacterial chemotaxis: protein-protein interactions in sensory signal propagation. J Bacteriol, 182(24), 6865-6873.

BROWN, D. A. & BERG, H. C. (1974). Temporal stimulation of chemotaxis in *Escherichia coli*. Proc Natl Acad Sci U S A, 71(4), 1388-1392.

BROWN, P. N., HILL, C. P. & BLAIR, D. F. (2002). Crystal structure of the middle and C-terminal domains of the flagellar rotor protein FliG. EMBO J, 21(13), 3225-3234.

BROWN, P. N., MATHEWS, M. A., JOSS, L. A., HILL, C. P. & BLAIR, D. F. (2005). Crystal structure of the flagellar rotor protein FliN from *Thermotoga maritima*. J Bacteriol, 187(8), 2890-2902.

BROWN, P. N., TERRAZAS, M., PAUL, K. & BLAIR, D. F. (2007). Mutational analysis of the flagellar protein FliG: sites of interaction with FliM and implications for organization of the switch complex. J Bacteriol, 189(2), 305-312.

CHANGEUX, J. P. & EDELSTEIN, S. J. (2005). Allosteric mechanisms of signal transduction. Science, 308(5727), 1424-1428.

CHEN, X. & BERG, H. C. (2000a). Torque-speed relationship of the flagellar rotary motor of *Escherichia coli*. Biophys J, 78(2), 1036-1041.

CHEN, X. & BERG, H. C. (2000b). Solvent-isotope and pH effects on flagellar rotation in *Escherichia coli*. Biophys J, 78(5), 2280-2284.

CHUN, S. Y. & PARKINSON, J. S. (1988). Bacterial motility: membrane topology of the *Escherichia coli* MotB protein. Science, 239(4837), 276-278.

CLUZEL, P., SURETTE, M. & LEIBLER, S. (2000). An ultrasensitive bacterial motor revealed by monitoring signaling proteins in single cells. Science, 287(5458), 1652-1655.

COHEN-BEN-LULU, G. N., FRANCIS, N. R., SHIMONI, E., NOY, D., DAVIDOV, Y., PRASAD, K., SAGI, Y., CECCHINI, G., JOHNSTONE, R. M. & EISENBACH, M. (2008). The bacterial flagellar switch complex is getting more complex. EMBO J, 27(7), 1134-1144.

DARNTON, N. C., TURNER, L., ROJEVSKY, S. & BERG, H. C. (2007). On torque and tumbling in swimming *Escherichia coli*. J Bacteriol, 189(5), 1756-1764.

DE MOT, R. & VANDERLEYDEN, J. (1994). The C-terminal sequence conservation between OmpA-related outer membrane proteins and MotB suggests a common function in both gram-positive and gram-negative bacteria, possibly in the interaction of these domains with peptidoglycan. Mol Microbiol, 12(2), 333-334.

DEAN, G. E., MACNAB, R. M., STADER, J., MATSUMURA, P. & BURKS, C. (1984). Gene sequence and predicted amino acid sequence of the motA protein, a membrane-associated protein required for flagellar rotation in *Escherichia coli*. J Bacteriol, 159(3), 991-999.

DEPAMPHILIS, M. L. & ADLER, J. (1971). Fine structure and isolation of the hook-basal body complex of flagella from *Escherichia coli* and *Bacillus subtilis*. J Bacteriol, 105(1), 384-395.

DRAKE, S. K., BOURRET, R. B., LUCK, L. A., SIMON, M. I. & FALKE, J. J. (1993). Activation of the phosphosignaling protein CheY. I. Analysis of the phosphorylated conformation by 19F NMR and protein engineering. J Biol Chem, 268(18), 13081-13088.

DUKE, T. A. & BRAY, D. (1999). Heightened sensitivity of a lattice of membrane receptors. Proc Natl Acad Sci U S A, 96(18), 10104-10108.

DUKE, T. A., LE NOVERE, N. & BRAY, D. (2001). Conformational spread in a ring of proteins: a stochastic approach to allostery. J Mol Biol, 308(3), 541-553.

DYER, C. M., QUILLIN, M. L., CAMPOS, A., LU, J., MCEVOY, M. M., HAUSRATH, A. C., WESTBROOK, E. M., MATSUMURA, P., MATTHEWS, B. W. &

DAHLQUIST, F. W. (2004). Structure of the constitutively active double mutant CheYD13K Y106W alone and in complex with a FliM peptide. J Mol Biol, 342(4), 1325-1335.

DYER, C. M. & DAHLQUIST, F. W. (2006). Switched or not?: the structure of unphosphorylated CheY bound to the N terminus of FliM. J Bacteriol, 188(21), 7354-7363.

DYER, C. M., VARTANIAN, A. S., ZHOU, H. & DAHLQUIST, F. W. (2009). A molecular mechanism of bacterial flagellar motor switching. J Mol Biol, 388(1), 71-84.

EIGEN, M. (1967). Kinetics of reaction control and information transfer in enzymes and nucleic acids. Nobel Symp, 5, 333-369

EISENBACH, M., WOLF, A., WELCH, M., CAPLAN, S. R., LAPIDUS, I. R., MACNAB, R. M., ALONI, H. & ASHER, O. (1990). Pausing, switching and speed fluctuation of the bacterial flagellar motor and their relation to motility and chemotaxis. J Mol Biol, 211(3), 551-563.

EMONET, T. & CLUZEL, P. (2008). Relationship between cellular response and behavioral variability in bacterial chemotaxis. Proc Natl Acad Sci U S A, 105(9), 3304-3309.

ENDRES, R. G., OLEKSIUK, O., HANSEN, C. H., MEIR, Y., SOURJIK, V. & WINGREEN, N. S. (2008). Variable sizes of *Escherichia coli* chemoreceptor signaling teams. Mol Syst Biol, 4, 211.

FAHRNER, K. A., RYU, W. S. & BERG, H. C. (2003). Biomechanics: bacterial flagellar switching under load. Nature, 423(6943), 938.

FRANCIS, N. R., IRIKURA, V. M., YAMAGUCHI, S., DEROSIER, D. J. & MACNAB, R. M. (1992). Localization of the *Salmonella typhimurium* flagellar switch protein FliG to the cytoplasmic M-ring face of the basal body. Proc Natl Acad Sci U S A, 89(14), 6304-6308.

FUKUOKA, H., WADA, T., KOJIMA, S., ISHIJIMA, A. & HOMMA, M. (2009). Sodium-dependent dynamic assembly of membrane complexes in sodium-driven flagellar motors. Mol Microbiol, 71(4), 825-835.

FUNG, D. C. & BERG, H. C. (1995). Powering the flagellar motor of *Escherichia coli* with an external voltage source. Nature, 375(6534), 809-812.

GESTWICKI, J. E., LAMANNA, A. C., HARSHEY, R. M., MCCARTER, L. L., KIESSLING, L. L. & ADLER, J. (2000). Evolutionary conservation of methyl-accepting chemotaxis protein location in Bacteria and Archaea. J Bacteriol, 182(22), 6499-6502.

GESTWICKI, J. E. & KIESSLING, L. L. (2002). Inter-receptor communication through arrays of bacterial chemoreceptors. Nature, 415(6867), 81-84.

GITTES, F. & SCHMIDT, C. F. (1998). Interference model for back-focal-plane displacement detection in optical tweezers. Opt Lett, 23(1), 7-9.

HILL, A. V. (1913). The combinations of Haemoglobin with oxygen and with carbon monoxide. I Biochem J, 7(5), 471-480.

HILLE, B. (1992). Ionic channels of excitable membranes, 2nd ed., Sinauer Associates Inc.

KARPEN, J. W. & RUIZ, M. (2002). Ion channels: does each subunit do something on its own? Trends Biochem Sci, 27(8), 402-409.

KATAYAMA, E., SHIRAISHI, T., OOSAWA, K., BABA, N. & AIZAWA, S. (1996). Geometry of the flagellar motor in the cytoplasmic membrane of *Salmonella typhimurium* as determined by stereo-photogrammetry of quick-freeze deep-etch replica images. J Mol Biol, 255(3), 458-475.

KEYMER, J. E., ENDRES, R. G., SKOGE, M., MEIR, Y. & WINGREEN, N. S. (2006). Chemosensing in *Escherichia coli*: two regimes of two-state receptors. Proc Natl Acad Sci U S A, 103(6), 1786-1791.

KIM, C., JACKSON, M., LUX, R. & KHAN, S. (2001). Determinants of chemotactic signal amplification in *Escherichia coli*. J Mol Biol, 307(1), 119-135.

KIM, K. K., YOKOTA, H. & KIM, S. H. (1999). Four-helical-bundle structure of the cytoplasmic domain of a serine chemotaxis receptor. Nature, 400(6746), 787-792.

KIM, M., BIRD, J. C., VAN PARYS, A. J., BREUER, K. S. & POWERS, T. R. (2003). A macroscopic scale model of bacterial flagellar bundling. Proc Natl Acad Sci U S A, 100(26), 15481-15485.

KOJIMA, S. & BLAIR, D. F. (2001). Conformational change in the stator of the bacterial flagellar motor. Biochemistry, 40(43), 13041-13050.

KOJIMA, S. & BLAIR, D. F. (2004). Solubilization and purification of the MotA/MotB complex of *Escherichia coli*. Biochemistry, 43(1), 26-34.

KOROBKOVA, E., EMONET, T., VILAR, J. M., SHIMIZU, T. S. & CLUZEL, P. (2004). From molecular noise to behavioural variability in a single bacterium. Nature, 428(6982), 574-578.

KOROBKOVA, E. A., EMONET, T., PARK, H. & CLUZEL, P. (2006). Hidden stochastic nature of a single bacterial motor. Phys Rev Lett, 96(5), 058105.

KOSHLAND, D. E., JR., NÉMETHY, G. & FILMER, D (1966). Comparison of experimental binding data and theoretical models in proteins containing subunits. Biochemistry, 5(1), 365-368.

KOSHLAND, D. E., JR., GOLDBETER, A. & STOCK, J. B. (1982). Amplification and adaptation in regulatory and sensory systems. Science, 217(4556), 220-225.

KOSHLAND, D. E., JR. & HAMADANI, K. (2002). Proteomics and models for enzyme cooperativity. J Biol Chem, 277(49), 46841-46844.

KUDO, S., MAGARIYAMA, Y. & AIZAWA, S. (1990). Abrupt changes in flagellar rotation observed by laser dark-field microscopy. Nature, 346(6285), 677-680.

KUO, S. C. & KOSHLAND, D. E., JR. (1989). Multiple kinetic states for the flagellar motor switch. J Bacteriol, 171(11), 6279-6287.

LAPIDUS, I. R., WELCH, M. & EISENBACH, M. (1988). Pausing of flagellar rotation is a component of bacterial motility and chemotaxis. J Bacteriol, 170(8), 3627-3632.

LARSEN, S. H., READER, R. W., KORT, E. N., TSO, W. W. & ADLER, J. (1974). Change in direction of flagellar rotation is the basis of the chemotactic response in *Escherichia coli*. Nature, 249(452), 74-77.

LEAKE, M. C., CHANDLER, J. H., WADHAMS, G. H., BAI, F., BERRY, R. M. & ARMITAGE, J. P. (2006). Stoichiometry and turnover in single, functioning membrane protein complexes. Nature, 443(7109), 355-358.

LEE, S. Y., CHO, H. S., PELTON, J. G., YAN, D., BERRY, E. A. & WEMMER, D. E. (2001). Crystal structure of activated CheY. Comparison with other activated receiver domains. J Biol Chem, 276(19), 16425-16431.

LI, G. & WEIS, R. M. (2000). Covalent modification regulates ligand binding to receptor complexes in the chemosensory system of *Escherichia coli*. Cell, 100(3), 357-365.

LI, M. & HAZELBAUER, G. L. (2004). Cellular stoichiometry of the components of the chemotaxis signaling complex. J Bacteriol, 186(12), 3687-3694.

LIARZI, O., BARAK, R., BRONNER, V., DINES, M., SAGI, Y., SHAINSKAYA, A. & EISENBACH, M. Acetylation represses the binding of CheY to its target proteins. Mol Microbiol.

LLOYD, S. A. & BLAIR, D. F. (1997). Charged residues of the rotor protein FliG essential for torque generation in the flagellar motor of *Escherichia coli*. J Mol Biol, 266(4), 733-744.

LLOYD, S. A., WHITBY, F. G., BLAIR, D. F. & HILL, C. P. (1999). Structure of the C-terminal domain of FliG, a component of the rotor in the bacterial flagellar motor. Nature, 400(6743), 472-475.

LO, C. J., LEAKE, M. C. & BERRY, R. M. (2006). Fluorescence measurement of intracellular sodium concentration in single *Escherichia coli* cells. Biophys J, 90(1), 357-365.

LO, C. J., LEAKE, M. C., PILIZOTA, T. & BERRY, R. M. (2007). Nonequivalence of membrane voltage and ion-gradient as driving forces for the bacterial flagellar motor at low load. Biophys J, 93(1), 294-302.

LOWDER, B. J., DUYVESTEYN, M. D. & BLAIR, D. F. (2005). FliG subunit arrangement in the flagellar rotor probed by targeted cross-linking. J Bacteriol, 187(16), 5640-5647.

LOWRY, D. F., ROTH, A. F., RUPERT, P. B., DAHLQUIST, F. W., MOY, F. J., DOMAILLE, P. J. & MATSUMURA, P. (1994). Signal transduction in chemotaxis. A propagating conformation change upon phosphorylation of CheY. J Biol Chem, 269(42), 26358-26362.

LUKAT, G. S., LEE, B. H., MOTTONEN, J. M., STOCK, A. M. & STOCK, J. B. (1991). Roles of the highly conserved aspartate and lysine residues in the response regulator of bacterial chemotaxis. J Biol Chem, 266(13), 8348-8354.

MADDOCK, J. R. & SHAPIRO, L. (1993). Polar location of the chemoreceptor complex in the *Escherichia coli* cell. Science, 259(5102), 1717-1723.

MANSON, M. D., TEDESCO, P., BERG, H. C., HAROLD, F. M. & VAN DER DRIFT, C. (1977). A protonmotive force drives bacterial flagella. Proc Natl Acad Sci U S A, 74(7), 3060-3064.

MATHEWS, M. A., TANG, H. L. & BLAIR, D. F. (1998). Domain analysis of the FliM protein of *Escherichia coli*. J Bacteriol, 180(21), 5580-5590.

MATSUMOTO, M. & NISHIMURA, T. (1998). ACM transactions on modeling and computer simulation. 8(1), 3-30.

MATSUURA, S., SHIOI, J. I., IMAE, Y. & IIDA, S. (1979). Characterization of the *Bacillus subtilis* motile system driven by an artificially created proton motive force. J Bacteriol, 140(1), 28-36.

MCEVOY, M. M., HAUSRATH, A. C., RANDOLPH, G. B., REMINGTON, S. J. & DAHLQUIST, F. W. (1998). Two binding modes reveal flexibility in kinase/response regulator interactions in the bacterial chemotaxis pathway. Proc Natl Acad Sci U S A, 95(13), 7333-7338.

MELLO, B. A. & TU, Y. (2003). Quantitative modeling of sensitivity in bacterial chemotaxis: the role of coupling among different chemoreceptor species. Proc Natl Acad Sci U S A, 100(14), 8223-8228.

MELLO, B. A., SHAW, L. & TU, Y. (2004). Effects of receptor interaction in bacterial chemotaxis. Biophys J, 87(3), 1578-1595.

MELLO, B. A. & TU, Y. (2005). An allosteric model for heterogeneous receptor complexes: understanding bacterial chemotaxis responses to multiple stimuli. Proc Natl Acad Sci U S A, 102(48), 17354-17359.

MICHAELIS, L. & MENTEN, M. L. (1913). Die kinetik der invertinwirkung. Biochem Z, 49, 333.

MINAMINO, T. & NAMBA, K. (2004). Self-assembly and type III protein export of the bacterial flagellum. J Mol Microbiol Biotechnol, 7(1-2), 5-17.

MONOD, J., WYMAN, J. & CHANGEUX J.-P. (1965). On the nature of allosteric transitions: a plausible model. J Mol Biol, 12, 88-118.

NEKOUZADEH, A. & RUDY, Y. (2007). Statistical properties of ion channel records. Part I: relationship to the macroscopic current. Math Biosci, 210(1), 291-314.

NEUMAN, K. C. & BLOCK, S. M. (2004). Optical trapping. Rev Sci Instrum, 75(9), 2787-2809.

PARK, S. Y., LOWDER, B., BILWES, A. M., BLAIR, D. F. & CRANE, B. R. (2006). Structure of FliM provides insight into assembly of the switch complex in the bacterial flagella motor. Proc Natl Acad Sci U S A, 103(32), 11886-11891.

PARKINSON, J. S., AMES, P. & STUDDERT, C. A. (2005). Collaborative signaling by bacterial chemoreceptors. Curr Opin Microbiol, 8(2), 116-121.

PAUL, K. & BLAIR, D. F. (2006). Organization of FliN subunits in the flagellar motor of *Escherichia coli*. J Bacteriol, 188(7), 2502-2511.

PAUL, K., HARMON, J. G. & BLAIR, D. F. (2006). Mutational analysis of the flagellar rotor protein FliN: identification of surfaces important for flagellar assembly and switching. J Bacteriol, 188(14), 5240-5248.

PILIZOTA, T., BILYARD, T., BAI, F., FUTAI, M., HOSOKAWA, H. & BERRY, R. M. (2007). A programmable optical angle clamp for rotary molecular motors. Biophys J, 93(1), 264-275.

PILIZOTA, T., BROWN, M. T., LEAKE, M. C., BRANCH, R. W., BERRY, R. M. & ARMITAGE, J. P. (2009). A molecular brake, not a clutch, stops the *Rhodobacter sphaeroides* flagellar motor. Proc Natl Acad Sci U S A, 106(28), 11582-11587.

PRASAD, K., CAPLAN, S. R. & EISENBACH, M. (1998). Fumarate modulates bacterial flagellar rotation by lowering the free energy difference between the clockwise and counterclockwise states of the motor. J Mol Biol, 280(5), 821-828.

PURCELL, E. M. (1997). The efficiency of propulsion by a rotating flagellum. Proc Natl Acad Sci U S A, 94(21), 11307-11311.

QIN, F. & LI, L. (2004). Model-based fitting of single-channel dwell-time distributions. Biophys J, 87(3), 1657-1671.

RAMAKRISHNAN, R., SCHUSTER, M. & BOURRET, R. B. (1998). Acetylation at Lys-92 enhances signaling by the chemotaxis response regulator protein CheY. Proc Natl Acad Sci U S A, 95(9), 4918-4923.

REID, S. W., LEAKE, M. C., CHANDLER, J. H., LO, C. J., ARMITAGE, J. P. & BERRY, R. M. (2006). The maximum number of torque-generating units in the flagellar motor of *Escherichia coli* is at least 11. Proc Natl Acad Sci U S A, 103(21), 8066-8071.

RIESSNER, T., WOELK, F., ABSHAGEN-KEUNECKE, M., CALIEBE, A. & HANSEN, U. P. (2002). A new level detector for ion channel analysis. J Membr Biol, 189(2), 105-118.

RYU, W. S., BERRY, R. M. & BERG, H. C. (2000). Torque-generating units of the flagellar motor of *Escherichia coli* have a high duty ratio. Nature, 403(6768), 444-447.

SAGI, Y., KHAN, S. & EISENBACH, M. (2003). Binding of the chemotaxis response regulator CheY to the isolated, intact switch complex of the bacterial flagellar motor: lack of cooperativity. J Biol Chem, 278(28), 25867-25871.

SAMATEY, F. A., MATSUNAMI, H., IMADA, K., NAGASHIMA, S., SHAIKH, T. R., THOMAS, D. R., CHEN, J. Z., DEROSIER, D. J., KITAO, A. & NAMBA, K. (2004). Structure of the bacterial flagellar hook and implication for the molecular universal joint mechanism. Nature, 431(7012), 1062-1068.

SAMBROOK, J. & RUSSELL, D.W. (2001). Molecular Cloning: A Laboratory Manual. CSHL Press.

SATO, K. & HOMMA, M. (2000). Functional reconstitution of the Na(+)-driven polar flagellar motor component of *Vibrio alginolyticus*. J Biol Chem, 275(8), 5718-5722.

SCHARF, B. E., FAHRNER, K. A., TURNER, L. & BERG, H. C. (1998a). Control of direction of flagellar rotation in bacterial chemotaxis. Proc Natl Acad Sci U S A, 95(1), 201-206.

SCHARF, B. E., FAHRNER, K. A. & BERG, H. C. (1998b). CheZ has no effect on flagellar motors activated by CheY13DK106YW. J Bacteriol, 180(19), 5123-5128.

SCHUSTER, S. C., SWANSON, R. V., ALEX, L. A., BOURRET, R. B. & SIMON, M. I. (1993). Assembly and function of a quaternary signal transduction complex monitored by surface plasmon resonance. Nature, 365(6444), 343-347.

SEGALL, J. E., BLOCK, S. M. & BERG, H. C. (1986). Temporal comparisons in bacterial chemotaxis. Proc Natl Acad Sci U S A, 83(23), 8987-8991.

SHARP, L. L., ZHOU, J. & BLAIR, D. F. (1995a). Features of MotA proton channel structure revealed by tryptophan-scanning mutagenesis. Proc Natl Acad Sci U S A, 92(17), 7946-7950.

SHARP, L. L., ZHOU, J. & BLAIR, D. F. (1995b). Tryptophan-scanning mutagenesis of MotB, an integral membrane protein essential for flagellar rotation in *Escherichia coli*. Biochemistry, 34(28), 9166-9171.

SHI, Y. & DUKE, T. (1998). Cooperative model of bacterial sensing. Phys Rev E, 58, 6399-6406.

SHIMIZU, T. S., LE NOVERE, N., LEVIN, M. D., BEAVIL, A. J., SUTTON, B. J. & BRAY, D. (2000). Molecular model of a lattice of signalling proteins involved in bacterial chemotaxis. Nat Cell Biol, 2(11), 792-796.

SHIMIZU, T. S., AKSENOV, S. V. & BRAY, D. (2003). A spatially extended stochastic model of the bacterial chemotaxis signalling pathway. J Mol Biol, 329(2), 291-309.

SILVERMAN, M. & SIMON, M. (1974). Flagellar rotation and the mechanism of bacterial motility. Nature, 249(452), 73-74.

SKOGE, M. L., ENDRES, R. G. & WINGREEN, N. S. (2006). Receptor-receptor coupling in bacterial chemotaxis: evidence for strongly coupled clusters. Biophys J, 90(12), 4317-4326.

SOURJIK, V. (2004). Receptor clustering and signal processing in *E. coli* chemotaxis. Trends Microbiol, 12(12), 569-576.

SOURJIK, V. & BERG, H. C. (2000). Localization of components of the chemotaxis machinery of *Escherichia coli* using fluorescent protein fusions. Mol Microbiol, 37(4), 740-751.

SOURJIK, V. & BERG, H. C. (2002a). Receptor sensitivity in bacterial chemotaxis. Proc Natl Acad Sci U S A, 99(1), 123-127.

SOURJIK, V. & BERG, H. C. (2002b). Binding of the *Escherichia coli* response regulator CheY to its target measured in vivo by fluorescence resonance energy transfer. Proc Natl Acad Sci U S A, 99(20), 12669-12674.

SOURJIK, V. & BERG, H. C. (2004). Functional interactions between receptors in bacterial chemotaxis. Nature, 428(6981), 437-441.

SOWA, Y., ROWE, A. D., LEAKE, M. C., YAKUSHI, T., HOMMA, M., ISHIJIMA, A. & BERRY, R. M. (2005). Direct observation of steps in rotation of the bacterial flagellar motor. Nature, 437(7060), 916-919.

SOWA, Y. & BERRY, R. M. (2008). Bacterial flagellar motor. Q Rev Biophys, 41(2), 103-132.

STRYER, L., BERG, J. M., & TYMOCZKO, J. L. (2002). Biochemistry 5th ed., W. H. Freeman and Co. Ltd.

STUDDERT, C. A. & PARKINSON, J. S. (2004). Crosslinking snapshots of bacterial chemoreceptor squads. Proc Natl Acad Sci U S A, 101(7), 2117-2122.

SUZUKI, H., YONEKURA, K. & NAMBA, K. (2004). Structure of the rotor of the bacterial flagellar motor revealed by electron cryomicroscopy and single-particle image analysis. J Mol Biol, 337(1), 105-113.

THOMAS, D. R., MORGAN, D. G. & DEROSIER, D. J. (1999). Rotational symmetry of the C ring and a mechanism for the flagellar rotary motor. Proc Natl Acad Sci U S A, 96(18), 10134-10139.

THOMAS, D. R., FRANCIS, N. R., XU, C. & DEROSIER, D. J. (2006). The three-dimensional structure of the flagellar rotor from a clockwise-locked mutant of *Salmonella enterica* serovar Typhimurium. J Bacteriol, 188(20), 7039-7048.

TOGASHI, F., YAMAGUCHI, S., KIHARA, M., AIZAWA, S. I. & MACNAB, R. M. (1997). An extreme clockwise switch bias mutation in fliG of *Salmonella typhimurium* and its suppression by slow-motile mutations in motA and motB. J Bacteriol, 179(9), 2994-3003.

TU, Y. & GRINSTEIN, G. (2005). How white noise generates power-law switching in bacterial flagellar motors. Phys Rev Lett, 94(20), 208101.

TURNER, L., CAPLAN, S. R. & BERG, H. C. (1996). Temperature-induced switching of the bacterial flagellar motor. Biophys J, 71(4), 2227-2233.

TURNER, L., SAMUEL, A. D., STERN, A. S. & BERG, H. C. (1999). Temperature dependence of switching of the bacterial flagellar motor by the protein CheY(13DK106YW). Biophys J, 77(1), 597-603.

TURNER, L., RYU, W. S. & BERG, H. C. (2000). Real-time imaging of fluorescent flagellar filaments. J Bacteriol, 182(10), 2793-2801.

VAN ALBADA, S. B., TANASE-NICOLA, S. & TEN WOLDE, P. R. (2009). The switching dynamics of the bacterial flagellar motor. Mol Syst Biol, 5, 316.

VAN WAY, S. M., MILLAS, S. G., LEE, A. H. & MANSON, M. D. (2004). Rusty, jammed, and well-oiled hinges: Mutations affecting the interdomain region of FliG, a rotor element of the *Escherichia coli* flagellar motor. J Bacteriol, 186(10), 3173-3181.

VIAPPIANI, C., BETTATI, S., BRUNO, S., RONDA, L., ABBRUZZETTI, S., MOZZARELLI, A. & EATON, W. A. (2004). New insights into allosteric mechanisms from trapping unstable protein conformations in silica gels. Proc Natl Acad Sci U S A, 101(40), 14414-14419.

VOLZ, K. & MATSUMURA, P. (1991). Crystal structure of *Escherichia coli* CheY refined at 1.7-A resolution. J Biol Chem, 266(23), 15511-15519.

WADHAMS, G. H. & ARMITAGE, J. P. (2004). Making sense of it all: bacterial chemotaxis. Nat Rev Mol Cell Biol, 5(12), 1024-1037.

WELCH, M., OOSAWA, K., AIZAWA, S. & EISENBACH, M. (1993). Phosphorylation-dependent binding of a signal molecule to the flagellar switch of bacteria. Proc Natl Acad Sci U S A, 90(19), 8787-8791.

WELCH, M., CHINARDET, N., MOUREY, L., BIRCK, C. & SAMAMA, J. P. (1998). Structure of the CheY-binding domain of histidine kinase CheA in complex with CheY. Nat Struct Biol, 5(1), 25-29.

WOLANIN, P. M. & STOCK, J. B. (2004). Bacterial chemosensing: cooperative molecular logic. Curr Biol, 14(12), R486-487.

XING, J., BAI, F., BERRY, R. & OSTER, G. (2006). Torque-speed relationship of the bacterial flagellar motor. Proc Natl Acad Sci U S A, 103(5), 1260-1265.

YAMAGUCHI, S., AIZAWA, S., KIHARA, M., ISOMURA, M., JONES, C. J. & MACNAB, R. M. (1986a). Genetic evidence for a switching and energy-transducing complex in the flagellar motor of *Salmonella typhimurium*. J Bacteriol, 168(3), 1172-1179.

YAMAGUCHI, S., FUJITA, H., ISHIHARA, A., AIZAWA, S. & MACNAB, R. M. (1986b). Subdivision of flagellar genes of *Salmonella typhimurium* into regions responsible for assembly, rotation, and switching. J Bacteriol, 166(1), 187-193.

YASUDA, R., NOJI, H., YOSHIDA, M., KINOSITA, K., JR. & ITOH, H. (2001). Resolution of distinct rotational substeps by submillisecond kinetic analysis of F1-ATPase. Nature, 410(6831), 898-904.

YILDIZ, A., FORKEY, J. N., MCKINNEY, S. A., HA, T., GOLDMAN, Y. E. & SELVIN, P. R. (2003). Myosin V walks hand-over-hand: single fluorophore imaging with 1.5-nm localization. Science, 300(5628), 2061-2065.

YILDIZ, A., TOMISHIGE, M., VALE, R. D. & SELVIN, P. R. (2004). Kinesin walks hand-over-hand. Science, 303(5658), 676-678.

YUAN, J. & BERG, H. C. (2008). Resurrection of the flagellar rotary motor near zero load. Proc Natl Acad Sci U S A, 105(4), 1182-1185.

YUAN, J., FAHRNER, K. A. & BERG, H. C. (2009). Switching of the bacterial flagellar motor near zero load. J Mol Biol, 390(3), 394-400.

ZHOU, J. & BLAIR, D. F. (1997). Residues of the cytoplasmic domain of MotA essential for torque generation in the bacterial flagellar motor. J Mol Biol, 273(2), 428-439.

ZHOU, J., LLOYD, S. A. & BLAIR, D. F. (1998). Electrostatic interactions between rotor and stator in the bacterial flagellar motor. Proc Natl Acad Sci U S A, 95(11), 6436-6441.

ZHU, X., REBELLO, J., MATSUMURA, P. & VOLZ, K. (1997a). Crystal structures of CheY mutants Y106W and T87I/Y106W. CheY activation correlates with movement of residue 106. J Biol Chem, 272(8), 5000-5006.

ZHU, X., VOLZ, K. & MATSUMURA, P. (1997b). The CheZ-binding surface of CheY overlaps the CheA- and FliM-binding surfaces. J Biol Chem, 272(38), 23758-23764.